Master Thesis

Massive Stars in the Orion-Eridanus Bubble

Niklas Bauer

Würzburg, December 2025

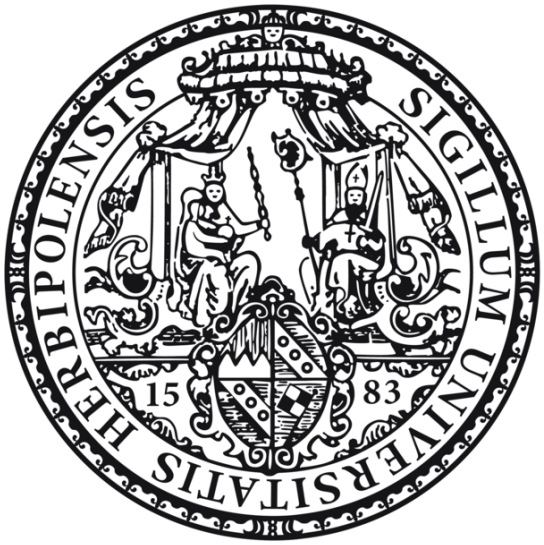

Julius-Maximilians-Universität Würzburg
Faculty of Physics and Astronomy

Supervisors: Dr. Thomas Siegert, Prof. Dr. Matthias Kadler

Abstract

The space telescopes CGRO/COMPTEL and INTEGRAL/SPI show the Milky Way in the 1.809 MeV gamma-ray line from the radioactive decay of ^{26}Al. This isotope with an intermediate lifetime of $\sim 1 \cdot 10^6$ yr, is mainly produced in massive stars, ejected in stellar winds and supernovae, and confined in superbubbles, such as the Orion Eridanus superbubble. INTEGRAL/SPI detected significant line flux from OB associations in Cygnus and in Scorpius Centaurus, but not from the Orion Eridanus superbubble. This thesis aims to detect a significant line flux from this superbubble in the Orion region. In addition, it aims to describe the morphology of the Orion Eridanus superbubble with a physical model based on previous results, to gain a deeper understanding of superbubble evolution as well as nucleosynthesis in stars leading to an observable ^{26}Al accumulation in superbubbles. For this, we give a theoretical overview on the physics of superbubbles before using two ^{26}Al sky modelling approaches to describe the Orion Eridanus superbubble and the expected gamma-ray signature. In the first approach, empirical models based on two 1.809 MeV all-sky surveys are used. In the second approach, physical models, tuned with the expected ^{26}Al mass from the stars in the Orion Eridanus superbubble, i.e., the Orion OB1 association, are used. These models are fitted to INTEGRAL/SPI data from ≈ 20 yr observation time. With the empirical model, we find a significant line detection of the Orion region with a significance up to $\sigma = 9.2$. The 1.809 MeV line flux is $F_{1809,\,\mathrm{empirical}} = (2.2 - 6.6) \cdot 10^{-5} \mathrm{ph\,cm^{-2}\,s^{-1}}$, which converts to an ^{26}Al mass of $M_{\mathrm{Al,\,empirical}} = (1.7 - 5.0) \cdot 10^{-5} \mathrm{M_\odot}$. These measured values take into account that the Orion region is situated in front of the Galactic plane, also shining in 1.809 MeV gamma-rays. The physical models lead to a significant line detection of the Orion Eridanus superbubble with a significance of up to $\sigma = 5.6$, with a 1.809 MeV line flux of $F_{1809,\,\mathrm{physical}} = (3.09^{+0.55}_{-0.39}) \cdot 10^{-5} \mathrm{ph\,cm^{-2}\,s^{-1}}$. This converts to an ^{26}Al mass of $M_{\mathrm{Al,\,physical}} = (2.3 \pm 0.4) \cdot 10^{-5} \mathrm{M_\odot}$, which is consistent with the empirical model result. From physical model comparison, we find Orion OB 1a to be dominant in the production and distribution of ^{26}Al. From population synthesis, we construct time profiles for the four subgroups in Orion OB1, and find a total ^{26}Al today of $M_{\mathrm{Al,\,pop}} = (0.002 - 1.9) \cdot 10^{-4} \mathrm{M_\odot}$. We detect the Orion Eridanus superbubble for the first time significantly at 1.809 MeV. The physical model result supports superbubble evolution models, used to describe the morphology of the Orion Eridanus superbubble. The population synthesis confirms stellar evolution models that give an ^{26}Al expectation reconcilable with the 1.809 MeV observation of the Orion Eridanus superbubble.

Zusammenfassung

Die Weltraumteleskope CGRO/COMPTEL und INTEGRAL/SPI zeigen die Milchstraße in der Emissionslinie mit 1.809,MeV aus dem radioaktiven Zerfall von ^{26}Al. Dieses Isotop mit einer mittleren Lebensdauer von $\sim 1 \cdot 10^6\,\mathrm{yr}$ wird hauptsächlich in massereichen Sternen produziert, in stellaren Winden und Supernovae ausgestoßen und in Superbubbles eingeschlossen, wie in der Orion-Eridanus-Superbubble. INTEGRAL/SPI detektierte signifikanten Linienfluss von OB–Assoziationen in Cygnus und in Scorpius Centaurus, aber nicht von der Orion-Eridanus-Superbubble. Diese Arbeit zielt darauf ab, einen signifikanten Linienfluss aus dieser Superbubble in der Orion-Region zu detektieren. Zusätzlich soll die Morphologie der Orion-Eridanus-Superbubble mit einem physikalischen Modell basierend auf vorherigen Ergebnissen beschrieben werden, um ein tieferes Verständnis von Superbubble-Evolution sowie der Nukleosynthese in Sternen zu gewinnen. Diese führt zu beobachtbaren Anhäufungen an ^{26}Al in Superbubbles. Dafür geben wir einen theoretischen Überblick über die Physik von Superbubbles, bevor wir zwei Modellierungsansätze des ^{26}Al-Himmels verwenden, um die Orion-Eridanus-Superbubble und die erwartete Gammastrahlensignatur zu beschreiben. Der erste Ansatz liegt in empirischen Modellen, basierend auf zwei 1.809,MeV all-sky-Surveys. Der zweite Ansatz liegt in physikalischen Modellen, abgestimmt auf die ^{26}Al-Masse Erwartung von den Sternen in der Orion-Eridanus-Superbubble, d.h. der Orion OB1-Assoziation. Diese Modelle werden an INTEGRAL/SPI-Daten aus $\approx 20\,\mathrm{yr}$ Beobachtungszeit gefitted. Mit dem empirischen Modell finden wir eine signifikante Liniendetektion der Orion-Region mit einer Signifikanz von bis zu $\sigma = 9.2$. Der 1.809,MeV Linienfluss beträgt $F_{1809,,\mathrm{empirical}} = (2.2,\text{–},6.6) \cdot 10^{-5}\mathrm{ph,cm^{-2},s^{-1}}$, was einer ^{26}Al-Masse von $M_{\mathrm{Al},,\mathrm{empirical}} = (1.7,\text{–},5.0) \cdot 10^{-5}\mathrm{M_\odot}$ entspricht. Diese gemessenen Werte berücksichtigen, dass die Orion-Region vor der galaktischen Ebene liegt, die ebenfalls 1.809,MeV Gammastrahlen emittiert. Die physikalischen Modelle führen zu einer signifikanten Liniendetektion der Orion-Eridanus-Superbubble mit einer Signifikanz von bis zu $\sigma = 5.6$, mit einem 1.809,MeV Linienfluss von $F_{1809,,\mathrm{physical}} = (3.09^{+0.55}{-}0.39) \cdot 10^{-5}\mathrm{ph,cm^{-2},s^{-1}}$. Dies entspricht einer ^{26}Al-Masse von $M\mathrm{Al},,\mathrm{physical} = (2.3 \pm 0.4) \cdot 10^{-5}\mathrm{M_\odot}$, was konsistent mit dem Ergebnis des empirischen Modells ist. Aus dem Vergleich physikalischer Modelle finden wir, dass Orion OB 1a dominant in der Produktion und Verteilung von ^{26}Al ist. Aus Populationssynthese konstruieren wir Zeitprofile für die vier Untergruppen in Orion OB1 und finden eine heutige Gesamtmasse an ^{26}Al von $M_{\mathrm{Al},,\mathrm{pop}} = (0.002,\text{–},1.9) \cdot 10^{-4}\mathrm{M_\odot}$. Wir detektieren die Orion-Eridanus-Superbubble

zum ersten Mal signifikant bei 1.809,MeV. Das Ergebnis des physikalischen Modells unterstützt Superbubble-Evolutionsmodelle, die zur Beschreibung der Morphologie der Orion-Eridanus-Superbubble verwendet werden. Die Populationssynthese bestätigt Sternentwicklungsmodelle, die eine ^{26}Al-Erwartung liefern, die mit der 1.809,MeV Beobachtung der Orion-Eridanus-Superbubble vereinbar ist.

Contents

1 Introduction

The radioactive isotope ^{26}Al is a product of nucleosynthesis in massive stars. ^{26}Al is unstable and β^+-decays, after an intermediate lifetime with the half-life $T_{1/2} = 7.17 \cdot 10^5$ yr. In the decay, gamma-rays with 1.809 MeV are emitted. Due to the distinct energy from the ^{26}Al decay, these gamma-rays are an observable tracer for the ^{26}Al, in the form of a 1.809 MeV line flux. This 1.809 MeV line emission from ^{26}Al decay was first detected by the HEAO-C spacecraft in 1984 [Diehl et al., 1995]. Another instrument that traced the 1.809 MeV emission is the imaging telescope COMPTEL aboard the Compton Gamma Ray Observatory (CGRO). The all-sky map from this mission at 1.809 MeV is shown in Fig. 1. The map shows a structured emission along a wide longitude, with an asymmetry relative to the Galactic center [Diehl et al., 1995]. Therefore, the ^{26}Al is positioned in

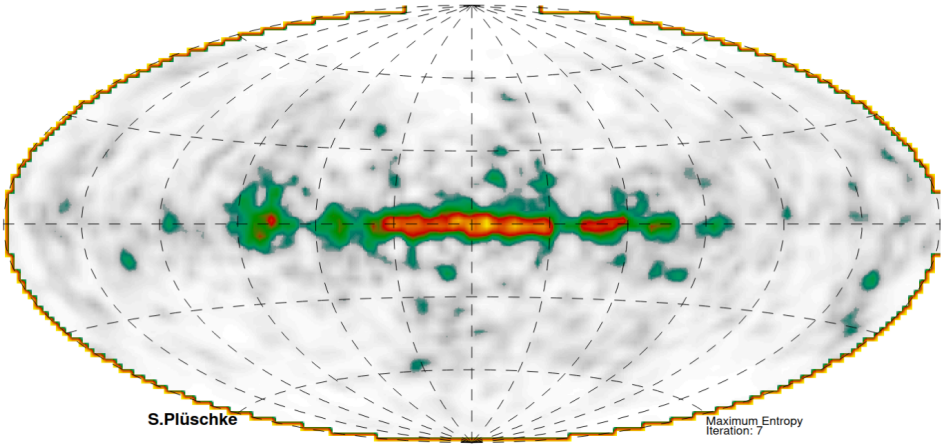

Fig. 1: The all-sky map from the imaging telescope COMPTEL at 1.809 MeV. Figure taken from Plüschke et al. [2001]

localised regions, rather than concentrated in the inner disk of the Galaxy. The dominant Galactic plane is then the accumulation of such regions. Outside of the inner Galactic disk, small structural features in the 1.809 MeV map support the statement of localised ^{26}Al regions. These regions are superbubbles, i.e., density cavities formed by the output of massive stars, which are filled with the ^{26}Al produced in these massive stars. Most massive stars are born in OB associations and transport radioactive isotopes into the interstellar medium with stellar wind or in supernova (SN) explosions. Another radioactive isotope with intermediate lifetime is ^{60}Fe, which also produces distinct gamma-ray emission during decay. In our work, we focus on ^{26}Al, because the output of ^{26}Al in

massive stars is higher than the output of ^{60}Fe [Limongi and Chieffi, 2018]. In previous observations, superbubbles that are connected to known OB associations have been significantly detected in the 1.809 MeV gamma-ray line, e.g. the Cygnus region around Cygnus X-1 with a significance of $\sigma = 10.9$ and the Scorpius Centaurus region around the Upper Scorpius and the Upper Centaurus Lupus with a significance of $\sigma = 6.1$, by Siegert [2017], measured with INTEGRAL/SPI over ≈ 11 yr. The nearest production site of massive stars, the OB star complex in Orion, has not yet been detected significantly at 1.809 MeV. Nonetheless, in the Orion region, a superbubble is observed in H_I, Hα, and in thermal X-ray emission. The Orion Eridanus superbubble (OES) which is considered the result of the energy output from the massive stars in the Orion region. The INTEGRAL mission obtained data, with information about the all-sky 1.809 MeV line emission, until early 2025. Therefore, a larger dataset is now available to analyse the Orion region with INTEGRAL/SPI, compared to the previous analysis. Thus, we motivate this work with the intention to detect a significant 1.809 MeV line flux from the Orion region. In addition, in Pon et al. [2014], two possible OES morphologies arise from model fitting. An analysis of these two geometries leads to a deeper understanding of the ^{26}Al distribution and movement in the OES. To examine the Orion region with the OES and to analyse the morphology of the OES, we structure this thesis as follows. In Chapter 2, we introduce superbubbles and the associated physics, from their stellar composition to the formation of super bubbles, as well as the OES with current knowledge about its morphology and the massive star groups it contains. In Chapter 3, we show the instrument used throughout the thesis INTEGRAL/SPI, with its data analysis. Here, we also show the dataset, the instrumental background in the dataset, applied model optimisation methods, and a test-statistical analysis of the Orion region with initial models. In Chapter 4, we follow two approaches in modelling the ^{26}Al sky. One with empirical models (Sec. 4.1) based on the CGRO/COMPTEL all-sky map from Plüschke et al. [2001] and the INTEGRAL/SPI all-sky map from Bouchet et al. [2015] at 1.809 MeV; and one with physical models (Sec. 4.2), where we built upon the geometrical models from Pon et al. [2014] with the information of the Orion OB1 association. The expected stellar output from this OB association is evaluated with a population synthesis, i.e., in our work, an accumulation of single-star ^{26}Al output over time profiles. All our results for the different modelling approaches are displayed in the two sections, respectively. In Chapter 5, we discuss the ^{26}Al mass distribution in the Orion region and the ^{26}Al localisation inside the OES, as well as the morphology for the OES, with our results from the ^{26}Al sky modelling. Here we also discuss the sound speed inside the OES and the observed velocity with respect to the Sun from the spectral analysis. Finally, we summarize the results and findings of this work in a conclusion in Chapter 6.

2 The Physics of Superbubbles

Superbubbles are a common feature of the interstellar medium (ISM) in galaxies throughout the universe. This Chapter deals with superbubbles, beginning with their evolution. Subsequently, the OES, which is the focus of this thesis, will be examined in detail.

2.1 Evolution of Superbubbles

Superbubbles arise from the combined mechanical and radiative output of massive stars, i.e., stellar winds, ultraviolet radiation, and SNe. In Weaver et al. [1977], the various phases of the expansion of an interstellar bubble were derived. The term "interstellar bubble" describes the interaction via winds and ionizing radiation of a single massive star with its surroundings [Krause et al., 2013]. The formation begins with a spherical symmetric stellar wind that blows through the ambient interstellar gas, assuming a uniform atomic density. Stellar wind is the mass loss of stars in an approximately steady outflow of particles [Pleintinger, 2020]. This leads to an expanding spherical system consisting of four distinct zones throughout its evolution. This system is called Bubble. The zones are

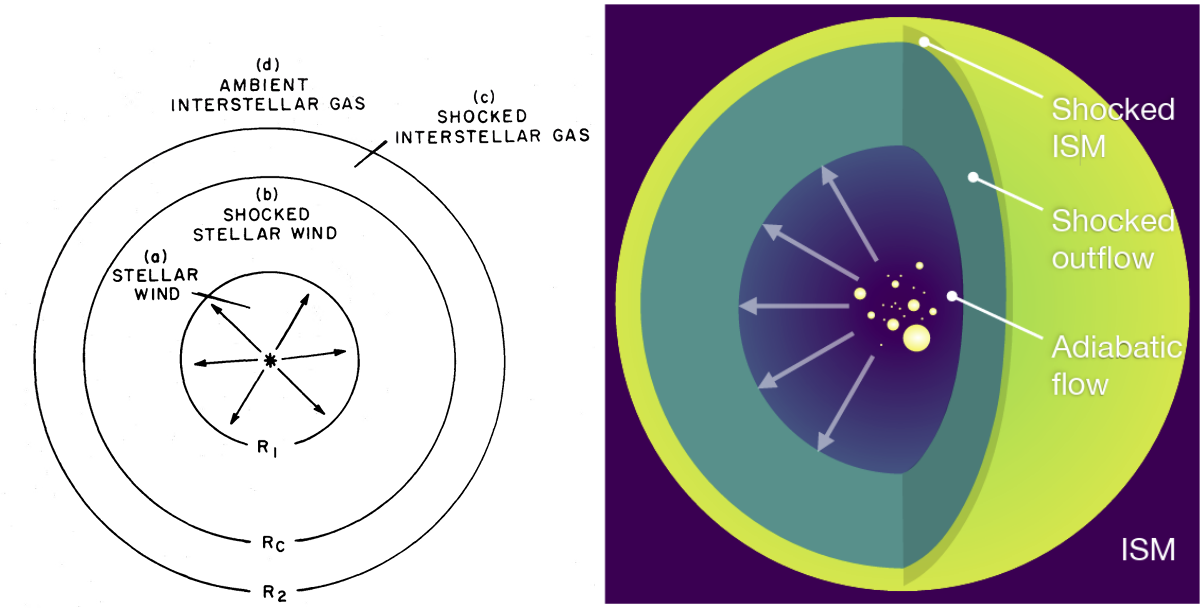

Fig. 2: Schematic regions and boundaries of the flow in a single star interstellar bubble taken from Weaver et al. [1977], (Left), and the corresponding schematic flow phases in superbubble evolution taken from Pleintinger [2020], (Right).

(a) the hypersonic stellar wind, (b) a region of shocked stellar wind, (c) a shell of shocked interstellar gas, and (d) ambient interstellar gas [Weaver et al., 1977]. These zones are displayed in Fig. 2, on the left. The first evolutionary phase is the adiabatic flow. The expansion is too fast for radiative cooling to become efficient, and each region is described as adiabatic expansion. In the second phase, radiative losses cause the expanding swept-up interstellar gas in region (c) to collapse into a thin shell. In this phase, there is still energy conserved in the shocked stellar wind in region (b). In the last phase, radiative cooling becomes efficient enough to cool region (b), leading to a drop in the pressure in this region. The expansion of the outer regions of the bubble decelerates [Weaver et al., 1977]. The resulting interior structure of an interstellear bubble of age $t = 10^6\,\mathrm{yr}$ is shown in Fig.3, for a stellar wind luminosity of $L_\omega = 1.27 \cdot 10^{36}\,\mathrm{erg\,s^{-1}}$ and an atomic density of $n_0 = 1\,\mathrm{cm^{-1}}$. The density in region (a), the hypersonic stellar wind, scales according to the continuity equation with $n_\omega \propto r^{-2}$. The stellar wind encounters a shock at R_1. The shocked stellar wind is hot ($T \gtrsim 10^6\,\mathrm{K}$) and of low density in region (b) [Weaver et al., 1977]. The shell (region (c)), i.e., swept-up ambient gas, consists either entirely of $\mathrm{H_{II}}$ or contains an outer layer of $\mathrm{H_I}$ if the stellar radiation is insufficient to photoionize all the gas in the shell [Weaver et al., 1977]. Stellar groups are spatially centered. Therefore, the

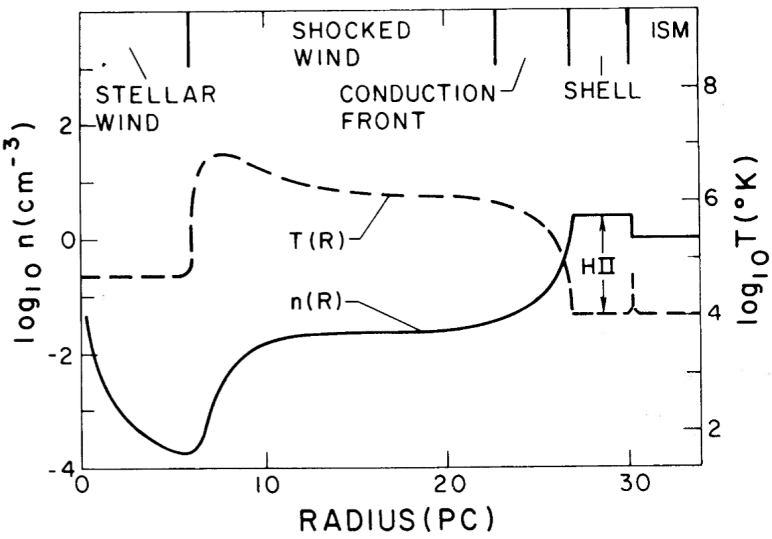

Fig. 3: Large-scale temperature and density features of an interstellar bubble of age $t = 10^6\,\mathrm{yr}$. Figure taken from Weaver et al. [1977].

different phases of spherical expansion for an interstellar bubble also apply when considering the combined output of many stars on a larger scale in superbubbles (typically a few 100 pc in size) [Pleintinger, 2020]. This is shown schematically in Fig. 2, on the right. When considering more than one star, in addition to the radiation and stellar winds, SNe feed the ambient medium. When SNe blast through the bubble, the gas is photoionised in the shock. This leads to a distinct Hα-emission from inside the bubble, during the first $\sim 10\,\mathrm{Myr}$ [Pleintinger, 2020].

2.1.1 Stellar Content

The stellar content in superbubbles is important for investigating the contribution of individual stars and stellar groups to their formation and evolution. Information about the stellar content is provided by an initial mass function (IMF). First constraints on this fundamental astrophysical distribution were published by Salpeter in 1955, introducing the mass function $\xi(M)$ [Chabrier, 2003].

$$\xi(M) \approx 0.03(\frac{M}{\mathrm{M}_\odot})^{-1.35} \tag{1}$$

For stars with the mass $0.4\,\mathrm{M}_\odot < \mathrm{M} < 10\,\mathrm{M}_\odot$ [Salpeter, 1955]. For consistency we name the power-law index for $\log(\xi(\mathrm{M}))$ α and the power-law index for $\log(\xi(\log \mathrm{M}))$ Γ. Thus, the Salpeter IMF has the power-law index $\alpha_{Sal} = 2.35$.
The IMF, following such a power-law, has since been supplemented by additional mass ranges, and the power-law index α has been further constrained. Kroupa [2001] summarizes the constraints on the different mass regimes as a multi-part power-law IMF with the power-law indices:

$$\begin{aligned}
&\xi(M) \propto M^{-\alpha_i} \\
&\alpha_0 = 0.3 \pm 0.7, \quad 0.01 \leq M/\mathrm{M}_\odot < 0.08 \\
&\alpha_1 = 1.3 \pm 0.5, \quad 0.08 \leq M/\mathrm{M}_\odot < 0.50 \\
&\alpha_2 = 2.3 \pm 0.3, \quad 0.50 \leq M/\mathrm{M}_\odot < 1.00 \\
&\alpha_3 = 2.3 \pm 0.7, \quad 1.00 \leq M/\mathrm{M}_\odot
\end{aligned} \tag{2}$$

, where $\xi(M)dM$ is the number of single stars in the mass interval M to $M + dM$. The Kroupa IMF is therefore applicable to a variety of masses and is not as top-heavy (producing as many massive stars) as the Salpeter IMF. The IMF describes the distribution of main sequence stars, which eventually evolve off the main sequence. Therefore, the present-day mass function (PDMF) differs from the IMF. A minimum turnoff mass is defined as the mass for which the age at which the star starts leaving the main sequence equals the age of the respective stellar cluster. For the Galactic disk with an age $\approx 10\,\mathrm{Gyr}$ this minimum turnoff mass would be $m_{TO} \approx 0.9\,\mathrm{M}_\odot$. Stars with masses above m_{TO} will have evolved as red giants, white dwarfs, neutron stars, or black holes to the present day. The PDMF of massive stars has been calculated by Scalo [1986] and gives the power-law indices [Chabrier, 2003]:

$$\begin{aligned}
&\alpha_0 = 5.37, \quad 0 \leq log(M) < 0.54 \\
&\alpha_1 = 4.53, \quad 0.54 \leq log(M) < 1.26 \\
&\alpha_2 = 3.11, \quad 1.26 \leq log(M) < 1.80
\end{aligned} \tag{3}$$

, with a higher α than what we have for the IMF and less Massive stars. The difference between the IMF and the PDMF can be seen as the fraction of massive stars that is already extinguished, via SNe explosions or due to leaving the main sequence in one of the other ways mentioned. The diverging PDMF from the IMF at the minimum turnout mass is shown schematically in Fig. 4.

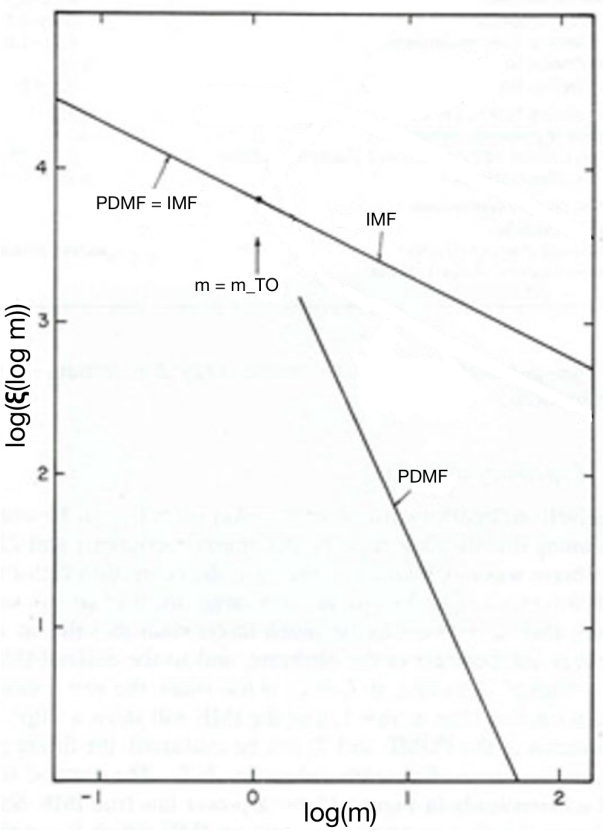

Fig. 4: Schematic parting between the IMF and the PDMF for masses above the minimum turnout mass, m_{TO}. The PDMF is steeper because the proportion of massive stars that have already died increases with increasing mass. Figure adapted from Scalo [1986].

2.1.2 Massive Stars

The output from stars and their influence on the surrounding ISM is called stellar feedback. This stellar feedback is dominated by massive stars and is the driving source in superbubble creation. Thus, it is important to understand how and where massive stars form, how they produce elements, and how they feed the ISM with these elements [Krause et al., 2014]. For this, we need to understand the general physical principles in massive stars and the processes that lead to nucleosynthesis [Lugaro and Chieffi, 2010].

Stellar Structure Equations

In the first approximation, a star is a gaseous spherical symmetric cloud contracting under its own gravity. It progressively heats up while it loses energy from the surface in the form of photons. The photon flux is pushed outwards due to a high temperature gradient, with a decreasing temperature from central to outer regions in the star. The energy absorbed by the gas ΔU, in dependence on the energy gained from the gravitational field $\Delta\Omega$ is given by the Virial theorem: $\Delta U = \Delta\Omega/3(\gamma - 1)$. Here, γ is the ratio between the two specific heats of the gas. One at constant pressure and one at constant volume. This results in a quasi-stable equilibrium configuration for $\gamma > 4/3$. This is given for an ideal gas ($\gamma = 5/3$) but also in a star during the evolutionary phases described in the following. If γ is below 4/3, no energy must be released from the system to contract the gas further, and the system collapses [Lugaro and Chieffi, 2010]. In hydrostatic equilibrium, the pressure is

$$\frac{dP}{dr} = -G\,M\,\rho\,r^{-2} \tag{4}$$

, with M being the interior mass, $G = 6.67430 \cdot 10^{-11} \frac{\mathrm{m}^3}{\mathrm{kgs}^2}$ being the gravitational constant, and ρ being the density at a given radius r within the star. With the mass continuity equation:

$$\frac{dM}{dr} = 4\pi\,r^2\,\rho \tag{5}$$

If we assume ρ to be constant to zero order within the star, the integration of eq. 5 shows:

$$\rho \propto \frac{M}{R^3} \tag{6}$$

Because of low pressure at the surface of the star and high pressure in the center of the star, the equation of hydrostatic equilibrium, eq. 4, becomes:

$$P_C \propto \frac{M\rho}{R_S} \tag{7}$$

, where P_C is the central pressure and R_S is the stellar radius. When relation (Eq. 6) is inserted in relation (Eq. 7) it reads:

$$P_C \propto \frac{M^2}{R_S^4} \tag{8}$$

For an ideal gas, the equation of state gives:

$$P \propto \frac{\rho T}{\mu} \tag{9}$$

, where T is the temperature and μ is the mean molecular weight.

If we insert eq. 9 in eq. 8 we get:

$$T_C \propto \frac{\mu M}{R} \tag{10}$$

Leaving us with the basic relation between the temperature in the core T_c, the mass M, and the stellar radius R_S. The energy flux through the structure in a stationary situation is given via Fick's law as:

$$\frac{dT}{dr} = \frac{-3\kappa\rho L}{16ac\pi^2 T^3} \tag{11}$$

, where κ is the opacity of the gas, L the luminosity, a the radiation constant, and c the speed of light. Conservation of energy is controlled by the continuity equation

$$\frac{dL}{dr} = 4\pi^2\rho\epsilon \tag{12}$$

, where ϵ represents the net local energy budget. This energy budget is the sum of the nuclear production rate ϵ_{nuc}, the neutrino energy losses, and the gravitational energy range. Due to the high temperature gradient between the center and the surface of the star, the central temperature can be described as:

$$T_C^4 \approx \frac{ML}{R^4} \tag{13}$$

Combining this relation with the relation (Eq. 10) that results from hydrostatic equilibrium gives the fundamental relation between luminosity and mass [Lugaro and Chieffi, 2010]:

$$L \approx \mu^4 M^3 \tag{14}$$

Solving the stellar structure equations requires heavy numerical calculations. Due to similarities between the numerical solutions for different stars, there are analytical scaling relations, called homology relations [Pols, 2011]. These lead to a radius-mass relation depending on the energy production rate mode ν for $\epsilon_{nuc} \propto \rho T^\nu$. ν varies in different nuclear burning phases. For stars on the main sequence, this is shown in Tab. 1 for the two possible branches in hydrogen fusion. With the pp-chain dominating in low mass and the CNO-cycle dominating in high mass main sequence stars.

	ν	R	T_c	ρ_c
pp-chain	$\nu \approx 4$	$R \propto M^{0.43}$	$T_c \propto \mu M^{0.57}$	$\rho_c \propto M^{-0.3}$
CNO cycle	$\nu \approx 18$	$R \propto \mu^{2/3} M^{0.81}$	$T_c \propto \mu^{1/3} M^{0.19}$	$\rho_c \propto \mu^{-2} M^{-1.4}$

Tab. 1: Homology relations for pp-chain and CNO-cycle dominated main-sequence stars.

Hertzsprung-Russel Diagram

Inserting the homology relations and the mass-luminosity relation (Eq. 14) in the Stefan-Boltzman-law

$$L = 4\pi R^2 \sigma T_{eff}^4 \tag{15}$$

, where $\sigma = 5.67040 \cdot 10^{-5} \frac{\text{erg}}{\text{cm}^2\,\text{s}\,\text{K}^4}$ is the Stefan Boltzman constant and T_{eff} the effective temperature [Pols, 2011], gives two temperature luminosity relations. One for the pp-chain dominated low mass main sequence stars and one for the CNO-cycle dominated high mass main sequence stars:

$$L_{low-mass} \approx T^{7.8} \qquad L_{high-mass} \approx T^{25} \tag{16}$$

When we compare these estimated values with the observational luminosity L(T) in a Hertzsprung-Russell diagram (HRD), for 22000 stars from the Hipparcos and 1000 from the Gliese catalog (see Fig. 5), we find that the low-mass power-law slope describes the cool part of the main sequence approximately. From the observation we estimate the power-law slope α of L(T) between 3000 K – 6000K to be $\alpha_{low-mass} \sim 8$, for the hot part 7500 K – 16000 K we estimate a power-law slope of $\alpha_{high-mass} \sim 5$. The high-mass L(T) homology expectation does not match the observation. This can be explained with the Humphreys-Davidson limit that sets in at high temperatures (∼10000 K) and is an upper limit for stellar luminosity depending on T_{eff} [Pols, 2011].

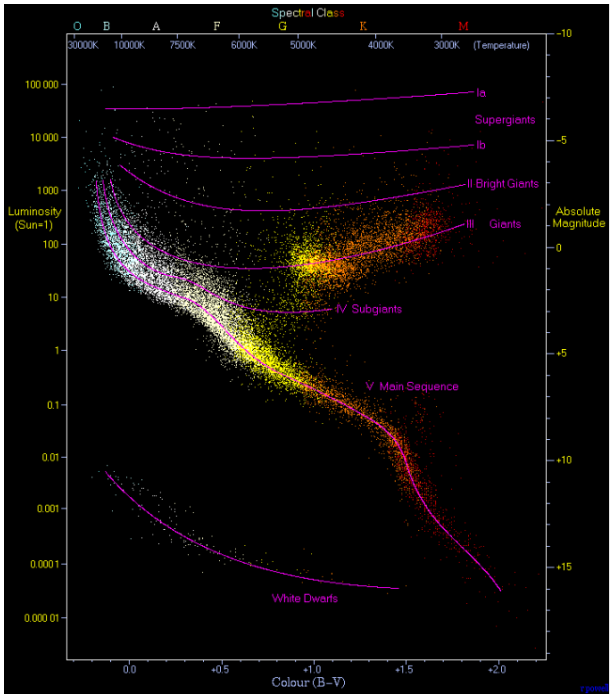

Fig. 5: Hertzsprung–Russell diagram constructed from 22000 stars in the Hipparcos Catalogue and 1000 nearby stars from the Gliese Catalogue. It should be noted that the x-axis is scaled according to spectral classes, resulting in a compressed representation of the temperature. Figure taken from Mignard [2019].

The HRD shows that most of the stars are on the main sequence, fusing hydrogen to helium. When the central hydrogen reservoir is burned up, they leave the main sequence on a path dependent on their original mass, their metallicity, and rotational velocity [Pleintinger, 2020].

Convection

The transportation of locally produced energy in stars via radiation or conduction is frequently too slow, so that interior shells can become unstable since a displacement from the equilibrium position is not fully counteracted by a restoring force. Instead, matter accelerates even further away from its original position and convection sets in, i.e., large-scale motions of matter [Lugaro and Chieffi, 2010]. This is visible when illustrating how the stellar structure equations look in a real star. This can be done in a Kippenhahn diagram (Fig.6). For a star with $M = 5\,\mathrm{M}_\odot$, the early evolution is comparable to a

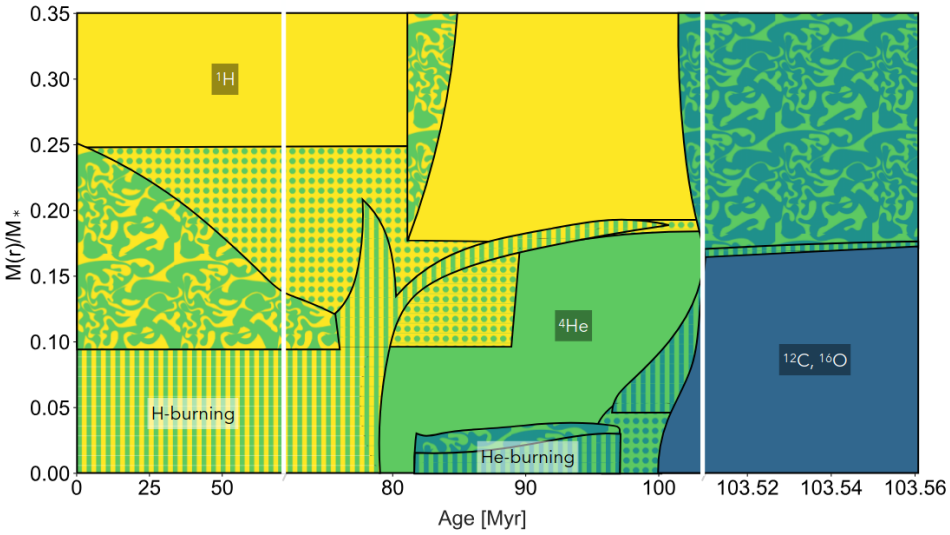

Fig. 6: Kippenhahn diagram showing the structural evolution of a $5\,\mathrm{M}_\odot$ star. For three phases, the core burns different elements starting with hydrogen.When there is no more hydrogen in the center, helium core burning sets in. After that, the helium burning moves into the shell, and a core mainly out of ^{12}C and ^{16}O evolves. Here, the star has left the main sequence. Figure taken from Pleintinger [2020].

Solar-type star with hydrogen burning in the center and the fuel hydrogen at the surface. The core and the hydrogen are linked with convection (marbled) and mixed (dotted) regions [Pleintinger, 2020]. After central hydrogen burning, the core is H-exhausted and made primarily from He. The H-burning shifts to the base of the H-rich mantle, while the star expands up to 1000 times the Solar radius. This expansion triggers large-scale convection from the star's surface to the center. This can be seen at about 80 Myr and is called the first dregde-up. During this process, the He-core increases in mass, as the H-burning products fall onto the core [Lugaro and Chieffi, 2010]. When the core density

reaches about $10^6\,\mathrm{g\,cm^{-3}}$ He-burning ignites and the star ascends in the Asymptotic Giant Branch (AGB) in the HRD [Pleintinger, 2020].

Nuclear Burning

The observed lifetime of a star supersedes the Kelvin-Helmholtz timescale, i.e., the lifetime of a contracting gas cloud under its gravity. The energy cannot be from the gravitational energy reservoir alone. Instead of simple contraction, nuclear reactions activate in the stellar core in the different burning phases. The energy rate of these nuclear reactions is dependent on the abundance of the reactant nuclei and the cross section of the reaction averaged over a Maxwellian distribution [Lugaro and Chieffi, 2010]. For burning heavier elements, the central temperature needs to increase while the abundance of lighter elements (with bigger reaction cross sections) needs to decrease. This happens mainly in massive stars ($M > 8\,\mathrm{M_\odot}$), that reach these central temperatures, when the lighter elements are burned up. The most abundant element is hydrogen. Burning hydrogen happens as long as a star is on the main sequence, and therefore for most of the star's lifetime. The two hydrogen-burning processes, i.e., producing alpha particles out of protons, are the pp-chain and the CNO-cycle.

The pp-chain ignites at temperatures of $\approx$ 10 MK when the stellar mass exceeds $0.08\,\mathrm{M_\odot}$. The pp-chain begins with proton on proton fusion and builds up through a sequence of proton captures and β-decays, which is displayed in Tab. 2. Because of a low cross section for the ^{3}He proton capture and due to no existing nuclei with atomic number A=5 (^{4}He proton capture), successive proton capture stops early at these two isotopes. To overcome the non-existence of A=5, enough ^{3}He must be produced to activate the capture of this nucleus by another ^{3}He or a ^{4}He nucleus [Lugaro and Chieffi, 2010]. If ^{3}He is captured by ^{4}He, ^{7}Be is created and the pp-chain branches in the ppII- or ppIII-chain, for electron or proton capture respectively [Siegert, 2017].

The second process, the CNO cycle, becomes efficient for temperatures of $\approx$20 MK. The temperature is significantly higher than where the pp-chain ignites, due to the high Coulomb barrier in the CNO nuclei. The CNO cycle starts with the proton capture on a ^{12}C nucleus, resulting in radioactive ^{13}N. ^{13}N decays via β^+ into ^{13}C. ^{13}C captures also a proton, fusing ^{14}N. Proton captures by ^{14}N, result in radioactive ^{15}O, that β^+-decays into ^{15}N. Proton fusion with ^{15}N leads to ^{12}C and an α-particle. This sequence is called the CN-cycle. For temperatures T$\sim$25 – 30 MK another branch of the CNO cycle becomes efficient. Instead of proton and ^{15}N fusing an α-particle, the ^{15}N captures the proton resulting in ^{16}O. The proton capture of ^{16}O forms radioactive ^{17}F, that β^+-decays to ^{17}O. ^{17}O captures a proton in a compound nucleus that either splits into ^{14}N and an α-particle, or turns into ^{18}F. That particle is radioactive and β^+-decays to ^{18}O. Proton capture on ^{18}O preferrentially split into ^{15}N and an α-particle or fuse ^{19}F. The different processes are shown in Tab. 2. Because all the proton captures and subsequent decays pro-

duce another isotope that is part of the CNO cycle, the total abundance of these isotopes is constant. For temperatures exceeding 25 – 30 MK the full cycle becomes efficient and a quasi-equilibrium establishes, in which the abundance of each isotope reaches a steady state value dependent on its production and destruction [Lugaro and Chieffi, 2010].
If the stellar mass is sufficient to reach temperatures of T≈40 – 50 MK, proton capture on ^{19}F, from the CNO leads to ^{20}Ne. This starts the next sub cycle of hydrogen fusion via proton captures and subsequent β^+-decays on ^{20}Ne, ^{21}Ne, ^{22}Ne, ^{23}Na, in the NeNa cycle, until an equilibrium value between these isotopes sets in. If the temperature exceeds ∼50 MK, proton capture by ^{23}Na becomes a possibility, competing with the ^{23}Na(p,α)^{20}Ne channel. As the temperature rises, the proton capture becomes more efficient and the processes for the resulting ^{24}Mg and further are activated step by step until, at ∼60 MK, the entire NeNaMgAl cycle is activated and the equilibrium ratios of all nuclei between ^{20}Ne and ^{27}Al are established. The NeNaMgAl cycle leaks to heavier elements than ^{27}Al. This means that processes, such as additional proton captures, are producing heavier elements outside of the NeNaMgAl cycle. The processes of the NeNaMgAl cycle are shown in Tab. 2 [Lugaro and Chieffi, 2010].

reaction	Q_{tot} [MeV]
ppI main sequence $0.08 \leq M/M_\odot$	$10\,\mathrm{MK} \leq T \lesssim 14\,\mathrm{MK}$
$p + p \rightarrow d + e^+ + \nu$	1.442
$d + p \rightarrow {}^3He$	5.494
$^3He + {}^3He \rightarrow {}^4He + 2p$	12.860
ppII	$14\,\mathrm{MK} \lesssim T \lesssim 23\,\mathrm{MK}$
$^3He + {}^4He \rightarrow {}^7Be$	1.587
$^7Be + e^- \rightarrow {}^7Li + \nu$	0.862
$^7Li + p \rightarrow {}^8Be \rightarrow \alpha + \alpha$	17.347
ppIII	$T \gtrsim 23\,\mathrm{MK}$
$^3He + {}^4He \rightarrow {}^7Be$	1.587
$^7Be + p \rightarrow {}^8B$	0.14
$^8B \rightarrow {}^8Be + e^+ + \nu \rightarrow \alpha + \alpha$	18.209
CNO cycle: dominant for stars: $M \gtrsim 1.3 M_\odot$; $T \gtrsim 23\,\mathrm{MK}$	
$^{12}C + p \rightarrow {}^{13}N$	1.944
$^{13}N \rightarrow {}^{13}C + e^+ + \nu$	2.220
$^{13}C + p \rightarrow {}^{14}N$	7.551
$^{14}N + p \rightarrow {}^{15}O$	7.297
$^{15}O \rightarrow {}^{15}N + e^+ + \nu$	2.754
$^{15}N + p \rightarrow {}^{12}C + \alpha$	4.966
CNO sub-cycle:	$25\,\mathrm{MK} \lesssim T \lesssim 30\,\mathrm{MK}$
$^{15}N + p \rightarrow {}^{16}O$	12.127
$^{16}O + p \rightarrow {}^{17}F$	0.600
$^{17}F \rightarrow {}^{17}O + e^+ + \nu$	2.761
$^{17}O + p \rightarrow {}^{14}N + \alpha$	1.192
$^{17}O + p \rightarrow {}^{18}F$	5.607
$^{18}F \rightarrow {}^{18}O + e^+ + \nu$	1.656
$^{18}O + p \rightarrow {}^{15}N + \alpha$	3.981
$^{18}O + p \rightarrow {}^{19}F$	7.994

reaction	Q_{tot} [MeV]
NeNaMgAl cycle	$40\,\mathrm{MK} \lesssim T \lesssim 60\,\mathrm{MK}$
$^{20}Ne + p \rightarrow {}^{21}Na$	5.979
$^{21}Na \rightarrow {}^{21}Ne + e^+ + \nu$	3.548
$^{21}Ne + p \rightarrow {}^{22}Na$	6.739
$^{22}Na \rightarrow {}^{22}Ne + e^+ + \nu$	2.842
$^{22}Ne + p \rightarrow {}^{23}Na$	8.794
$^{23}Na + p \rightarrow {}^{20}Ne + \alpha$	2.377
$^{23}Na + p \rightarrow {}^{24}Mg$	11.693
$^{24}Mg + p \rightarrow {}^{25}Al$	6.548
$^{25}Al \rightarrow {}^{25}Mg + e^+ + \nu$	4.277
$^{25}Mg + p \rightarrow {}^{26}Al$	6.307
$^{26}Al \rightarrow {}^{26}Mg + e^+ + \nu$	4.004
$^{26}Al + p \rightarrow {}^{27}Si$	12.275
$^{26}Mg + p \rightarrow {}^{27}Al$	8.271
$^{27}Si \rightarrow {}^{27}Al + e^+ + \nu$	4.812
$^{27}Al + p \rightarrow {}^{28}Si$	11.585
$^{27}Al + \alpha \rightarrow {}^{24}Mg$	1.601

Tab. 2: Hydrogen burning nucleosynthesis processes that build up elements from hydrogen to silicon. Each reaction is associated with an energy release Q_{tot} determined by the mass defect. The Table is adapted from Siegert [2017].

In stars burning these heavier elements, the central density increases and with it the interior temperature. Here, neutrino cooling becomes important, as electromagnetic radiative cooling is not efficient enough, and with neutrinos leaving the surface of the star nearly

unhindered. When stars are so massive that after burning all the hydrogen in their core, the He core has a mass of $\sim 0.35\,M_\odot$, they continue to contract, reaching central temperatures of 10^8 K. This happens if the initial mass was $M \gtrsim 2\,M_\odot$. At this temperature and density in the core, the fusion of two α-particles directly into carbon becomes efficient in the triple-α-process and He-burning ignites (Tab. 3). A large jump in luminosity and radius of the star accompanies the ignition of the triple-α-process. If the He core is lighter than $\sim 0.35\,M_\odot$, electron degeneracy is sufficient to counteract gravity without the need of additional contraction [Lugaro and Chieffi, 2010, Siegert, 2017].

When hydrogen is burned up in the core, H burning shifts to the outer layers, and a He core builds. The same process happens when He is burned up in the core, with He-burning shifting away from the center. The He-exhausted remaining core needs a mass of $\gtrsim 1.1 M_\odot$ to overcome electron degeneracy. If not, an electron degenerate core consisting of C and O forms. The minimum star mass to overcome the electron degenerate CO core is $\sim 9-12\,M_\odot$. In stars with masses higher than $\sim 6-8\,M_\odot$ carbon burning ignites. This gives a range between $\sim 6-12\,M_\odot$, where in a partially degenerate CO core carbon burning ignites and lifts the degeneracy. Stars with this mass will not be able to overcome the formation

reaction	
He burning, triple-α process:	$M \gtrsim 2\,M_\odot$, $T \gtrsim 100$ MK
$\alpha + \alpha \rightarrow {}^{8}\mathrm{Be}$	
${}^{8}\mathrm{Be} + \alpha \rightarrow {}^{12}\mathrm{C}$	
C burning, massive stars:	$M \gtrsim 8\,M_\odot$, $T \gtrsim 500$ MK
${}^{12}\mathrm{C} + {}^{12}\mathrm{C} \rightarrow {}^{20}\mathrm{Ne} + \alpha$	
${}^{12}\mathrm{C} + {}^{12}\mathrm{C} \rightarrow {}^{23}\mathrm{Na} + p$	
${}^{23}\mathrm{Na} + p \rightarrow {}^{20}\mathrm{Ne} + \alpha$	
${}^{23}\mathrm{Na} + p \rightarrow {}^{24}\mathrm{Mg}$	
${}^{12}\mathrm{C} + \alpha \rightarrow {}^{16}\mathrm{O}$	
Ne burning:	$T \gtrsim 120$ MK
${}^{20}\mathrm{Ne} + \gamma \rightarrow {}^{16}\mathrm{O} + \alpha$	
${}^{20}\mathrm{Ne} + \alpha \rightarrow {}^{24}\mathrm{Mg}$	
${}^{24}\mathrm{Mg} + \alpha \rightarrow {}^{28}\mathrm{Si}$	

reaction	
O burning:	$M \gtrsim 9\,M_\odot$, $T \gtrsim (150 \ldots 260)$ MK
${}^{16}\mathrm{O} + {}^{16}\mathrm{O} \rightarrow {}^{28}\mathrm{Si} + \alpha$	
${}^{16}\mathrm{O} + {}^{16}\mathrm{O} \rightarrow {}^{31}\mathrm{P} + p$	
${}^{16}\mathrm{O} + {}^{16}\mathrm{O} \rightarrow {}^{31}\mathrm{S} + n$	
${}^{31}\mathrm{S} \rightarrow {}^{31}\mathrm{P} + e^+ + \nu_e$	
Si burning:	$M \gtrsim 8 \ldots 11\,M_\odot$, $T \gtrsim (2.7 \ldots 3.5)$ GK
${}^{28}\mathrm{Si} + {}^{28}\mathrm{Si} \rightarrow {}^{56}\mathrm{Ni}$	
${}^{28}\mathrm{Si} + (1 \ldots 7)\alpha \rightarrow {}^{32}\mathrm{S} \ldots {}^{56}\mathrm{Ni}$	

Tab. 3: Advanced nuclear burning stages in massive stars. For He-burning the associated energy released Q_{tot} in units of MeV is given in brackets. The Table is adapted from Siegert [2017].

of an electron-degenerate ONeMg core, after central C-burning. Stars beyond $\sim 9-12\,M_\odot$ go through the subsequent central burning phases and end in core collapse SNe [Lugaro and Chieffi, 2010].

When central Si-burning ignites, all elements up to ^{56}Fe are produced, with the highest bounding energy per nucleon. The star cannot gain energy from nuclear fusion to heavier elements, and the energy to sustain itself under gravity runs out, leading to the collapse of the star. Right before collapse, the star shows an onion-like structure with the different burning phases layering above the iron core [Siegert, 2017]. The processes associated with the different central burning phases are shown in Tab. 3.

Supernovae

The iron core in a late massive star collapses when it reaches its Chandrasekhar mass limit. Free-fall sets in, until a density of $\gtrsim 2{\cdot}10^6\,\mathrm{g\,cm^{-3}}$ in a massive star with $25\,\mathrm{M}_\odot$ as example is reached. For this density, the interior of the star heats up to $5-10\,\mathrm{GK}$, leading to thermal gamma-rays. The gamma-rays photodisintegrate the iron in the core, and a neutron star emerges within $\sim$ 1s. The sudden change in the equation of state leads to a rebound of the central core from the compact object, in the form of a shock wave going outwards. This shockwave interacts with the rest of the different layers falling inwards. The shock leads to the complete disruption of the star. This is called core collapse SNe. In the shock region, due to the initial nuclear composition of the star and the temperatures reached in the shock, explosive nucleosynthesis occurs [Siegert, 2017]. The radiation energy, inside the shockfront, scales with the temperature according $E_{SN} \propto T^4$. This leads to zones of different explosive burning phases, which are shown in Fig. 7. The energy also scales with the radius of the shockfront; therefore, the burning phases of heavier isotopes are dominant

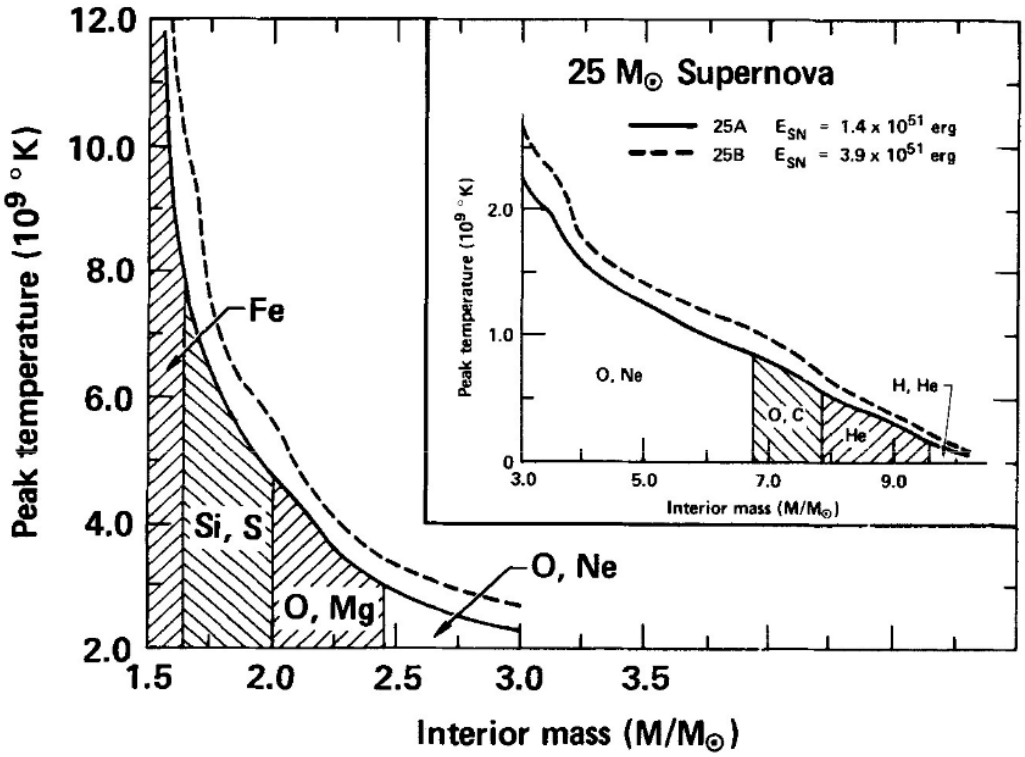

Fig. 7: Peak temperature in the iron core collapse SN shockfront as a function of the mass fraction, for a star with the mass $25\,\mathrm{M}_\odot$. Different zones of explosive burning occur. The dashed line is a second stellar model with a different explosion energy than the one shown with the solid line. Figure taken from Siegert [2017].

in explosive burning. The different isotopes that are produced can either be emitted into the ISM or fall back onto the neutron star, depending on their mass and the production region, defining a mass cut [Siegert, 2017]. In addition to iron core dissociation, stellar cores can collapse via two different mechanisms. First, via electron capture reactions in

stars not heavy enough to ignite central Ne-burning, and were stable due to the electron degeneracy of the NeOMg-core. Second, electron positron pair-production in stars with $M \gtrsim 100 M_\odot$ after C-burning. These reduce the substantial thermal energy to counteract gravity and the core collapses [Pleintinger, 2020]. For stars with masses between 9 – 120 $M_\odot$, iron core SNe dominate the collapse mechanism [Siegert, 2017].

From Remnants to Superbubbles

The energy released in a core-collapse SNe is on the order of $\sim 10^{51}$ erg during a few seconds. After the shockwave - launched by this - sweeps through the stellar envelope, it propagates in the surrounding ISM with a velocity of $3000 - 5000\,\mathrm{km\,s^{-1}}$. This expansion is the supernova remnant (SNR). The ambient region may be evacuated due to a wind-driven bubble formation in earlier life stages of the star. SNR can be described in three phases. Starting with the free expansion in the first phase. Here, the surrounding ISM pressure is negligible. The radius of the SNR increases linearly to the velocity of the ejecta, v_{ej}:

$$R_{free}(t) = v_{ej} t \tag{17}$$

During free expansion, ISM gas is accumulated in the shock front, building up a reverse shock. This leads to an efficient deceleration of the expansion when the swept-up mass matches the ejecta mass. Here, the phase of free expansion goes into the second, the Sedov-Taylor phase. This phase is an ejecta-dominated adiabatic expansion and lasts over $10^4 - 10^5$ years. The Sedov-Taylor phase is comparable with the adiabatic expansion in the wind-driven formation of interstellar bubbles. During this phase, the radius of the SNR increases according to:

$$R_{Sedov-Taylor}(t) \propto (\frac{E_{SN}}{\rho_0})^{\frac{1}{5}} t^{\frac{2}{5}} \tag{18}$$

, with the total energy of the SN, E_{SN} and pre-shock ISM density ρ_0. The third phase is the snowplough phase. Matter is continuously swept up during expansion, and the expansion decelerates. The radius evolves here with:

$$R_{Snowplough}(t) \propto (\frac{\mu}{\rho_1})^{\frac{1}{4}} t^{\frac{1}{4}} \tag{19}$$

, with the total momentum of the expanding shell μ and the density in the swept up shell ρ_1. Due to the "snowploughing" of matter the density ρ_1 is increased in regard to ρ_0 [Pleintinger, 2020, Shull, 1995]. The evolution of a SNR in the three phases is shown in Fig.8. The effects of stellar wind forming interstellar bubbles and SNe forming SNR on the ambient ISM are similar, even though their composition is different. When these two mechanisms happen at overlapping time and space, they accumulate to a large-scale expansion. Due to the majority of massive stars forming in OB associations simultaneously,

massive stars are spatially correlated. Superbubbles are driven by the stellar winds and SNRs of an entire OB association, rather than having a single stellar wind driving source [Mac Low and McCray, 1988].

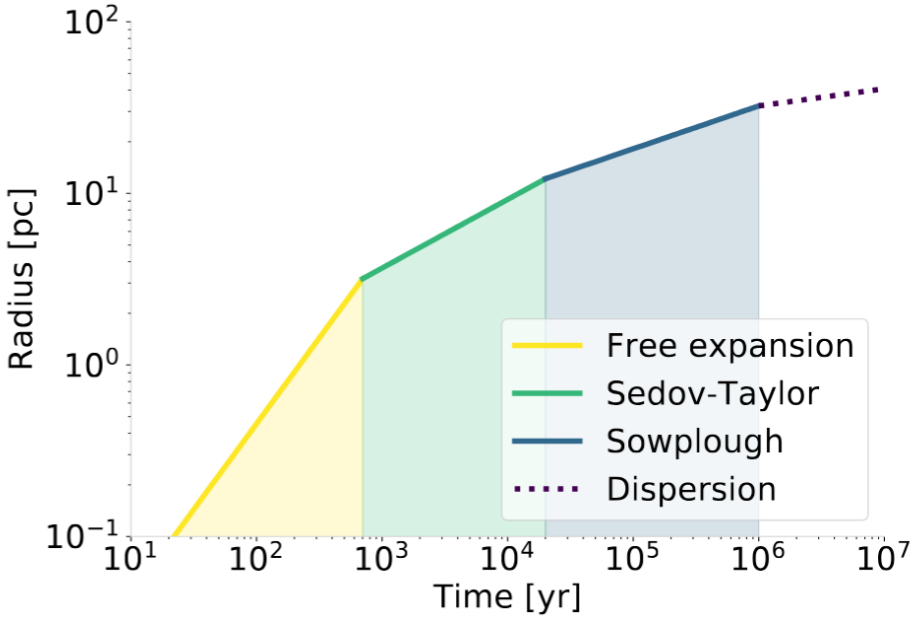

Fig. 8: Schematic evolution of a SNR in three phases. The expansion is similar to the expansion in wind-driven interstellar bubble formation. Figure taken from Pleintinger [2020].

Yields

The isotopes that are produced in the explosive burning, according to the pre-SN composition of the star, are blown into the ISM with the expansion of the SNR. Isotopes produced earlier in the star's evolution are additionally blown out of the gravitational field of the star in the stellar wind. When entering the ISM, isotopes are called yields, differing between the stellar wind yields and the SN yields. A star's evolutionary path, dependent on its initial mass, its rotational velocity, and its metallicity, i.e., the enrichment of the stellar gas from previous stellar nucleosynthesis, controls the composition of these ejecta. The nuclear processes in stars are not directly accessible. Thus, calculations of nucleosynthesis yields that can be compared to measurements are an important tool. Radioactive isotopes such as ^{60}Fe, ^{44}Ti, and ^{26}Al are of particular interest because they emit distinct gamma radiation, i.e., gamma rays with a specific energy released during the respective radioactive decay. The characteristic lines for ^{60}Fe are at 1.173 MeV and 1.332 MeV[1], for ^{44}Ti are at 67.9 keV, 78.4 keV[2] , and 1.157 MeV, and for ^{26}Al at 1.809 MeV. These gamma-rays are directly observable [Pleintinger, 2020]. Limongi and Chieffi [2018] did such calculations

[1] https://www.esa.int
[2] https://www.sci.esa.int

for stellar evolution models of stars with initial masses of $13\,M_\odot \leq M \lesssim 120\,M_\odot$ and testing the impact of rotational velocities, $0\,\mathrm{km\,s^{-1}} \leq v_{rot} \lesssim 300\,\mathrm{km\,s^{-1}}$ and metallicities, $0 \leq [Fe/H] \lesssim -4$. For the assumption that stars with initial masses $M \geq 25\,M_\odot$ fully collapse to a black hole, these calculations predict yields for ^{26}Al, ^{60}Fe, and ^{44}Ti shown in Fig. 9. Thus, in stars with $M \geq 25\,M_\odot$ only the stellar wind contributes to the total yield of an isotope. We find the ^{26}Al-yields to be higher than the yields of ^{60}Fe. ^{44}Ti only enriches the ISM in stellar models below the full black hole collapse mass.

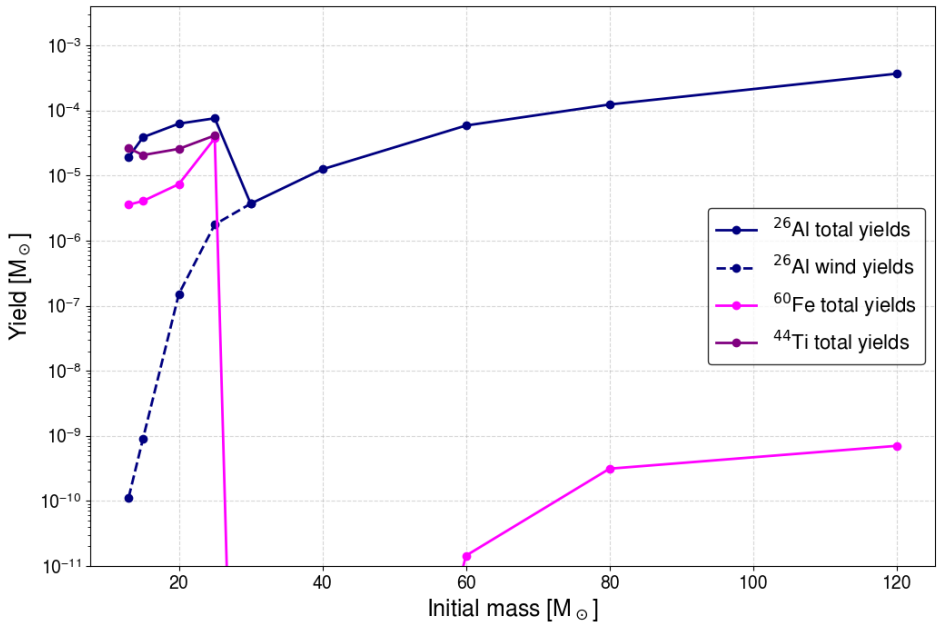

Fig. 9: Yields of the radioactive ^{60}Fe, ^{26}Al, and ^{44}Ti per initial mass from non-rotating stellar models with Solar metallicity by Limongi and Chieffi [2018]. Stars with initial masses $M \geq 25\,M_\odot$ fully collapse into black holes.

When looking at the time profiles of ^{26}Al, ^{60}Fe, and the ^{60}Fe/^{26}Al ratio (Fig. 10), ^{26}Al is ejected from the star prior to ^{60}Fe. ^{60}Fe is produced only during explosive burning, and there is no stellar wind contribution to the ^{60}Fe-yield. Nontheless, due to a higher lifetime ^{60}Fe will dominate the ^{60}Fe/^{26}Al ratio at some point starting at 16 – 30 Myr, depending on the initial mass, considering the Limongi and Chieffi [2018] non rotating stellar models, at Solar metallicity [Pleintinger, 2020]. This thesis focuses on stars with ages up to 10±2 Myr (see Sec. 2.2.4), where ^{26}Al-yields dominate. Thus, in this work ^{26}Al leads to higher model flux predictions than ^{60}Fe, making it more likely to be observable.

^{26}Al from massive Star Winds and Supernovae

^{26}Al is produced in the NeNaMgAl cycle via the proton capture of ^{25}Mg and has an intermediate lifetime of $\sim 1 \cdot 10^6$ yr with the half-life of $T_{1/2} = 7.17 \cdot 10^5$ yr. This lifetime

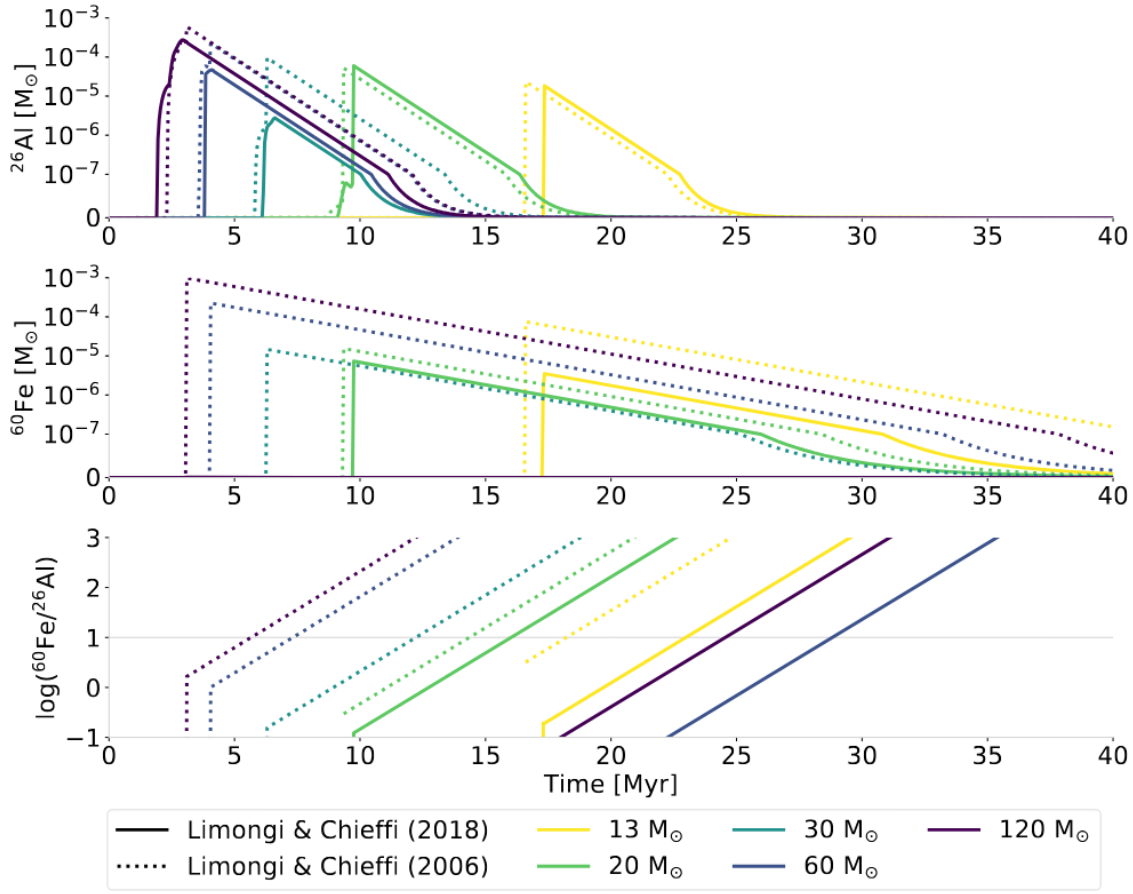

Fig. 10: Time profiles of ^{26}Al- and ^{60}Fe-yields for different initial masses from non-rotating stellar models with Solar metallicity by Limongi and Chieffi [2018] (solid lines) compared to an older model by Limongi & Chieffi from 2006 (dotted lines). Figure taken from Pleintinger [2020].

is on the order of SNR evolution or wind-driven bubble formation, thus the possibility of transporting ^{26}Al into the ISM leads to the yields shown in Fig. 9 via stellar wind and SNe. ^{26}Al decays via two channels (see Fig. 11). The dominant β^+-decay happens with 81.7%, while it decays via electron capture the rest of the time.
The β^+-decay results in the first excited state of the target isotope ^{26}Mg, while producing also a positron and an electron neutrino.

$$^{26}\mathrm{Al} \xrightarrow{\beta^+} {}^{26}\mathrm{Mg}^* + e^+ + \nu_e$$
$$^{26}\mathrm{Mg}^* \rightarrow {}^{26}\mathrm{Mg} + \gamma(1.809\,MeV)$$

While relaxing to the ground state a 1.809 MeV photon is emitted. The electron capture (EC) results in either the higher excited state in 2.7% or the first excited state in 15.5% of cases. Here, no positron is produced, and the energy difference is added to the electron neutrino energy that is again produced.

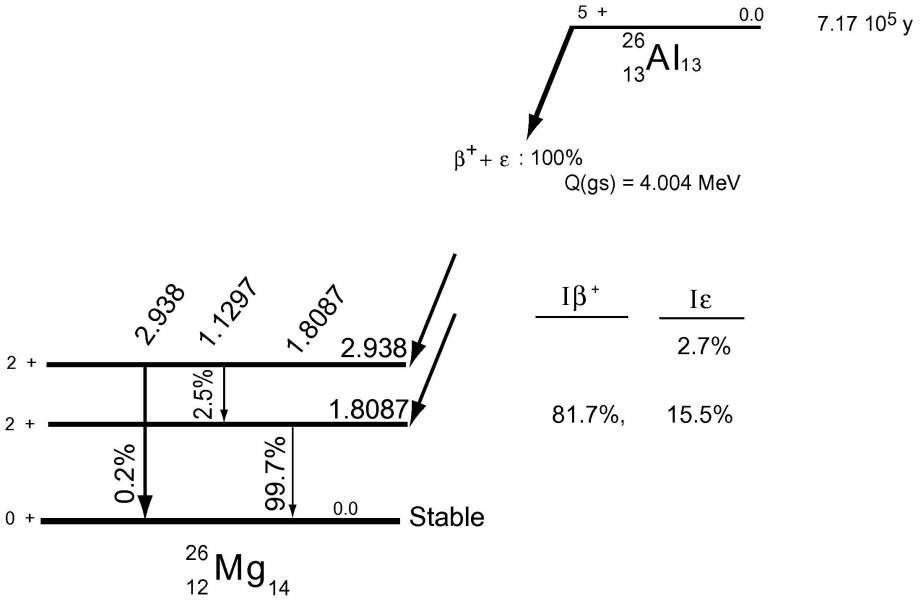

Fig. 11: ^{26}Al decay scheme. The ^{26}Al ground state, with a half-life of $7.17 \cdot 10^5$ yr, decays via positron emission (β^+) or electron capture (ϵ), forming ^{26}Mg in one of two excited states. The higher excited state is reached in 2.7% of the decay. It relaxes to the ground state by directly emitting one gamma-ray photon at 2.938 MeV or via the first excited state emitting two gamma-ray photons at 1.130 MeV and 1.809 MeV. Otherwise, it decays only via the first excited state emitting 1.809 MeV photons. Figure taken from Castillo-Rogez et al. [2009].

The first excited state resulting from electron capture emits the same 1.809 MeV photon as for the β^+-channel.

$$
\begin{aligned}
^{26}\mathrm{Al} &\xrightarrow{\mathrm{EC}} {}^{26}\mathrm{Mg}^* + \nu_e \\
^{26}\mathrm{Mg}^* &\rightarrow {}^{26}\mathrm{Mg} + \gamma(1.809\,\mathrm{MeV})
\end{aligned}
$$

For the higher excited state of ^{26}Mg, two channels in relaxation arise. First, directly going to the ground state, emitting a 2.938 MeV photon for 0.2% of cases, or second, also through the first excited state for 2.5% of cases emitting a 1.130 MeV photon in addition to a 1.809 MeV photon.

$$
\begin{aligned}
^{26}\mathrm{Al} &\xrightarrow{\mathrm{EC}} {}^{26}\mathrm{Mg}^* + \nu_e \\
^{26}\mathrm{Mg}^* &\rightarrow {}^{26}\mathrm{Mg} + \gamma(1.130\,\mathrm{MeV}) + \gamma(1.809\,\mathrm{MeV}) \\
^{26}\mathrm{Mg}^* &\rightarrow {}^{26}\mathrm{Mg} + \gamma(2.938\,\mathrm{MeV})
\end{aligned}
$$

Thus, 99.7% of the decaying ^{26}Al result in a 1.809 MeV gamma-ray line emission. This line dominates the other two gamma-ray lines with the photon flux ratios of $F_{1.8}/F_{2.9} \approx 500$, $F_{1.8}/F_{1.1} \approx 40$ and the 1.809 MeV photon flux $F_{1.8}/F_{e^+} \approx 1.2$ times higher than the positron flux, making the 1.809 MeV gamma-ray line a suitable tracer for cummulative effects of stellar feedback, such as superbubbles.

The dependence of the photon flux $F_{1.8}$ on the ^{26}Al-mass can be derived by describing the radioactive decay statistically with the decay law:

$$\frac{dN(t)}{dt} = -\lambda N(t) \tag{20}$$

, with the particle number N and the decay constant $\lambda = \frac{ln(2)}{T_{1/2}} = 3.07 \cdot 10^{-14}\,\mathrm{s}^{-1}$.
This differential equation can be solved with:

$$N(t) = N_0 \cdot e^{-\lambda \cdot t} \tag{21}$$

Inserting this solution (Eq. 21) back into the differential equation (Eq. 20) leads to the photon luminosity L, of an initial amount of particles N_0 over time.

$$L(t) = \lambda \cdot N_0 \cdot e^{-\lambda \cdot t} \tag{22}$$

Under the assumption of an isotropic emission in all spatial directions with sound speed v_s this translates to the flux $F(d)$:

$$F_{1.8}(d) = \frac{p \cdot \lambda \cdot \frac{M}{m} \cdot e^{-\lambda \cdot d/v_s}}{4\pi d^2} \tag{23}$$

, with the mass of one ^{26}Al atom $m = 25.9797604\,\mathrm{u}$, the total mass of decaying ^{26}Al M, the probability of emitting the 1.809 MeV photon when decaying $p = 99.7\%$, and the distance from the source d.

Massive Star Regions

Massive stars do not evolve separately, but are created simultaneously. This happens in OB associations. In these star groups, stars form out of the same volume in a molecular cloud. OB associations are rather young ($< 20\,\mathrm{Myr}$) compared to the Milky Way (MW) ($> 10\,\mathrm{Gyr}$). This is due to O and B stars forming on the high end of the main sequence in the HRD. O and B stars are therefore short-lived and explode in core collapse SNe a few million years ($< 35\,\mathrm{Myr}$, for the longest-lived massive stars of $M = 8\,\mathrm{M}_\odot$) after formation [Siegert, 2017, Pleintinger, 2020]. This time-scale is well-fitting with the half-life of ^{26}Al, being another advantage in observing the 1.809 MeV gamma-ray line [Siegert, 2017]. The most prominent nearby OB associations, in regard to their ^{26}Al content, are listed in Tab. 4 and can be located in Scorpius-Centaurus (ScoCen), Perseus, Cygnus, and Orion [Pleintinger, 2020]. The 1.809 MeV signature of these regions is also visible in the all-sky 1.809 MeV map, with the image reconstruction from Knödlseder et al. [1999] for the COMPTEL mission, shown in Fig. 12. Also, the Galactic plane is a prominent feature

in this energy, due to the cumulative contribution of many OB associations along the line of sight (LOS) through the Galactic plane. This thesis focuses on the stars in Orion, while Cygnus will be used to validate our analysis methods later.

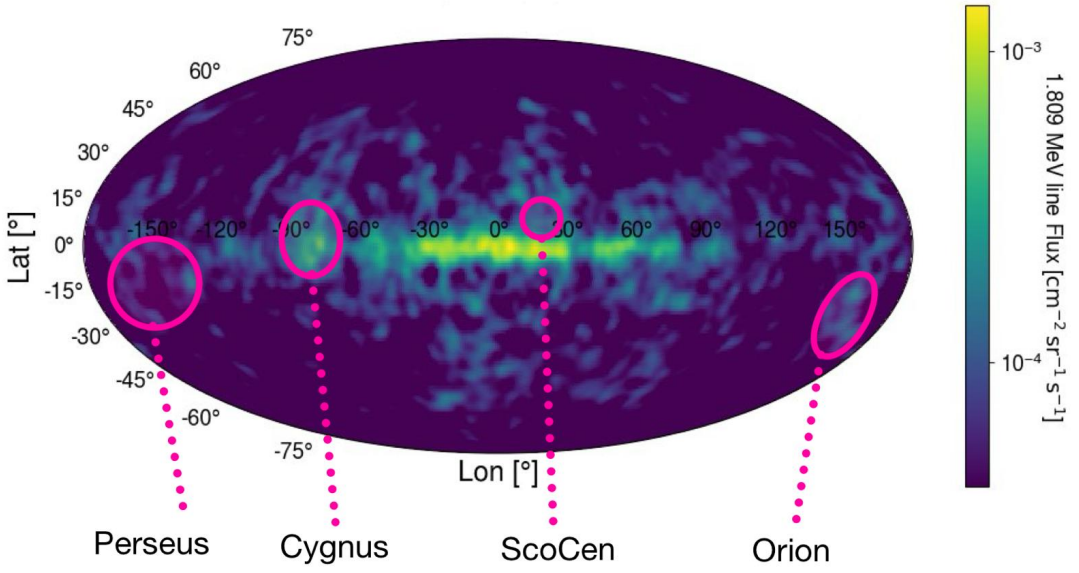

Fig. 12: The 1.809 MeV all-sky map from the COMPTEL mission ([Plüschke et al., 2001]) shows the MW and prominent OB association-containing regions (adapted from Pleintinger [2020]). Spectral analysis focuses on Orion later on, while Cygnus will be analysed to validate the methods.

Population Synthesis

The spatial resolution in MeV measurements is limited to a few degrees [Pleintinger, 2020]. This is due to Compton scattering being the dominant photon interaction at this energy. This resolution is not enough to resolve single stars in the OB associations. Instead, an integrated signal of their combined output is observed. A tool to deal with integrated signals is population synthesis. Population synthesis is based on the approach to describe an integrated signal as the evolutionary contribution of the constituents [Pleintinger, 2020]. These constituents, the stars that are modelled to describe the stellar group of interest, contribute to the total ^{26}Al, with their respective ^{26}Al-yields. The yields can be described by time profiles $\psi(M_\star, t)$ based on stellar models. The sample of stars, used to describe the population, is produced in the integration of the time profiles of single stars over the total mass range weighted with a mass function $\xi(M_\star)$. This mass function is given, either with the PDMF, describing the current composition of a population, or the IMF describing the star formation at age zero of the population. For the IMF, the population synthesis result $\Psi(t)$ needs to be normalised (with factor A) to the total mass

Name	ℓ [°]	b [°]	Distance [pc]	Age [Myr]
Sco-Cen: US	351.5	+20.0	143 ± 6	10 ± 7
Sco-Cen: UCL	331.0	+12.5	136 ± 5	16 ± 7
Sco-Cen: LCC	298.5	+5.5	115 ± 4	15 ± 6
Ori OB1a	201.0	-17.3	~ 300	8–12
Ori OB1b	206.0	-18.0	360–620	2–8
Ori OB1c	209.0	-19.5	~ 385	2–6
Ori OB1d	211.3	-19.5	~ 380	1–2
Cyg OB2	80.2	+0.8	1350–1750	1–7
Cyg OB1	75.5	+1.1	1400	6–8
Cyg OB2	72.9	+1.9	1800	2–12
Cyg OB4	82.8	-7.6	800	...
Cyg OB5	67.1	+2.1	1610	...
Cyg OB6	86.0	+1.0	1700	...
Cyg OB7	89.0	0.0	630	1–13
Cyg OB8	77.9	+3.4	1800	4–6
Cyg OB9	77.7	+1.9	960	2–4
Per OB2	159.2	-17.1	296 ± 17	1–10
Per OB1	147.0	-5.5	175 ± 3	50
Cen OB2	294.3	-1.0	2100	3–10
Per OB1	134.7	-3.2	1800	8–11
Sco OB4 (?)	252.4	+2.4	960	...
Sco OB3	173.1	-0.8	1200	...
Ori OB2 (?)	192.6	-11.6	2040	...

Tab. 4: Nearby OB associations linked to ^{26}Al enriched regions in the sky. For some of these OB associations very little is known indicated with the (?). Table adapted from Wright [2020].

of the population in the end. The population synthesis is then calculated with:

$$\Psi(t) = A \int_{M_{\star,\min}}^{M_{\star,\max}} \psi(M_\star, t)\, \xi(M_\star)\, dM_\star \tag{24}$$

For a population of 100 massive stars in the $8-120\,\mathrm{M}_\odot$ range corresponding to a typical nearby OB association, the population synthesis modelling of ^{26}Al and ^{60}Fe was done in Voss et al. [2009]. The resulting time profiles are shown in Fig. 13. The ejection of ^{26}Al during wind phases starts prior to the ejection of ^{60}Fe, starting with the first SN. Because of the most massive stars exploding earlier, the time profiles show a maximum during the first SNe. Later, the contribution from less massive star SNe shows, while for ^{26}Al the wind contribution decreases with the number of exploded constituents. Population synthesis will be used to evaluate the ^{26}Al output of different subgroups of the Orion OB1 association in Sec. 4.2.3.

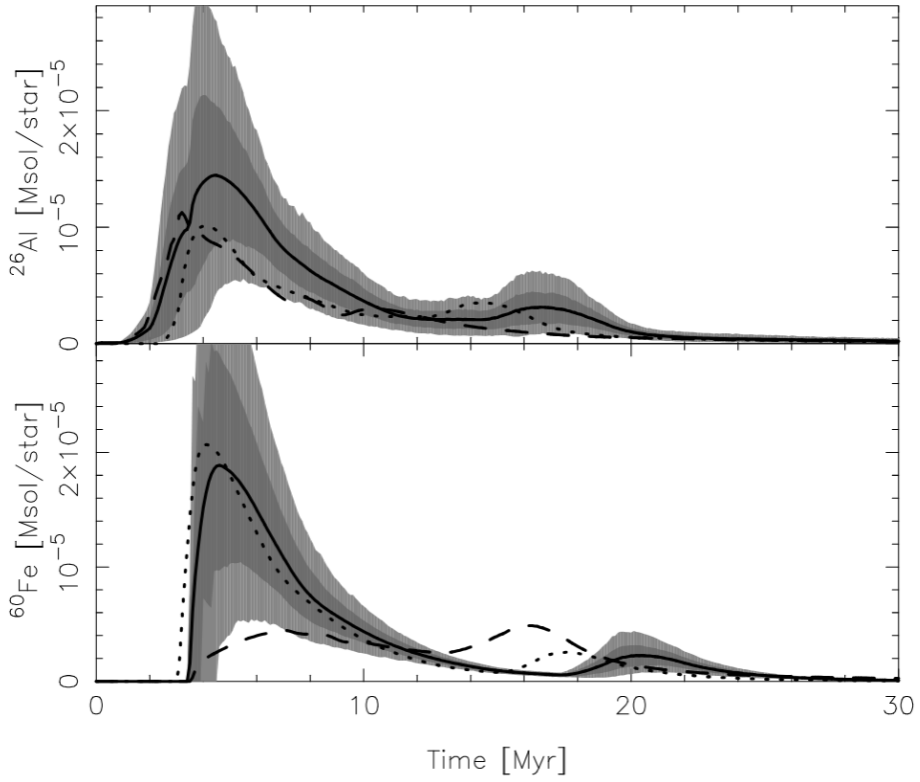

Fig. 13: Time profiles of the ^{26}Al and ^{60}Fe synthesis in a population of 100 massive stars ranging between $8-120\,M_\odot$. The dark grey and grey area are the 1-σ and 2-σ deviation from the best model, while the dashed and dotted lines show alternative stellar evolution models. Figure taken from Voss et al. [2009].

2.2 The Orion Eridanus Superbubble

The OB star complex in Orion is the nearest production site of massive stars to the Sun. With the Orion OB1 association at a distance of $\sim$ 400 pc, this makes a good laboratory for the investigation of the influence on the ISM by massive star groups. The energy output from the Orion OB1 subgroups in stellar wind and SNe can account for the morphology and kinematics of the ambient ISM in this region [Brown et al., 1994]. Here, a large cavity enclosed by atomic hydrogen and filled with hot X-ray gas, between the Solar System and the stellar associations in Orion, lies: The OES. H_I data constrains the bubble to an area of $\approx 2000\mathrm{deg}^2$ between $b = (-5° - -55°)$ and $\ell = (185° - 225°)$ [Siegert, 2017]. The OES was discovered in X-rays, due to its hot interior with the ROSAT all-sky survey and is a neighbor of the Local Bubble [Krause et al., 2014].

2.2.1 Morphology

A first approximation of the OES morphology can be derived with the standard theory for spherical symmetric bubbles (Sec. 2.1), under the assumption of a uniform ISM density surrounding the H_I shell [Brown et al., 1994]. The radius of $\sim$140 pc and expansion

velocities of $15-20\,\mathrm{km\,s^{-1}}$, from observations can be matched, for Orion OB 1a as driving source, assuming a dynamical age of the bubble of $3-5\,\mathrm{Myr}$. As well as estimating the energy needed to disrupt the parental molecular cloud, of the bubble, as the output from Orion OB 1b and Orion OB 1c [Brown et al., 1994]. Thus, in the spherical approximation, the stars in Orion OB1 are a sufficient source in the creation of the OES. Nonetheless, the assumption of a spherical symmetry and a uniform ambient ISM density cannot withhold considering the position of the stars $\sim 130\,\mathrm{pc}$ below the Galactic plane. The density gradient perpendicular to the Galactic plane in the $\mathrm{H_I}$ distribution leads to an elongated superbubble formation extending down to $\sim 300\,\mathrm{pc}$ below the Galactic plane and the OB associations at one end of the bubble rather than in the center [Brown et al., 1994]. The resulting morphology is shown in Fig. 14. In this configuration, the OES is filled with the

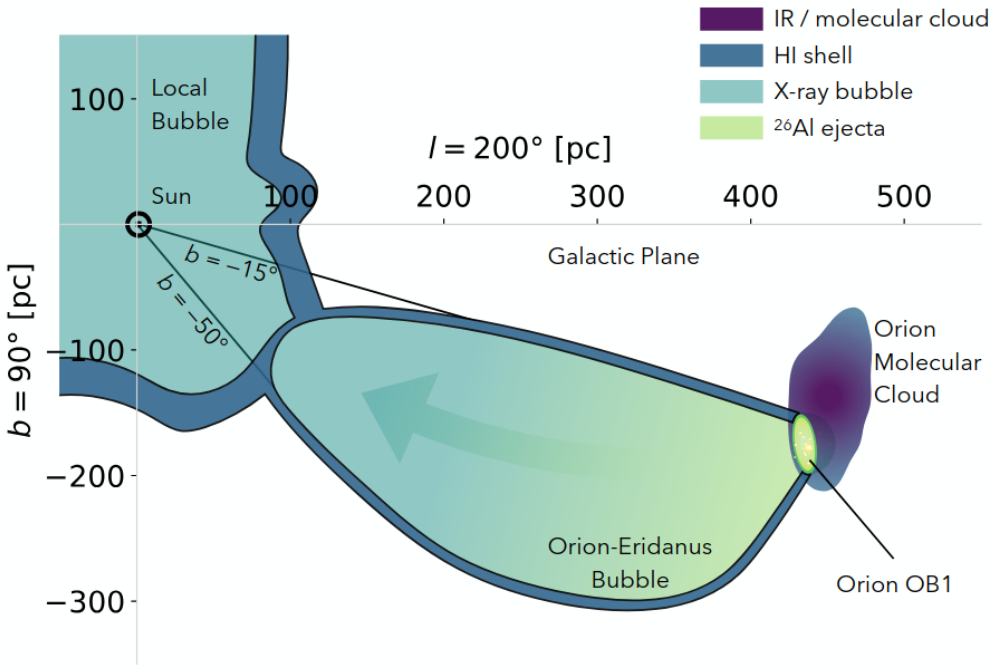

Fig. 14: Schematic morphology for the OES forming in the $\mathrm{H_I}$ pressure gradient below the Galactic plane. The superbubble elongates and forms away of the driving OB association. Yields from the massive stars flow freely into the OES towards the Sun, while they are stopped in the other direction by the Orion molecular cloud. Figure taken from Pleintinger [2020].

yields from the stars in Orion OB1, which flow freely into the evacuated OES, towards the Sun. The Orion molecular cloud located behind the OB association, prohibits the yields from spreading out away from the Sun. With this predominant outflow direction for the ^{26}Al-yields, we expect the ^{26}Al gamma-ray line to be blueshifted, dependent on the sound speed. The sound speed also shapes the morphology of the ^{26}Al distribution in the OES. The emission region is restricted to absolute distances of $1\,\mathrm{pc}\frac{v_s}{1\,\mathrm{km\,s^{-1}}}$ [Siegert, 2017]. Another information about the position and morphology of the OES is given in the

Hα line, from the hot plasma cooling on the inside of the superbubble shell. It is emitted during the recombination of previously dissociated protons and electrons [Pon et al., 2014]. The Hα emission from the Orion region, in combination with the COMPTEL 1.809 MeV and the position of the Orion OB1 subgroups is shown in Fig. 15. Bright features in this line emission constrain the extent of the OES to Barnard's Loop and the Eridanus Filaments, Arc A, B, and C. This boundaries match with the ROSAT observed X-ray emission, which results from the hot plasma inside the superbubble as thermal radiation [Pon et al., 2014]. The resulting shape that fills this space is approximately ellipsoidal.

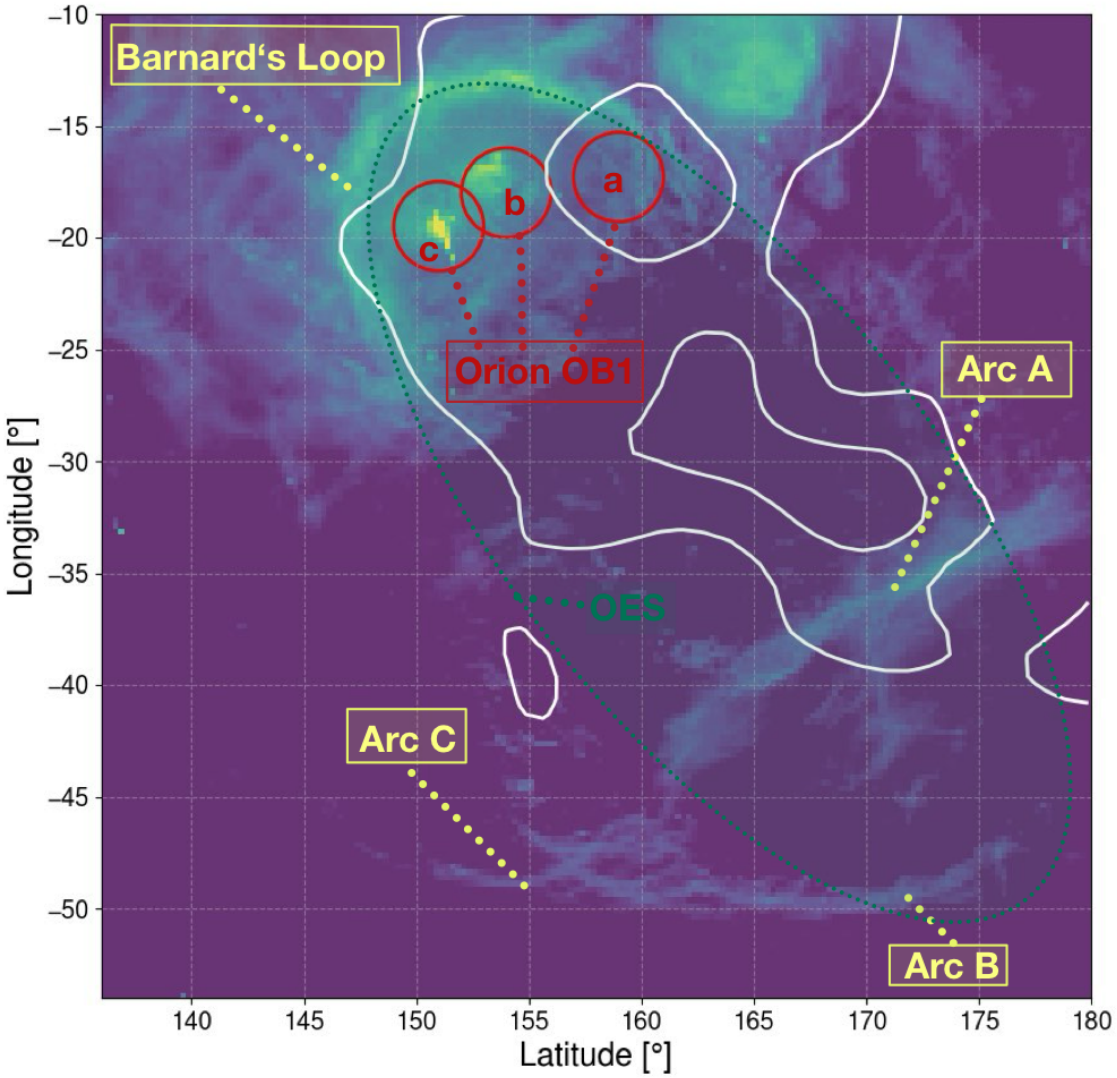

Fig. 15: The OES (indicated in green) in Hα (using the Hα all-sky map from Finkbeiner [2003]). It is located between Barnard's Loop and Arcs A, B, and C (Eridanus filaments). The red circles illustrate the position of the Orion OB1 subgroups 1a, 1b, and 1c, according to Wright [2020]. The white contour plot shows the 1.809 MeV emission, measured by COMPTEL ([Plüschke et al., 2001]), suggesting a spatial offset between ^{26}Al and the younger subgroups (1c and 1b), while matching the position of the oldest subgroup, 1a.

2.2.2 Advanced Superbubble Modelling

The pressure gradient of the H_I distribution leads to a non-spherical symmetric superbubble evolution. A hydrodynamic model that describes this evolution is given by the modified Kompaneets approximation. The approximation found by Kompaneets (1960) was originally developed as a semi-analytic solution to describe the blastwave of a strong nuclear explosion in Earth's atmosphere [Baumgartner and Breitschwerdt, 2013]. This description of a shock wave propagating into a purely exponential atmosphere is also applicable for superbubble evolution in disk galaxies. Since then, this approximation has been modified to allow for gas cooling and a time-dependent energy input rate in the models and has been shown to give excellent first-order solutions on the shape of superbubbles expanding in the Galaxy, e.g., the W4 superbubble, the Ophiuchus superbubble, and the Local Bubble [Pon et al., 2014]. The location of the superbubble wall, in a modified Kompaneets approximation, is

$$r(z, y) = 2H \arccos\left[\frac{1}{2} e^{\frac{z}{2H}} \left(1 - \frac{y^2}{4H^2} + e^{-\frac{z}{H}}\right)\right] \tag{25}$$

, where r is the perpendicular distance from the central axis of the superbubble to the wall, z is the distance along the central axis from the driving source, H is the scaleheight of the exponential atmossphere, and y a dimensionless parameter between $0-2H$ that specifies the evolutionary stage of the superbubble [Pon et al., 2014]. This leads to relatively spherical superbubbles in their early evolutionary stages. A significant elongation sets in when the radius of the bubble reaches the scale height of the exponential atmosphere (y$\sim$H), towards the lower density direction.

Pon et al. [2014] applied this modelling to the OES and compared the resulting models to the Hα image of the superbubble. They derive two possible ellipsoidal solutions that fit the Hα boundaries best. One model has the Eridanus end pointed towards the Sun and one model has the orientation twisted and the Eridanus end pointing away from the Sun. Model T (towards) and model A (away), respectively. These two models are shown in Fig. 16 (Top). How these models are inclined in respect to each other and the Galactic plane becomes clearer when looking at the schematic diagrams of the models in Fig. 16 (Bottom). When going from Model T to model A, the orientation twists inside of Barnard's Loop and Arc A and B switch their position on the shell as Arc A moves from the near side wall to the far side wall of the superbubble. The models A and T will be used in physical modelling of the ^{26}Al-filled OES in Sec. 4.2.

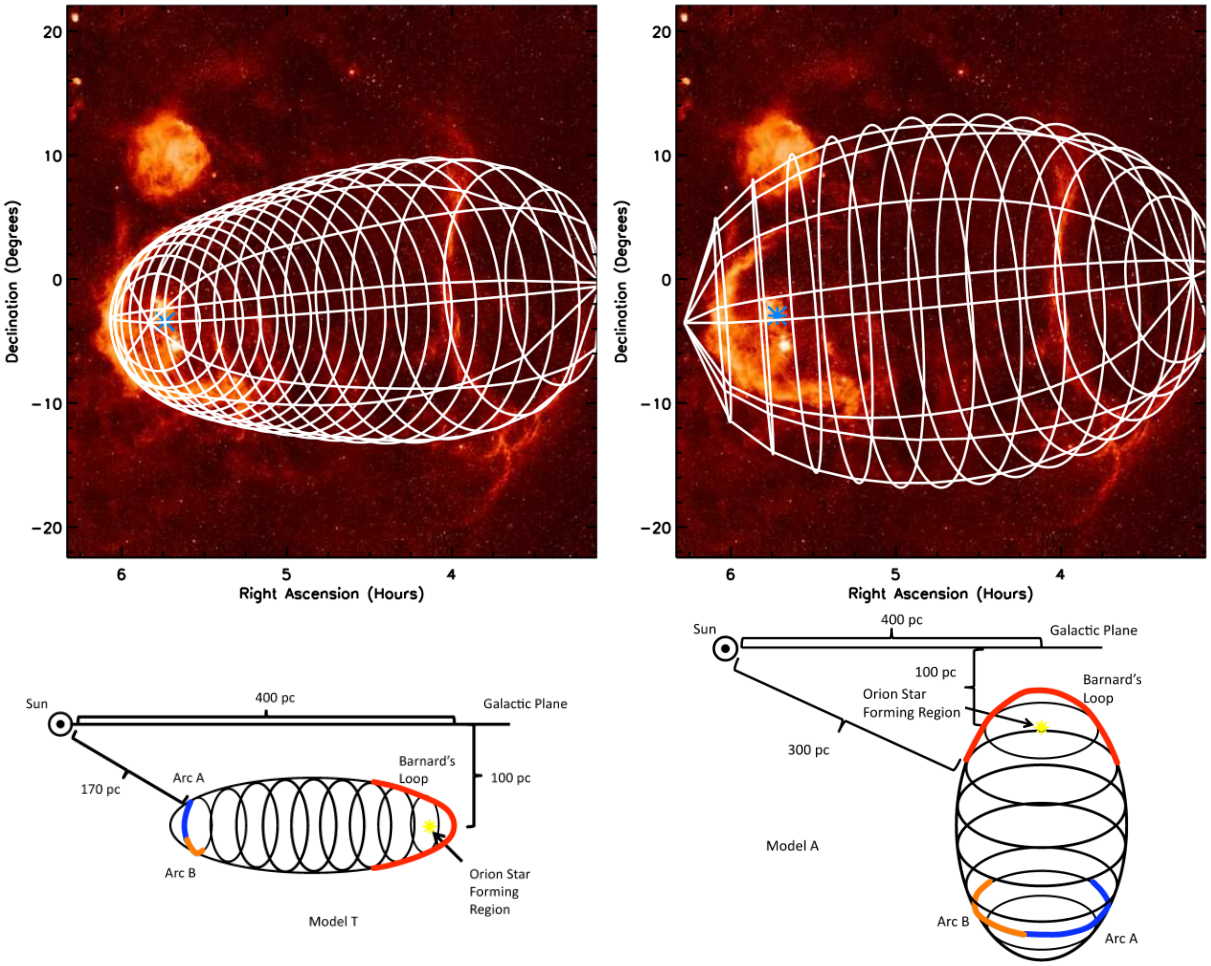

Fig. 16: Top: Best-fitting hydrodynamic model of the OES, in the Hα map. On the left, the model is oriented towards the Sun (Model T), and on the right, the model is pointing away from the Sun (Model A). The blue asterisk denotes the position of the driving source in the model and is located around the Orion OB1 association. Bottom: Schematic diagram for each of the two models (T, left, and A, right). The figures are taken from Pon et al. [2014].

2.2.3 Ellipsoid Parametrisation

We expect the OES to be ellipsoidally shaped. The mathematical description of such a geometry is given in Eq. 26.

$$\frac{x^2}{a^2} + \frac{y^2}{b^2} + \frac{z^2}{c^2} = 1 \tag{26}$$

With a, b, c the main axes of the ellipsoid along the coordinate system axes in x, y, and z direction [Pressley, 2010]. Therefore we can write a matrix $\mathbf{A} = \mathrm{diag}(1/a^2, 1/b^2, 1/c^2)$ for which the ellipsoid is unambigously defined as:

$$\mathbf{x}^T \mathbf{A} \mathbf{x} = 1 \tag{27}$$

With $\mathbf{x}^{\mathrm{T}} = (\mathrm{x},\ \mathrm{y},\ \mathrm{z})$. When rotating the system with the three Pauli matrices $\sigma_{\alpha,\beta,\gamma}$, i.e., the rotation matrices for a given angle around the each coordinate axes, one obtains $\mathbf{A}_{rot}$. This matrix now contains all the information about the extent and orientation of the ellipsoid. To solve for where a LOS $\mathbf{d}$ from the observer position $\mathbf{P}$, cuts through the ellipsoid positioned at (0, 0), we need the quadric given by

$$\mathbf{d}(\theta,\phi) = \begin{pmatrix} \sin\theta\,\cos\phi \\ \sin\theta\,\sin\phi \\ \cos\theta \end{pmatrix} \tag{28}$$
$$\mathbf{d}^T\mathbf{A}_{rot}\mathbf{d} + 2\mathbf{P}^T\mathbf{A} - 1 = 0$$

This can be solved as a quadratic function. We use this in an exemplary model for a rotated ellipsoid observed via the LOS. The 3D setup, as well as the geometrical projection of the ellipsoid in the sky as seen by the observer, are shown in Fig. 17.

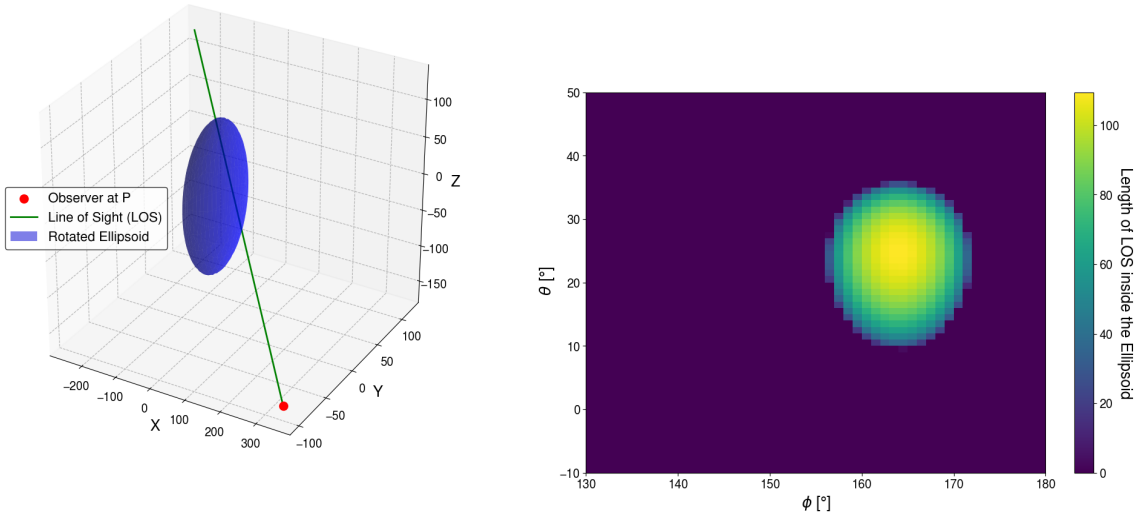

Fig. 17: Exemplary model illustration. Left: Rotated Ellipsoid in the center of the model space with an observer at position P and one LOS. Right: Ellipsoid sky projection, as seen by the observer, using a grid of LOS. The length of the LOS inside the ellipsoid is the distance between the entering and the exit point on the ellipsoid.

We use the following parameters for the exemplary ellipsoidal model setup:

Ellipsoid						**Line of Sight**		**Observer**		
a [au]	b [au]	c [au]	α [°]	β [°]	γ [°]	ϕ [°]	θ [°]	x [au]	y [au]	z [au]
100	50	50	3	-90	-15	160	24	350	-100	-160

Tab. 5: Parameter for the examplary model display in Fig. 17. For the main axes and the coordinate vectors an arbitrary unit (au) is used.

2.2.4 Stars in the OES

The Orion OB1 association is the driving source in the models describing the OES. The four subgroups with different ages (summarized in Tab. 6) are shown in Fig. 18 (left). We

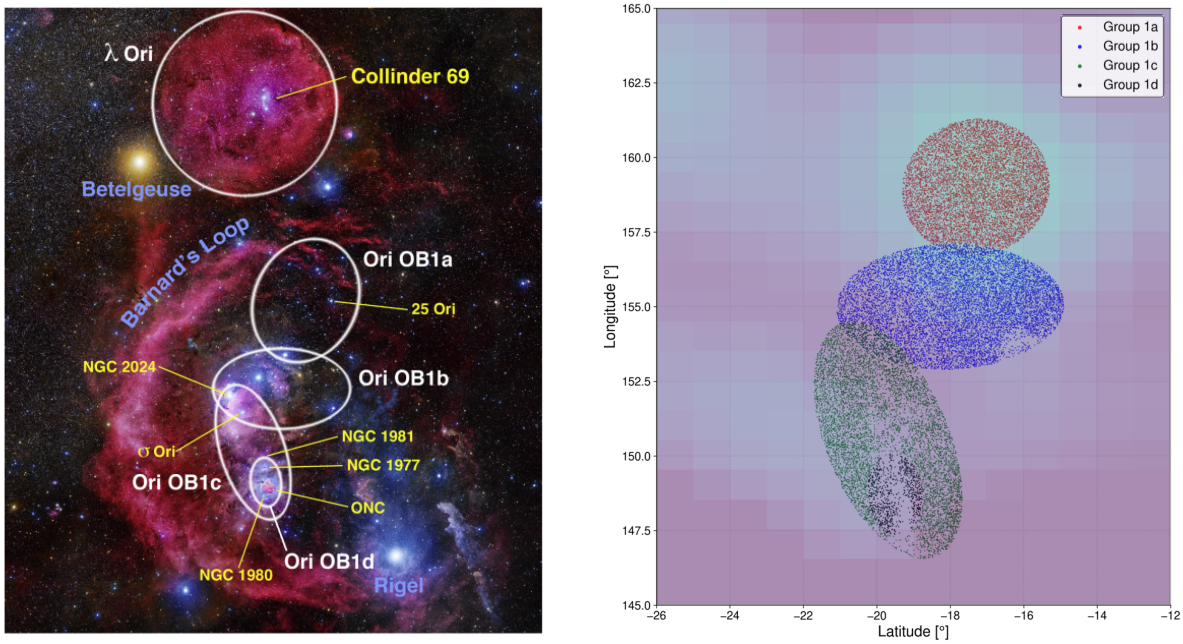

Fig. 18: Left: Wide-field map of the Orion constellation indicating the positions of the four subgroups of the Orion OB1 association. Figure taken from Wright [2020].
Right: Subsets of the GAIA DR3 catalog. Displayed are the positions of stars with known masses in the four subgroups of the Orion OB1 association. In front of the 1.809 MeV map from COMPTEL.

Name	l [°]	b [°]	Distance [pc]	Age [Myr]
Ori 1a	201.0	−17.3	∼ 360	8–12
Ori 1b	205.0	−18.0	360–420	2–8
Ori 1c	209.0	−19.5	∼ 385	2–6
Ori 1d	211.3	−19.5	∼ 380	1–2

Tab. 6: Orion OB1 association subgroups 1a–1d. Excerpt from table 4 according to Wright [2020].

need to estimate the mass of these subgroups to evaluate their ^{26}Al-content in Sec. 4.2.3. For this, we examine the stellar content in the Orion OB1 association further, using the Global Astrometric Interferometer for Astrophysics, GAIA. It launched in 2013 to collect properties of over 1 billion stars, such as their position, parallaxes, and proper motions [Gaia Collaboration et al., 2016]. The magnitude limit for GAIA is $3 \leq G \leq 21$ and the data is publicly available in the GAIA Archive[3] [Lindegren et al., 2018]. Using this, we extract our own sky survey for the Orion region from the GAIA data release 3, which is the latest catalog of the GAIA observation. Only stars for which the mass is known can

[3]https://archives.esac.esa.int/gaia

be used in a statistical analysis of the different Orion OB1 subgroup masses. Thus, we filter the catalog for only stars with a mass estimate for each subgroup, respectively. In Fig. 18 the different subgroups are shown (left) and our catalog subsets for the different subgroups (right). The subset stars are shown in front of the COMPTEL 1.809 MeV map. The hotspot in the COMPTEL map coincides with the position of Ori 1a. Thus, Ori 1a could be the main production site of ^{26}Al in the OES. The size of the four subsets is in the order of 10000 entries for 1a-1c. Only the subset for Ori 1d is smaller.

3 INTEGRAL/SPI

In this chapter, we describe the instrument used throughout this thesis, the spectrometer on INTEGRAL, SPI. Subsequently, we describe SPI data analysis, before testing statistical models in the Orion region with this instrument.

3.1 Gamma-Ray Telescope SPI

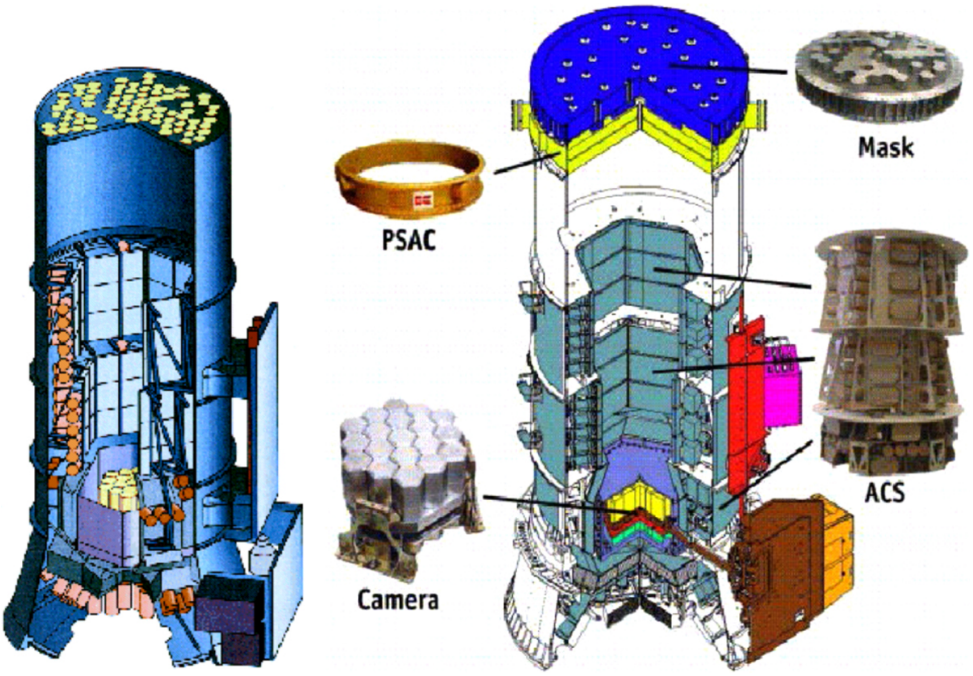

Fig. 19: Schematic (left) and cut-away (right) view of the SPI instrument on INTEGRAL. The instrument consists of a 19-element Ge detector array housed in a cryostat and operated at 80 K, a coded mask of tungsten elements that blocks about half of the detectors in the field of view and a surrounding anti-coincidence system (ACS), vetoing events from cosmic-ray interactions. Figure taken from Diehl et al. [2018].

SPI is the spectrometer on board the ESA mission INTEGRAL (International Gamma Ray Astrophysics Laboratory) [Vedrenne et al., 2003]. INTEGRAL was launched in 2002, into the initial 72-hour orbit with an inclination of 52.2 degrees, a height of perigee of 9000 km, and a height of apogee of 154000 km. With this, the satellite stays outside the radiation belt for 90% of the orbit. This time can be used for scientific observations [Winkler et al., 2003]. INTEGRAL will re-enter Earth's atmosphere in 2029 but was

decommissioned in early 2025 ([Diehl et al., 2018] & ESA[4]). Therefore, INTEGRAL observed space for over 22 yr. SPI is one of the two main instruments on INTEGRAL, and is optimised for high-resolution gamma-ray line spectroscopy in the energy range 20 keV – 8 MeV [Vedrenne et al., 2003]. SPI is equipped with a gamma-ray camera, composed of 19 germanium detectors and a geometrical detection area of 508cm^2. The detector array is cooled to working temperatures of 85 – 90 K in an active cryogenic system. This leads to an energy resolution of 3.1 keV at 1.809 MeV [Siegert, 2017]. The field of view is chosen to be $16^\circ \times 16^\circ$ fully-coded, to examine extended structures as well as point sources. This gives an angular resolution of $\sim 2.5^\circ$ [Vedrenne et al., 2003]. SPI's high spectral resolution makes it unique for observing nuclear lines with regard to nucleosynthesis [Diehl et al., 2018]. Thus, SPI is optimal for studying the ^{26}Al abundance in the Galaxy. SPI and its components are shown in Fig. 19.

3.2 SPI Data Analysis

3.2.1 Event Detection

The raw data, in SPI observations, result from photons that trigger one of the 19 Ge detectors in the camera. These are then counted as events. A shielding of the signal in the field of view is provided by the anti-coincidence system (ACS). The ACS detects photons coming from the background, and with detection triggers a 725 ns window of no event registration in the camera. Thus, the ACS enables filtering out background events that would be indistinguishable from the observed signal in the detectors. Such events arise from charged-particle interactions in the instrument [Diehl et al., 2018]. The measured signal for each event consists of the time of the trigger, the detector identifier, and the signal pulse height. Events that scatter in more than one Ge detector in a coincidence time window of 350 ns are summarized in a Multiple Events (ME) log entry [Diehl et al., 2018]. We expect our sky signal to be composed of Single Events (SE) in the energy regime regarding ^{26}Al. Thus, we choose a dataset of SE throughout the analysis.
The data analysis in SPI is performed for individual energy bins, with the smallest binning of 0.5 keV. SPI observes diffuse emission or point sources in a multitude of pointings. A pointing is an observation unit for a specific region in the sky and a specific amount of time, typically 1800 – 3600 s [Siegert et al., 2019]. The data is pre-processed at INTEGRAL's Data Centre (ISDC). This includes an energy calibration of the pulse height and sorting them in count histograms for each detector. These histograms hold the data in the form of event counts per data space bin $d_{p,j,e}$. The data space is comprised of p being the pointing number, j the detector number, and e the energy bin [Diehl et al., 2018]. The detector numbering is shown in Fig. 20. The pre-processed data is modelled with different

[4] `https://www.esa.int/Science_Exploration/Space_Science/Integral`

model components following the setup in Eq. 29.

$$m_p = \sum_t \sum_g R_{g,p} \sum_{n=1}^{N_S} \theta_{k,t} M_{k,g} + \sum_{t'} \sum_{k=N_S+1}^{N_S+N_B} \theta_{k,t'} B_{k,p} \tag{29}$$

, with $R_{g,p}$, the response function (coded-mask shadowing, see Sec. 3.2.2) applied to $M_{k,g}$, the kth of N_S sky models, for each pixel, g and pointing, p. The N_B, background models, $B_{k,p}$, are independent from the coded-mask shadowing. $\theta k, t$ is the amplitude of the sky models, i.e., a celestial image of the emission (diffuse or point source), changing on a timescale t with regard only to the physics of the source. $\theta k, t'$ is the amplitude of the background model, changing on varying timescale t' for different background events, i.e., the instrument material activating processes that lead to gamma-rays.

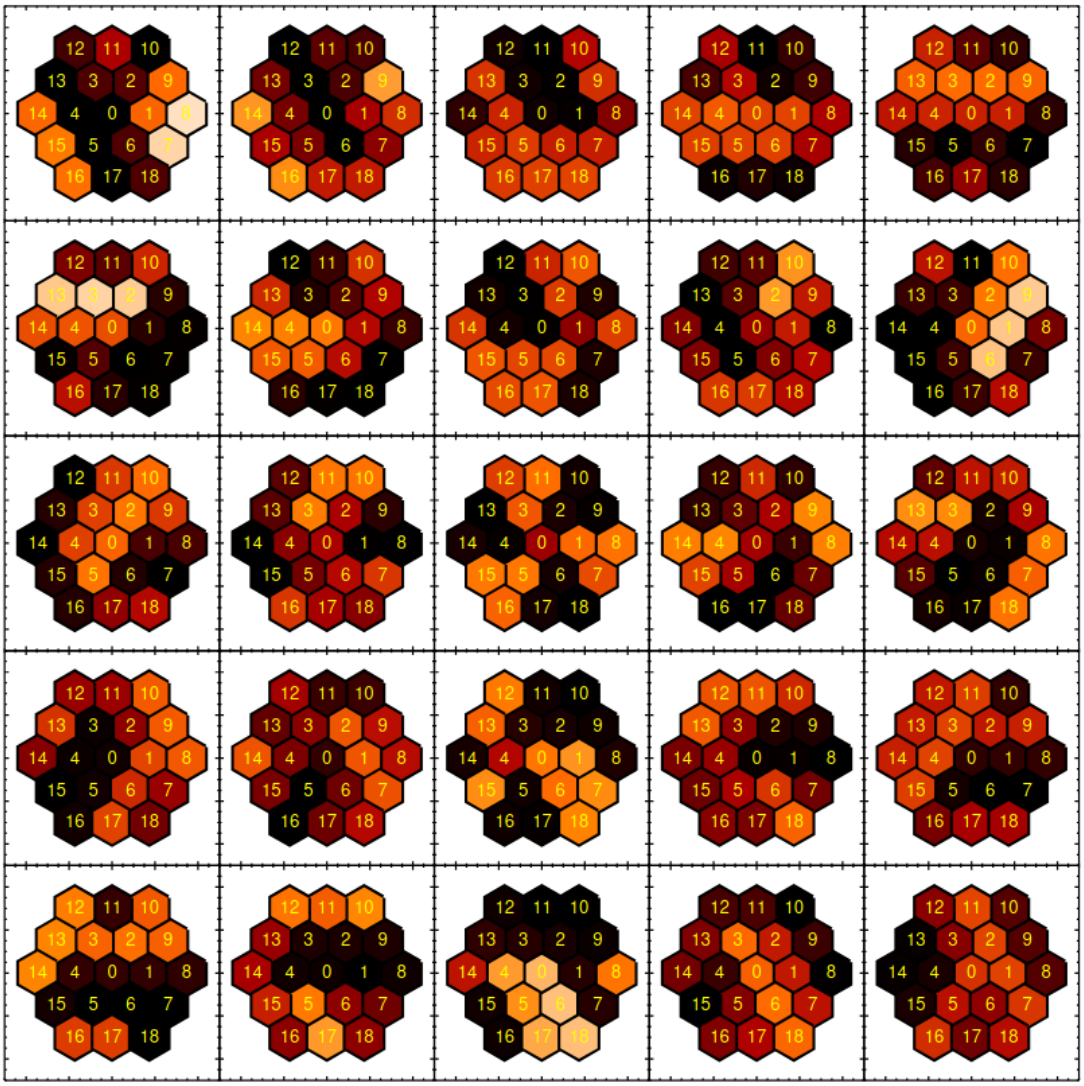

Fig. 20: Shadowgrams of the 19 Ge detectors for the 5 x 5 grid "dithering" with a point source on axis (target direction). Each shadowgram shows the detector layout with the detector numbers from 0 to 18 and the detector response in color code from black (no signal, totally shadowed) to red, yellow, and white (maximum exposure). Figure taken from Diehl et al. [2018].

3.2.2 Coded Mask

To obtain the information on the direction from where the photons enter the Ge detectors, SPI is equipped with a coded mask (Fig. 19). The resulting distribution of a set of photon events on the Ge detectors is called their shadowgram, due to the mask shadowing some detectors from the source. The information from these shadowgrams is the response function. To better resolve sources, INTEGRAL is also systematically oriented facing a 5×5 grid with 2.1° steps around the target direction. This is called "dithering" and the resulting shadowgrams for a point source on axis are displayed in Fig. 20. Over typically long exposure times, i.e., hundreds to many thousands of pointings, this method leads to a well-defined modulation, giving the position of a celestial source [Diehl et al., 2018]. Since typical gamma-ray sources produce only intensities of $\approx 10^{-5}\,\mathrm{ph\,cm^{-2}\,s^{-1}}$, the individual Ge detectors capture only a few photons during a pointing and the modulation is only reached statistically. The information from the response is then also fundamental in distinguishing between celestial and instrumental-background events, with the latter expected to be constant from pointing to pointing [Diehl et al., 2018].

3.2.3 Dataset

The dataset used in our analysis consists of 20-year SPI observations between 2003 and 2023. This gives us 143360 pointings and 254.7 Ms of total exposure time. The all-sky distribution of the pointings is shown in Fig. 21. Most of the pointings are directed into the Galactic plane. The Orion region is observed with $\sim 1.6 \cdot 10^3$ pointings, adding up to an exposure of ~ 4.6 Ms. We use an energy bin size of 0.5 keV in the range of 1790 – 1840 keV.

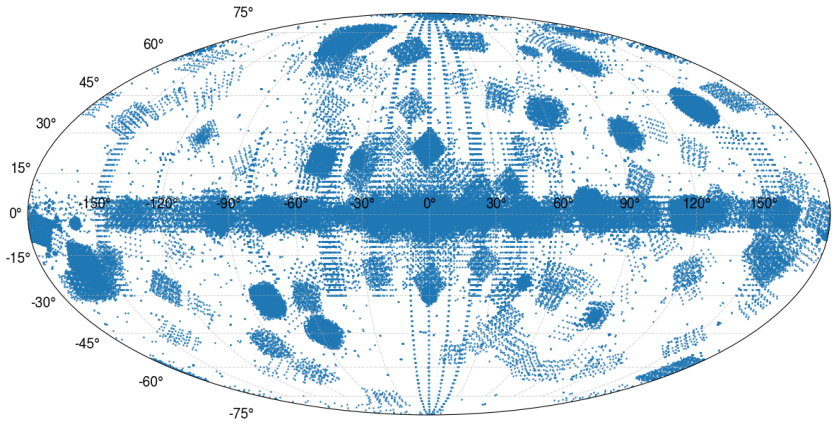

Fig. 21: 143360 pointings between 2003 and 2023 with the total exposure of 254.7 Ms. The Galactic plane is observed most frequently. The Orion region is observed $\sim 1.6 \cdot 10^3$ times, with an exposure of ~ 4.6 Ms.

The data accumulated for these pointings is shown in Fig. 22, for each detector, counting all the photons in the energy range. The counts measured by each detector correlate for the different pointings, i.e., high flux in an observation shows higher counts in all the detectors. The figure also shows when detectors fail and cannot contribute to the measurement anymore. This was the case for detectors 2, 3, 6, and 18. Here, the background must be re-calibrated. To examine the background contribution in the data, we compare

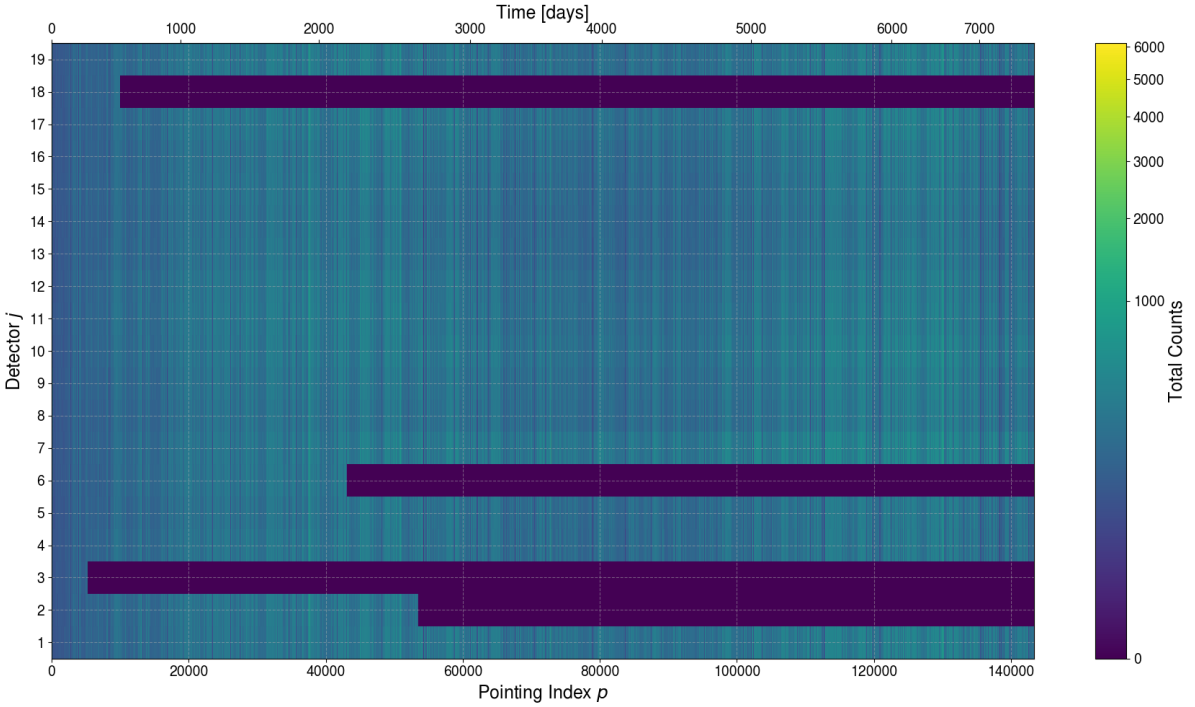

Fig. 22: Measured counts in all 19 detectors for each pointing in our dataset. Detectors 2, 3, 6, and 18 all fail at some point during the mission.

the measurement of the Galactic plane (in the sample of all pointings for $(-60° \leq \ell \leq 60°$, and $-5° \leq b \leq 5°)$, where we expect a strong signal, with the measurement of high latitudes in all poinitngs with $|b| > 60°$, where we expect no signal and only background contributions. To compare the two regions with different numbers of pointings, we normalise the observation to the exposure time. The resulting spectra for the Galactic plane and the background, for the 100 energy bins, is shown at the top of Fig. 23. The figure shows that the observation with SPI is dominated by the background contribution. The gamma-ray line emission at 1.809 MeV from the Galaxy is not visible without cleaning the measurement from the background. The result when removing the background component is shown at the bottom of Fig. 23. Here, the signal from the Galaxy becomes visible on top of a baseline from the different background amplitudes in the observations. The negative baseline means that the activity in the instrument material was stronger for the observation of the high latitude background contribution.

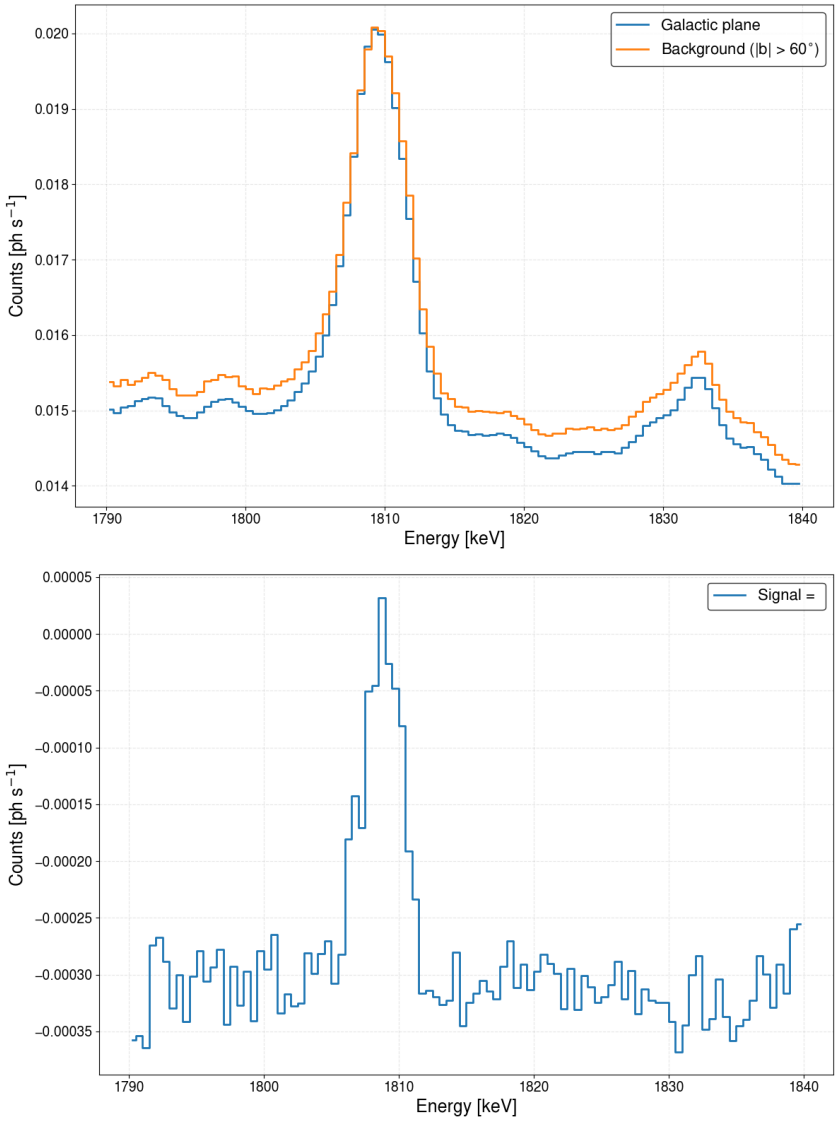

Fig. 23: Observation in the Galactic plane compared to the background. Top: Spectra for both measurements, with only Galactic plane contributing pointings ($-60° \leq \ell \leq 60°$, and $-5° \leq b \leq 5°$) and background pointings ($|b| > 60°$). Bottom: Difference between the Galactic plane and the background show a signal in the form of a gamma-ray line at 1.809 MeV.

3.2.4 Instrumental Background

Energetic particles cause this dominant instrumental background in the Ge detectors. The resulting spectra, show the background as superimposed nuclear lines on a continuum falling towards high energies (Fig. 24, left). When these energetic particles collide with the satellite, different emission processes follow, leading to imminent or delayed events in the detectors (Fig. 24, right). Prompt emission results from Bremsstrahlung and nuclear excitation lines, while cosmic-rays also produce secondary protons. The continuum is dominated by Bremsstrahlung of these secondary protons, while the lines result from nuclear de-excitation. In our analysis, we follow an entirely empircial background modelling

approach. This accounts for the unpredictability of the cosmic-ray spectrum at SPI's energy domain and position [Diehl et al., 2018]. As mentioned, the data can be modelled

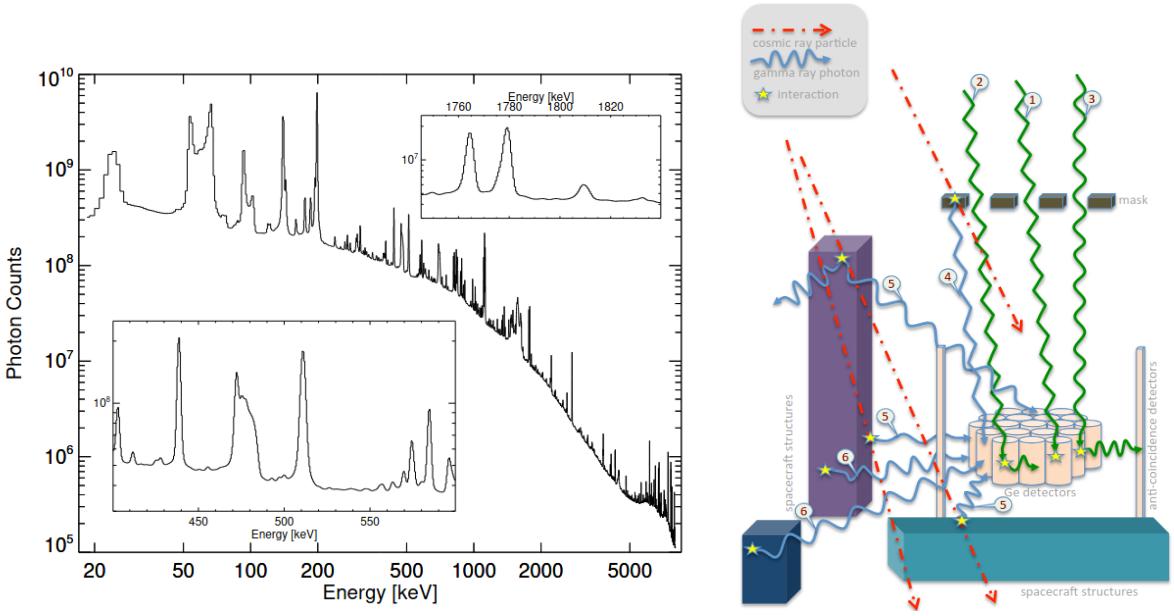

Fig. 24: Left: All detector energy spectrum measured with SPI integrated over the orbits 43-1730. The background follows a continuum superimposed with nuclear de-excitation lines. The inserts show in detail the two brightest celestial lines at 511 keV and the aforementioned 1.809 MeV.
Right: Different events possible in the SPI Ge detectors. In green, cosmic photons that produce single events (1), multiple events (2), and self-vetoed events (3). In blue, background photons arise from the scattering of cosmic-rays (red) promptly (4,5) or delayed via radioactive decay (6). Figures taken from Diehl et al. [2018].

with the combination of the sky and background models (Eq. 29), which is optimised for the amplitudes with a maximum-likelihood fit. The used background models are based on what is already known about the sky and instrumental background, and improves over the course of the mission. SPI's background modelling is therefore based on two assumptions. First, celestial sources produce shadowgrams that conduct the contribution of each detector to the source signal. Second, the instrumental background does not vary during small re-pointings, leaving a characteristic signal shape and relative detector ratios [Diehl et al., 2018].

3.2.5 Background Optimisation

The background modelling, i.e., evaluating the spectrum of the instrument when observing no source, is dependent on the activity at SPI's position at any given time. To account for variability, the background is modelled often over the time of the mission on a chosen timescale. This timescale tunes the background modelling and controls the number of background parameters. The best background model is given for an optimised timescale

and thus the optimal number of background parameters. The quality of a setup is then classified via the Akaike Information Criterion [AIC Akaike, 1974]:

$$\mathrm{AIC} = 2N_{\mathrm{par}} - 2\ln \mathcal{L}(D|M) \tag{30}$$

Therefore the likelihood $\mathcal{L}(D|M)$ of the data D, being a realisation of the model, M, with N_{par} background parameters is penalised by this number N_{par}. By evaluating relative ΔAIC (absolute AIC differences), we determine the appropriate timescale on which the background must be re-adjusted [Siegert et al., 2019]. We can evaluate the AIC for each bin (Fig. 25) to find the best background setup for the 100 bins for each sky model, respectively. We use sky models based on two surveys in the following. The COMPTEL

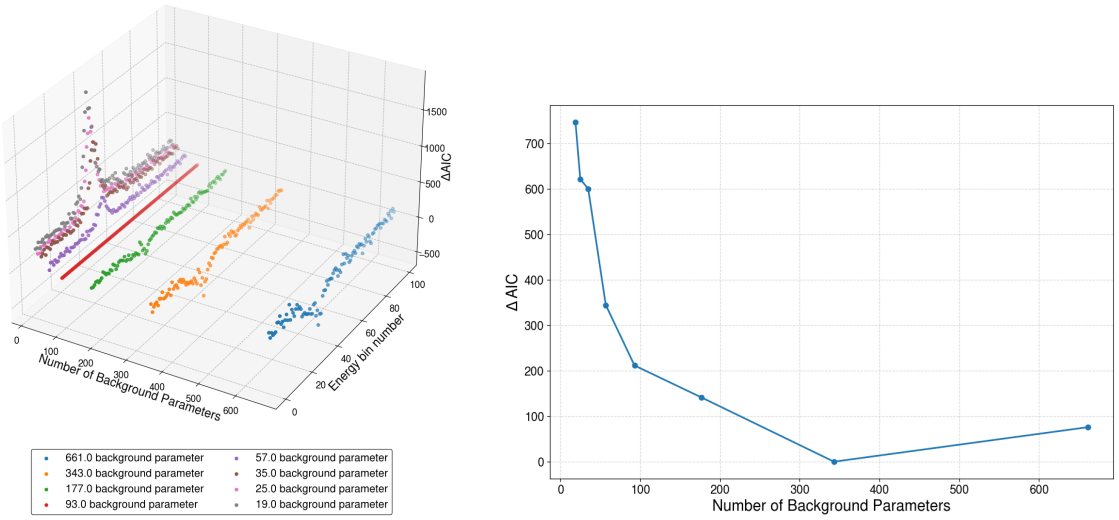

Fig. 25: The relative AIC for varying background for the whole spectrum of Orion with the SPI survey (left) and for the energy bin 30, centered at 1804.75 keV, as an example of the ΔAIC optimisation (right). For this energy bin and this survey, the background needs to be modelled with 343 background parameters, i.e., every 16th revolution.

all-sky map, from Plüschke et al. [2001], and the SPI all-sky map from Bouchet et al. [2015], both at 1.809 MeV. We get two background setups for each region described with both surveys. This is given in template maps for each. The template maps hold the optimised number of background parameters for each survey, region, and energy bin. We calculate the template maps for a reference model, in the Cygnus region, and for our region of interest, Orion, for both surveys. The results are displayed in Fig. 26, with the exception of the Orion sky model based on COMPTEL. For Orion, both surveys led to the same background configuration and identical template maps. In the following analysis, the background is optimised according to the respective template map.

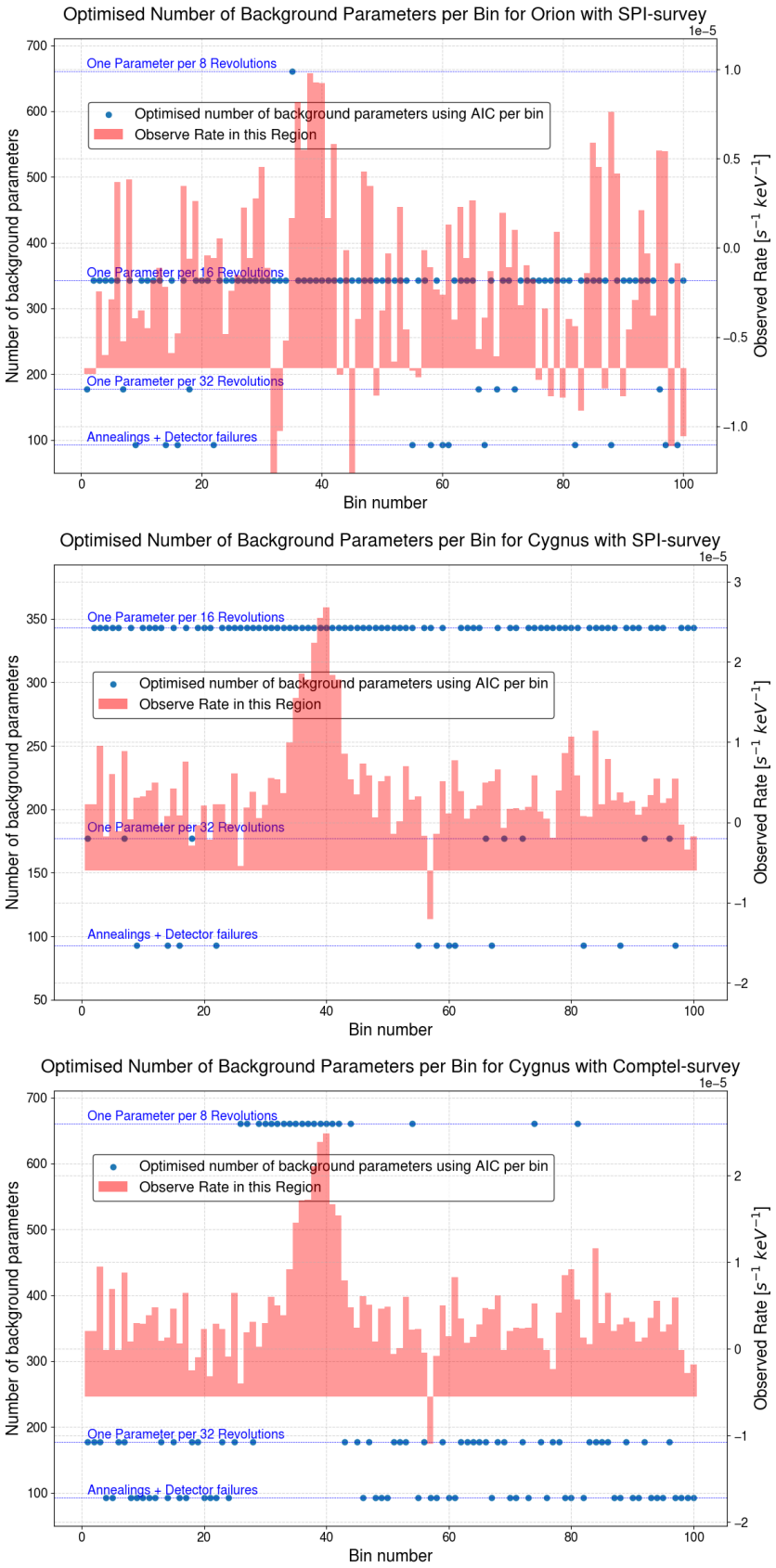

Fig. 26: Template maps for the sky models created with two surveys, SPI and COMPTEL, for the regions Orion and Cygnus show that the best number of background parameters is not constant for the bins and respective sky models. For the Orion region, the template map is identical with both surveys, and we do not show Orion-COMPTEL here. These templates will be used for the AIC optimised spectroscopy in the next step.

3.2.6 Sky Model Optimisation

The second part of our model setup (Eq. 29), the sky models describe the flux expectation of the source that is examined. Thus, the sky image is seen in the camera of SPI through the shadowing of the coded-mask. The response of the coded-mask needs to be applied to the sky model. This is done in the convolution of the sky image with the response matrix, i.e., the spectral and spatial response of SPI. For the size of our dataset and over the whole range of 1790–1840 keV, this convolution is very time-consuming. Here, we introduce a method to fasten this step in the spectral analysis using properties of the spectral response. The spectral response is shown in Fig. 27. The left panel shows the probability density of

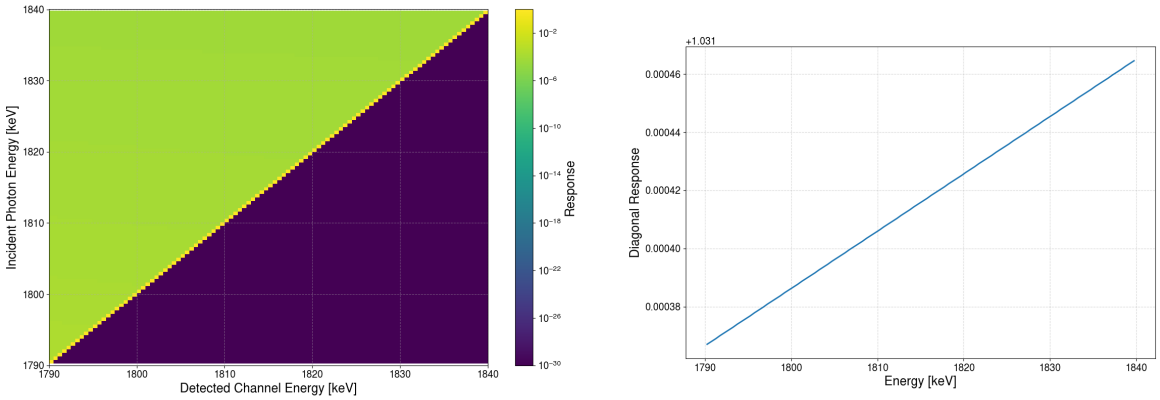

Fig. 27: Spectral response of the instrument. Probability density for an incident photon to be registered in an energy bin (Left). Peak response value on the diagonal (Right). The spectral response shows the high spectral resolution of SPI.

an incident photon being detected in one of the 100 channels. The pronounced diagonal shows the high resolution of the instrument, i.e., photons are detected, and registered with the energies they carry. The right panel shows how the probability density develops along the diagonal. Since the response of each channel follows the same function and changes approximately linearly along the diagonal, we can estimate the spectral response of each energy bin by the spectral response of bin 50. We thus only need to convolve this energy bin with the sky model. The result of this convolution is then used as input for the rest of the energy bins 1 – 100. We call this method speed convolution. When comparing the speed with the conventional convolution, we find a deviation in the resulting spectra, with line fluxes from the Cygnus and Orion region. We quantify this deviation Δ according to

$$\Delta = \frac{F_{\text{Speed}} - F_{\text{Conventional}}}{F_{\text{Conventional}}} \tag{31}$$

, and show it in Tab. 7. We test two sky models in the Cygnus region, that will be used to validate the method later on and one sky model in the Orion region to confirm the same sky model response to the speed convolution method. The spectra for Orion with a SPI-based sky model convolved in both ways are shown in Fig. 28. Here, slight deviations

in the spectra arise. The fit parameters of the 1.809 MeV gamma-ray line are consistent within statistical uncertainties in both spectra.

Sky Model	$F_{conventional}$ $[10^{-5}\,ph\,cm^{-2}\,s^{-1}]$	F_{speed} $[10^{-5}\,ph\,cm^{-2}\,s^{-1}]$	Deviation
$Orion_{SPI}$	(3.50 ± 0.82)	(3.43 ± 0.77)	$(2 \pm 32)\%$
$Cygnus_{SPI}$	(8.36 ± 0.87)	(8.40 ± 0.87)	$(1 \pm 15)\%$
$Cygnus_{COMPTEL}$	(7.54 ± 0.79)	(7.59 ± 0.79)	$(1 \pm 15)\%$

Tab. 7: Flux values for Cygnus and Orion with both convolution methods, from the spectral analysis in the range 1790 – 1840 keV. The systematic error from the deviation is negligible considering its statistical uncertainty. The sky models are based on the survey given in the subscript, SPI or COMPTEL.

It is important to have these systematics in mind but when we compare them with the statistical uncertainties, we conclude that they are negligible in our further analysis. All the following spectra are done with the speed convolution method.

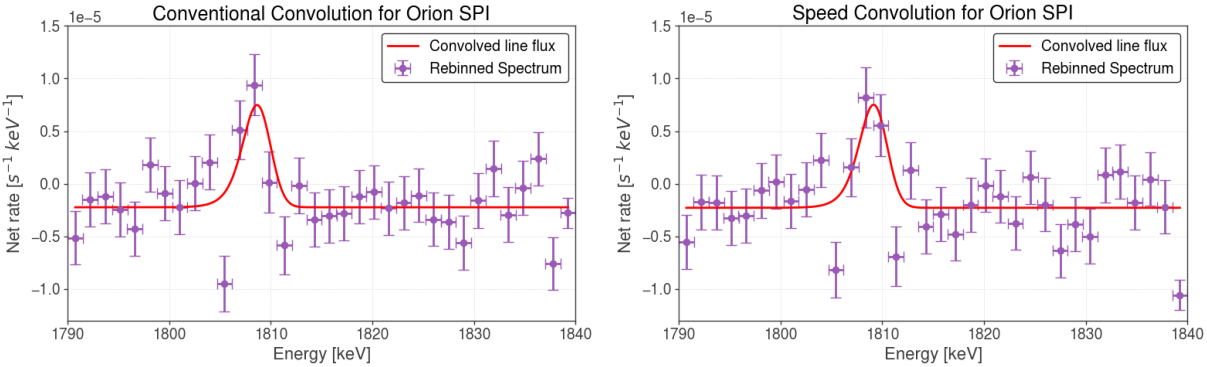

Fig. 28: Spectra for Orion, with a sky model based on the SPI survey from Bouchet et al. [2015]. The left spectral analysis was done with the conventional convolution. The right spectral analysis was done with the speed convolution. The spectra lead to the same 1.809 MeV line fit, with the fit parameters matching within their uncertainties, even though the spectra show slight deviations.

3.3 Test Statistics

Before modelling the ^{26}Al sky in the Orion region, we test the statistics for this region in our dataset. We use a set of initial models in a three-dimensional parameter space to describe the Orion region in respective sky models. The parameters we test are the position in longitude ℓ_0 and latitude b_0 as well as the width of the source model. These initial models are realised with the [von Mises–Fisher distribution in `astromodels`; Vianello et al., 2015], i.e., a two-dimensional Gaussian on a sphere, in spherical coordinates:

$$\begin{aligned} M_{\text{intial}}(\ell, b, \sigma_{2D}) &= \exp\left(-\frac{\theta^2}{2\sigma_{2D}^2}\right) \\ \theta(\ell, b, \ell_0, b_0) &= \arccos\left[\sin(b)\sin(b_0) + \cos(b)\cos(b_0)\cos(\ell - \ell_0)\right] \end{aligned} \tag{32}$$

, with the angular distance on the sphere θ. We vary the width starting from σ_{2D} is 0° (point source) to 8°, and limit the model extension to a region of $3\sigma_{2D}$ to avoid low-flux values that could introduce noise in the fitting process. To account for the gamma-ray emission from all regions except Orion, and to provide a reference against which the tested models can be evaluated, we use the all-sky image from COMPTEL, excluding the region with longitudes $\ell = 140° - 180°$ and latitudes $b = -60° - (-6°)$. The COMPTEL image with the test region is shown in Fig. 29, with an exemplary initial model placed at $(\ell, b) = (164°, -22°)$ with the width of 5°. The models are placed in a grid that covers the entire test region. We place models for the set of widths, with one model per pixel in the grid. The grid consists of pixels with a constant pixel area of $3.4\,\mathrm{deg}^2$. Thus, models with the same width cover the same area in the sky, regardless of their latitude position. Leaving the test region empty (Fig. 29) defines the baseline model with likelihood $\mathcal{L}_0$. How to evaluate each tested model with the likelihood $\mathcal{L}_1$ is given in Eq. 33.

$$\begin{aligned} \Delta \ln \mathcal{L} &= \ln \mathcal{L}_0 - \ln \mathcal{L}_1 \,, \\ TS &= -2\,\Delta \ln \mathcal{L} \,. \end{aligned} \tag{33}$$

With TS, the model improvement, we get the information on the probability of our models at the respective position. When displaying this improvement on the grid where

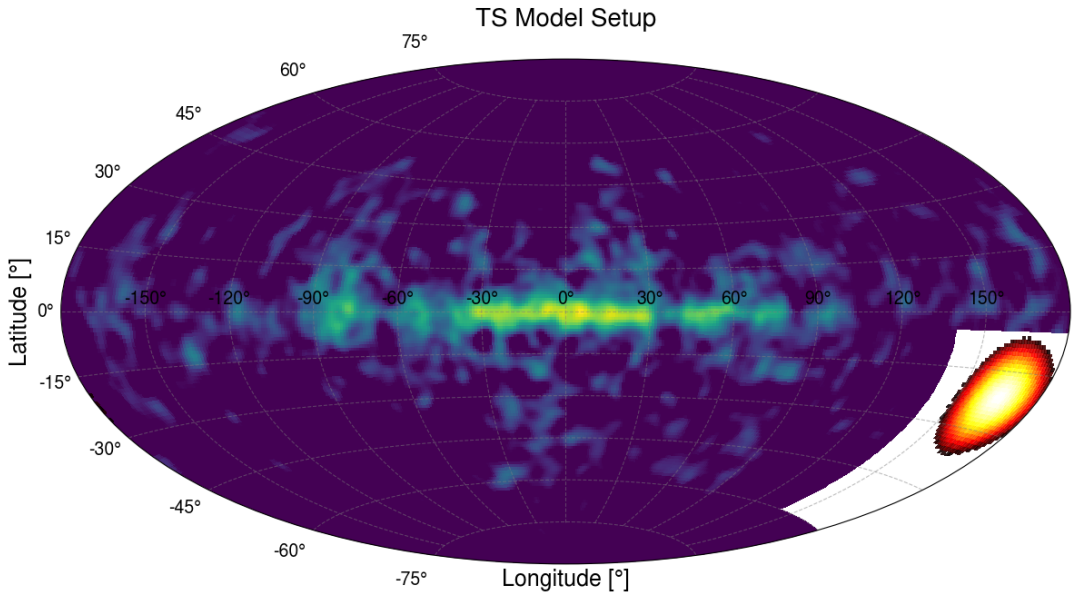

Fig. 29: Exemplary illustration of the sky model setup for the test models. The COMPTEL map with the test region cut out (blue – green) represents the baseline model, while a 2-D Gaussian with a width of 5σ, centered at $(\ell, b) = (164°, -22°)$ (red – white), fills the test region.

we distributed the initial test models, we get so-called "TS maps" (test statistics), which are shown in Fig. 30, in addition to the respective line flux results for each model. The more likely point source models seem to be scattered around the expected position of the OES. Therefore, we need mildly extended models to model the OES. This is substantiated when we take the flux for these point source models into account. Here, we find only positive flux results in the outer parts of the test region. This changes for the extended models. All the extended models produce positive flux values in the central tested region. The most likely models are the extended models with width between $\sigma_{2D} = 2^\circ - 5^\circ$. Also, the extended models converge in their likelihood into a hotspot at $(\ell, b) = (166^\circ, -23^\circ)$. This shows a shift to the COMPTEL image hotspot, indicating a difference in the ^{26}Al distribution in the test region measured with SPI. Additionally, we find a "hotter" region in the model line flux profile at lower latitudes. This could confirm an outflow of the ^{26}Al into the OES, and thus ^{26}Al yields in the region towards the Eridanus end. This will also be tested when modelling the ^{26}Al sky in Sec. 4. The extended flux detection matches the diffuse emission from the Orion region measured by COMPTEL. Thus, we find confirmation of extended source emission from this region, in our dataset. The TS maps also show boundaries for the ^{26}Al distribution, constraining the 1.809 MeV line flux to latitudes above $\sim$ (-40°). This would mean that the ^{26}Al does not reach the far end of the OES, which lies at lower latitudes.

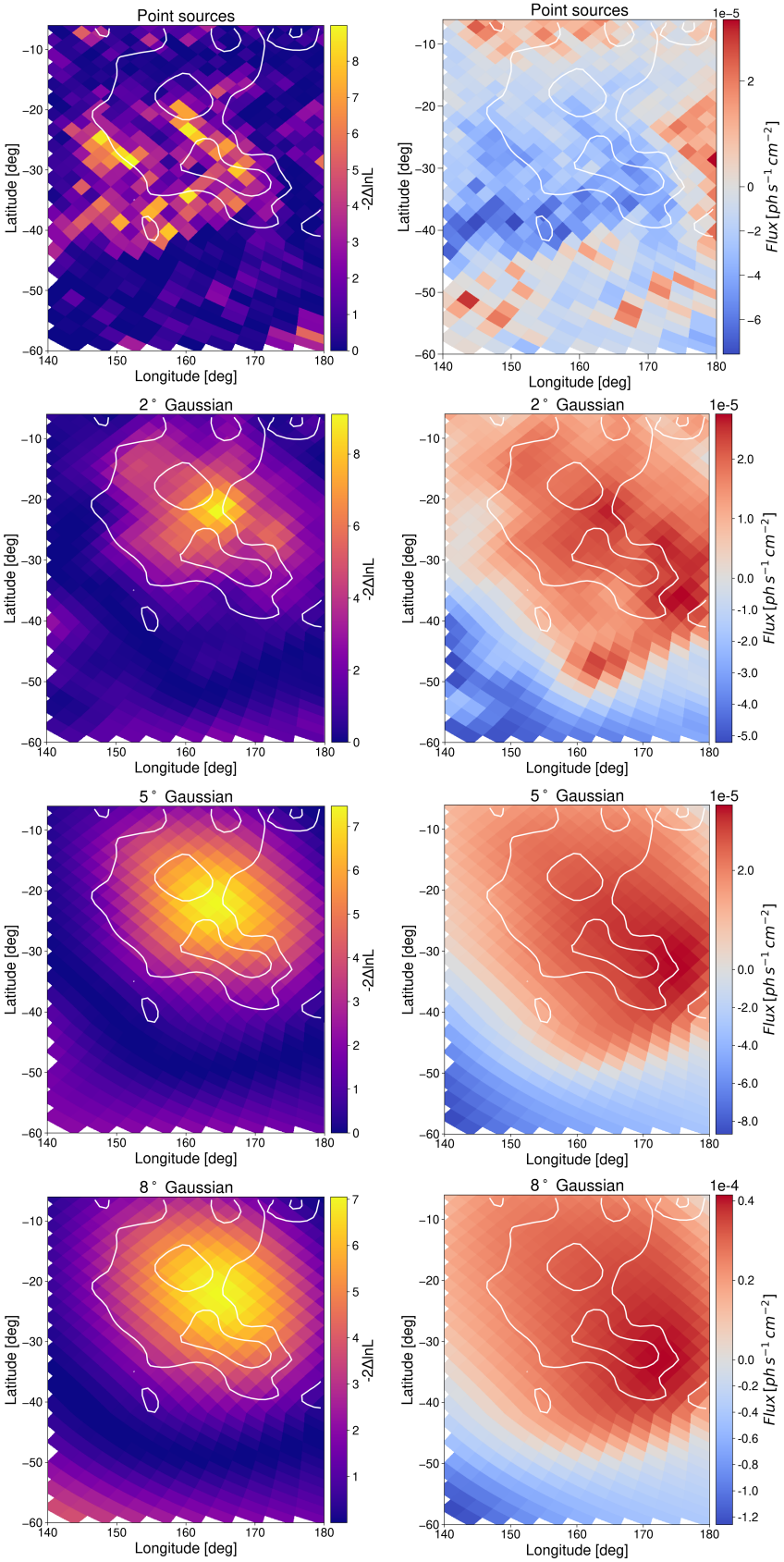

Fig. 30: Left: Test-statistic maps for different widths of the 2D Gaussian models (top to bottom 0°, 2°, 5°, and 8°). The COMPTEL image is overlaid as white contours. We notice an offset between the COMPTEL hotspot and the center of the most likely models. Right: Line-flux values for varying widths of the 2D Gaussian models. The OES is hardly identifiable with point-source models, requiring instead mildly extended sources. We note that in both cases, these are not images but 2D likelihood profiles and flux estimates for individually tested components at fixed positions.

4 Modelling the ^{26}Al Sky

In this chapter, we model the ^{26}Al signature of the Orion region. We use two different approaches. First, we extract sky models from the two mentioned surveys at 1.809 MeV (Plüschke et al. [2001], and Bouchet et al. [2015]), for Orion, and to validate the method for Cygnus and the MW. Second, we construct a physical model based on the geometry for the OES, with an ^{26}Al-mass estimation of the Orion OB1 association in Sec. 4.2.

4.1 Empirical Sky Models

To produce spectra for our regions of interest, we need to create respective sky models. One approach is to use empirical sky models. These are based on measurements of the sky at 1.809 MeV. We use the observation from COMPTEL, Plüschke et al. [2001], and from SPI, Bouchet et al. [2015]. The two all-sky 1.809 MeV surveys are shown in Fig. 31. The differences in the two images arise from the different instruments used. COMPTEL is a Compton telescope, unlike SPI, which is a coded-mask telescope. The image reconstruction for the two instruments, therefore varies for the two measurements. For SPI, the image reconstruction leads to some high latitude flux, where no 1.809 MeV emission is expected. This is considered an artifact of image reconstruction.

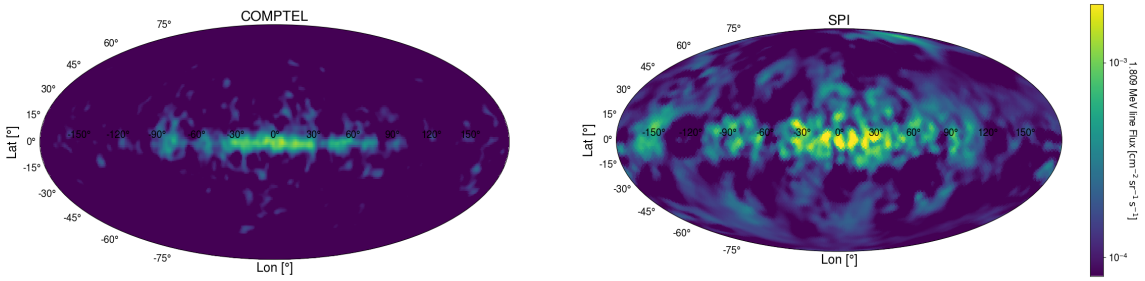

Fig. 31: 1.809 MeV whole sky surveys from COMPTEL, Plüschke et al. [2001] (left) and SPI, Bouchet et al. [2015] (right). Although both instruments measured the same sky, the images differ. This is due to COMPTEL being a Compton telescope and not a coded-mask instrument like SPI. The image reconstruction for the two designs works differently, leading to a grainier and less smooth appearance of the SPI results than those of COMPTEL.

In order to study a specific region in the sky that is incorporated as a result of these image reconstructions, we split the all-sky maps into two regions. One of them describes the region of interest with the remaining Galaxy masked out, and the other describes the remaining Galaxy. The amplitude of the two components is then independently fitted. Thus, the sum of both components is not necessarily the same result as the image reconstruction fitted as one. For the Orion and the Cygnus region, the cut-outs, i.e., the part from the image we use to describe either region and the negative image, i.e., the rest of the Galaxy, are shown in Fig. 32. We use circular cutouts with a radius of 15° for each region, as used in previous analysis by Siegert [2017]. We analyse the impact of different cut-out sizes in Sec. 4.1.2.

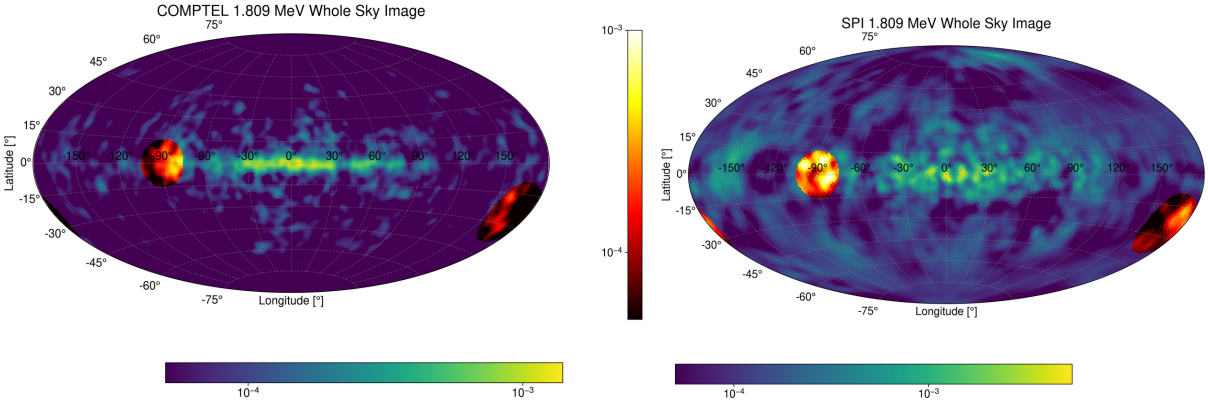

Fig. 32: Sky models cuttet out of the 1.809 MeV whole sky surveys from COMPTEL, Plüschke et al. [2001] (left) and SPI, Bouchet et al. [2015] (right). The Cygnus (at $(-90°, 0°)$) and the Orion region (at $(168°, -24°)$) are placed, where they were cut out. All colourbars show the flux intensity in units of $\mathrm{cm}^{-2}\,\mathrm{sr}^{-1}\,\mathrm{s}^{-1}$.

4.1.1 Cygnus

To validate our measurement method, we start with the observation of the Cygnus region. This region was significantly detected in previous analysis, which makes it suitable for testing the method. The spectral analysis results for Cygnus from Wang [2013] and Siegert [2017], are shown in Tab. 8. In our spectral analysis, we use the background setup

Cygnus previous analysis				
	Flux $[10^{-5}\,\mathrm{ph\,cm^{-2}\,s^{-1}}]$	$\mathrm{FWHM_{Sky}}$ [keV]	Centroid Shift [keV]	Significance $[\sigma]$
Wang [2013]	6.0 ± 1.0	3.10 ± 0.67	...	6
Siegert [2017]	9.28 ± 1.75	3.66 ± 0.46	0.00 ± 0.19	10.9

Tab. 8: 1.809 MeV gamma-ray line flux results for the Cygnus region in previous analysis.

and the sky models for the two surveys, COMPTEL and SPI, respectively. The fitting is a likelihood method using OSA/`spimodfit`. [Courvoisier et al., 2003]. Models, which are made of a degraded Gaussian, i.e., a Gaussian convolved with an exponential tail, on top

of a constant, are fitted to spectral data points. The degradation of the Gaussian is how a symmetrical gamma-ray line is seen through the spectral response, and is quantized with the degradation parameter τ. For the analysis of the 1.809 MeV line, this parameter is fixed at $\tau = 1.05$ keV. The data points have Gaussian uncertainties, and we minimize χ^2 when fitting. The models then represent the gamma-ray spectrum in this energy range for our studied regions. We optimize four parameters: the flux, line width, and centroid, along with the continuum offset. The significance of the line flux is then assessed both from its associated uncertainty and through a likelihood ratio test. For Cygnus, this gives:

Cygnus Results						
Sky Model	Flux $[10^{-5}\,\mathrm{ph\,cm^{-2}\,s^{-1}}]$	$\mathrm{FWHM_{Sky}}$ [keV]	Centroid Shift [keV]	$\mathrm{v_{Doppler}}$ $[\mathrm{km\,s^{-1}}]$	sNr	Significance $[\sigma]$
COMPTEL	9.2 ± 1.0	3.0 ± 0.6	0.08 ± 0.23	13 ± 38	8.6	9.1
SPI	8.4 ± 1.0	1.1 ± 0.4	0.60 ± 0.24	99 ± 40	11.4	8.1

Tab. 9: Results for the likelihood fitting of the Cygnus sky models based on COMPTEL and SPI. We calculate the full width half maximum (FWHM) as well as the centroid shift of the 1.809 MeV line ($\Delta\mathrm{E} = E_{\mathrm{SKY}} - E_0$). The centroid position of the celestial line is directly related to the centroid of the degraded Gaussian μ with the degradation parameter (roughly $\mu - \tau$). For the centroid shift, we use the laboratory energy of $E_0 = 1808.65$ keV. The signal-to-noise ratio (sNr) is the line flux in contrast to the constant and the measured FWHM. The velocity of the source towards the Sun is the Doppler velocity $\mathrm{v_{Doppler}}$ corresponding to the centroid shift.

Both sky models produce spectra for the Cygnus region shown in Fig. 33. The line fluxes

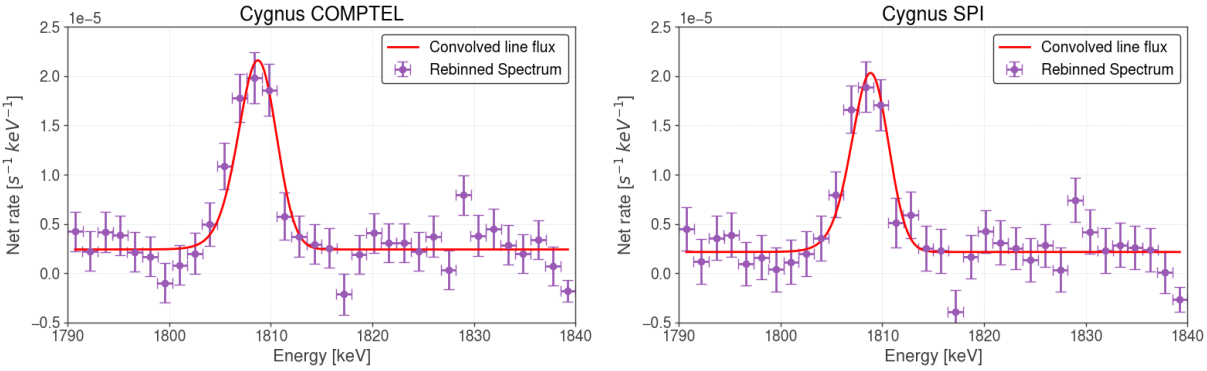

Fig. 33: Observed (purple crosses) gamma-ray spectra of the Cygnus region for the two survey-based sky models. The spectra are fitted in the range of 1790-1840 keV with an asymmetric Gaussian line on top of a constant continuum. For better illustration, we rebinned the spectra a to 1.5 keV bin size. The fit results are summarised in Tab. 9.

in both match the previous measurement from Siegert [2017]. The SPI-based model shows a smaller celestial line than the COMPTEL-based model. In addition, the COMPTEL-based model shows a smaller centroid shift with regard to the lab energy than the SPI-based model. The COMPTEL-model agrees with the expectation for a shift, due to the Galactic rotational velocity with respect to the Sun, that is ~ 0 [Diehl et al., 2006]. The SPI-model leads to a blueshift in the line, which means an additional movement of the

source towards the Sun. This could be an ^{26}Al outflow into the ISM in Cygnus, similar to the one expected for the ^{26}Al inside the OES. We validate our method in deriving spectra for regions of interest, with the spectral analysis being consistent with the previous results.

4.1.2 Orion

With the validation of the method, we can focus on the Orion region. We again use the respective background optimisation for the two survey-based sky models we extracted for the Orion region. The likelihood fitting results in the two spectra, displayed in Fig. 34. The fit results for the 1.809 MeV gamma-ray line in this region are:

Orion Results						
Sky Model	Flux $[10^{-5}\,\mathrm{ph\,cm^{-2}\,s^{-1}}]$	$\mathrm{FWHM_{Sky}}$ [keV]	Centroid Shift [keV]	$\mathrm{v_{Doppler}}$ $[\mathrm{km\,s^{-1}}]$	sNr	Significance $[\sigma]$
COMPTEL	3.0 ± 0.8	$\lesssim 2.9$ (2σ U.L.)	0.40 ± 0.37	66 ± 61	-12.7	4.0
SPI	4.2 ± 1.0	$\lesssim 2.9$ (2σ U.L.)	0.55 ± 0.34	91 ± 56	-12.4	4.7

Tab. 10: Results for the likelihood fitting of the Orion sky models based on COMPTEL and SPI. The parameters that are not directly fitted are calculated in the same way we did for Cygnus (see Tab. 9).

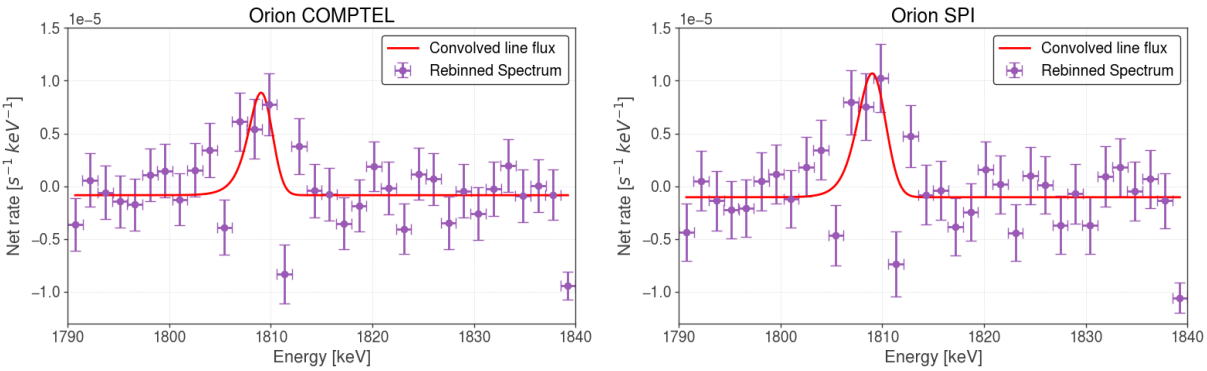

Fig. 34: Observed (purple crosses) gamma-ray spectra of the Orion region for the two survey-based sky models. The spectra are fitted in the range of 1790-1840 keV with an asymmetric Gaussian line on top of a constant continuum. For better illustration, we rebinned the spectra to a 1.5 keV bin size. The fit results are summarised in Tab. 10.

The gamma-ray line flux in Orion for both sky models matches the measurement in Siegert [2017] within their uncertainties ($F_{\mathrm{Orion,(2017)}} = (3.65 \pm 1.19)\,10^{-5}\,\mathrm{ph\,cm^{-2}\,s^{-1}}$). We detect the Orion region in the 1.809 MeV line flux with a detection significance of $4\,\sigma$ for the COMPTEL-based, and $4.7\,\sigma$ for the SPI-based models. The FWHM of the celestial line cannot be determined with the likelihood fit, and we show the 2σ upper limit instead. Both sky models produce a blueshifted line in the spectra. The associated Doppler velocity, for both lines, is positive ranging, from $5-147\,\mathrm{km\,s^{-1}}$ within a one σ-intervall. This could confirm the predominant flow direction of ^{26}Al towards the Eridanus end, which is expected for the OES. When comparing the sky models (Fig. 32), the SPI-based model

shows a shifted hotspot to the COMPTEL-based model. This shift is similar to the hotspot in the TS modelling. This could account for the higher detection significance when using the SPI-based sky model.

Milky Way

When we analyse the sky models for the Orion region, the rest of the Galaxy is fitted as a second component simultaneously. Thus, we produce spectra, shown in Fig. 35, for the MW in addition to the Orion region when combining the two components.

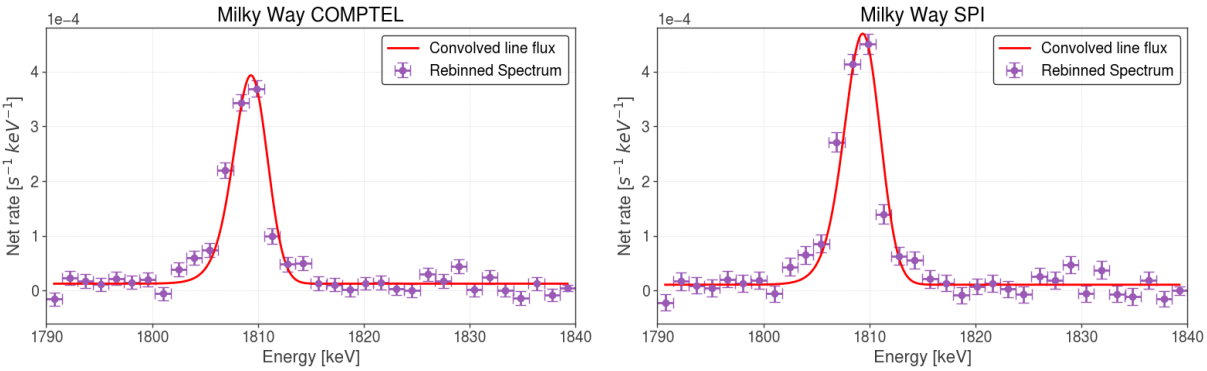

Fig. 35: Observed (purple crosses) gamma-ray spectra of the MW for the two survey-based sky models of Orion as one component and the rest of the Galaxy as the second component. The spectra are fitted in the range of 1790-1840 keV with an asymmetric Gaussian line on top of a constant continuum. For better illustration, we rebinned the spectra to a 1.5 keV bin size. The fit results are summarised in Tab. 11.

The results for the likelihood fitting of the 1.809 MeV gamma-ray line are:

MW Results						
Sky Model	Flux [10^{-5} ph cm^{-2} s^{-1}]	FWHM$_{\mathrm{Sky}}$ [keV]	Centroid Shift [keV]	v_{Doppler} [km s^{-1}]	sNr	Significance [σ]
COMPTEL	157.8 ± 5.6	1.9 ± 0.2	0.69 ± 0.06	114 ± 10	46.3	28.0
SPI	200.2 ± 7.2	2.3 ± 0.2	0.72 ± 0.07	119 ± 12	32.8	27.7

Tab. 11: Results for the likelihood fitting of the MW as composed of the Orion sky models based on COMPTEL and SPI, with the rest of the Galaxy as an additional component. The parameters that are not directly fitted are calculated in the same way we did for Cygnus (see Tab. 9).

The measured 1.809 MeV line flux for the COMPTEL-based sky model, matches with the previous result from Siegert [2017] within the uncertainties ($F_{\mathrm{MW,(2017)}} = (1.69 \pm 0.14)\,10^{-3}\,\mathrm{ph\,cm^{-2}\,s^{-1}}$). The value for the SPI-based model is higher. This is due to the non-zero flux at high latitudes in the SPI image reconstruction. The model prediction of a flux at these latitudes contradicts the observation. While trying to match this area in the model, the rest of the galaxy is upscaled. Thus, the SPI-based sky model fitting overestimates the flux for the MW compared to the previous measurements. We note that the COMPTEL image reconstruction is describing the entire Galaxy better, while

the SPI image reconstruction is more precise when it comes to the Orion region, where the high latitude contribution is not part of the primary sky model.

Bayesian Fitting

The maximum likelihood fitting estimates the resulting parameters without any physical conditioning on the parameters. Thus, when the likelihood is flat, parameters do not converge in the fitting. This is the case for the FHWM in the Orion likelihood analysis. This changes in the Bayesian approach. Here any analysis is weighted with the prior state of information. The Bayesian approach follows Bayes' theorem

$$p(M \mid D, I) = \frac{p(M \mid I)\, p(D \mid M, I)}{p(D \mid I)}, \tag{34}$$

, where M denotes the model, D the observed data, and I the prior information. The term $p(D \mid M, I)$ is the probability of obtaining the data D if the model M and the prior information I are true; this quantity is therefore the likelihood $\mathcal{L}(M)$. The term $p(M \mid I)$ is the prior probability of the model, $p(M \mid D, I)$ is the posterior probability, and $p(D \mid I)$ is a normalisation constant (the Bayesian evidence) that ensures that the posterior is normalised [Gregory, 2005]. We illustrate Bayes' theorem for one parameter θ in Fig. 36. The two panel show two different likelihood functions with a fixed prior on the parameter

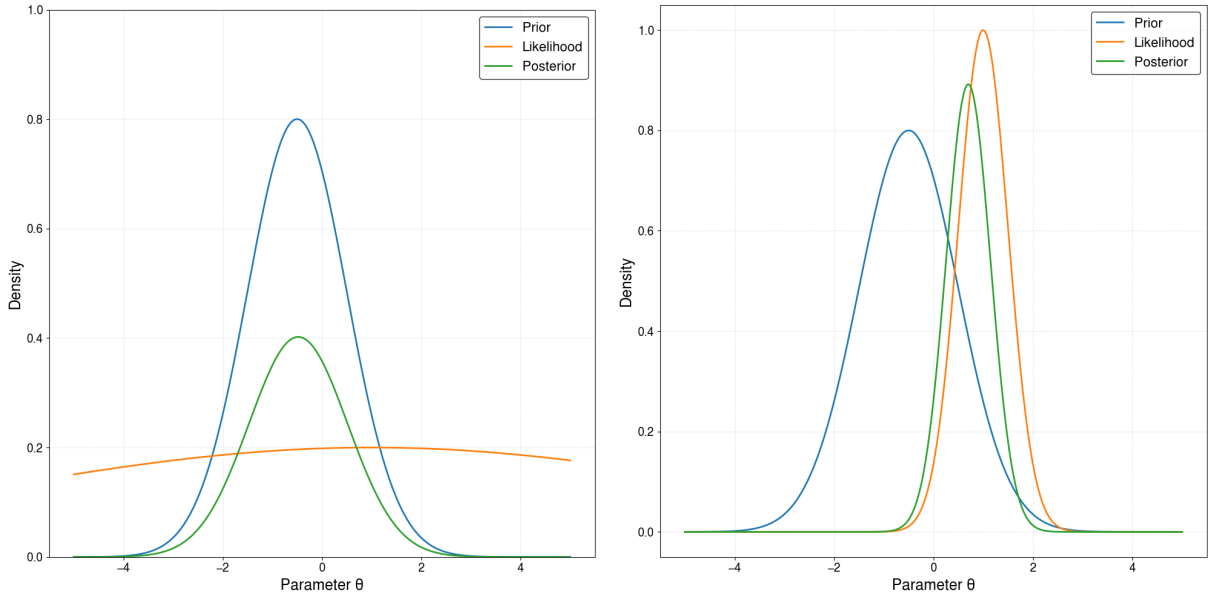

Fig. 36: Two likelihood cases for a given prior resulting in a posterior according to Bayes' theorem.

θ. In the left panel, the likelihood is flat and the posterior is highly dependent on the prior. In the right panel, the likelihood is well defined and dominating the prior. Thus, the posterior is shaped by both the prior and the likelihood. This principle works likewise in a multi-dimensional problem, like our four-dimensional parameter space of, line flux,

line width, centroid, and continuum. Here the prior is defined as a prior volume in the parameterspace, where the parameter priors overlap. A tool that realises the Bayesian approach is the `multinest` algorithm [Feroz et al., 2009]. The underlying technique, nested sampling aims at efficient evaluation of the Bayesian evidence. This is needed to compare probabilities for different models. In this process, the posterior inference is produced as a by-product [Feroz et al., 2009]. Nested sampling works with a fixed set of parameter vectors in the n-dimensional parameter space, sorted by their likelihood. These are the so-called live points. With each iteration, the least likely live point is replaced with a new drawn point, under the condition that the new point needs to have a higher likelihood than the one replaced [Buchner et al., 2014]. The original set of live points is drawn randomly from the prior distribution. During the algorithm, the volume occupied by live points in the parameter space decreases and moves in the direction of a higher likelihood. Projecting this volume after the algorithm ran onto one axis in parameter space gives the posterior for the respective parameter. We use `multinest` to fit the Orion sky model that is based on the SPI survey, with 2000 live points. This is more than sufficient, considering that according to Feroz et al. [2009] a few hundred live points are enough to recover posterior structure. The resulting posteriors are shown in Fig. 37, with profiles showing the priors, in the range of the posteriors. We use for the continuum a Gaussian as prior, centered at $\mu_{\mathrm{K,prior}} = 0$ and with a width of $\sigma_{\mathrm{K,prior}} = 1 \cdot 10^{-6}$. The continuum arises from activity differences at the instrument in the respective background modelling. This is either positive or negative and averages over the mission to be zero. For the line flux, we use a logarithmic uniform prior, $p(F_{\mathrm{Al}}) \propto 1/F_{\mathrm{Al}}$ in the range of $1 \cdot 10^{-7}$ – $1 \cdot 10^{-4}$. The centroid prior distribution is a Gaussian centered at the laboratory energy of 1808.65 keV with width 2 keV. And the prior for the FWHM is a uniform distribution starting at the instrumental resolution with $\sigma_{\mathrm{prior}} = 1.16\,keV - 3.1$ keV. The resulting fit parameters from the Bayesian fit are:

Orion Bayesian Results					
Sky Model	Flux $[10^{-5}\,\mathrm{ph\,cm^{-2}\,s^{-1}}]$	$\mathrm{FWHM_{Sky}}$ [keV]	Centroid Shift [keV]	$\mathrm{v_{Doppler}}$ $[\mathrm{km\,s^{-1}}]$	Significance $[\sigma]$
SPI	$4.42^{+0.48}_{-0.44}$	$1.53^{+0.43}_{-0.59}$	$0.27^{+0.21}_{-0.19}$	45^{+35}_{-31}	9.2

Tab. 12: Results for the Bayesian fitting of the Orion region with the sky models based on the SPI survey. The parameters that are not directly fitted are calculated in the same way we did for Cygnus (see Tab. 9).

The parameters match the likelihood fitting results within the uncertainties (Tab. 10). Additionally, we were able to extract the FWHM of the celestial line, for which we only got upper limits in the likelihood fits. Considering the Bayesian approach and the use of priors, this is expected. Here, posterior distributions are generated for each likelihood function. The FWHM is derived from the measured width of the celestial line; therefore, the prior for the width is not in the converted posteriors in the plot.

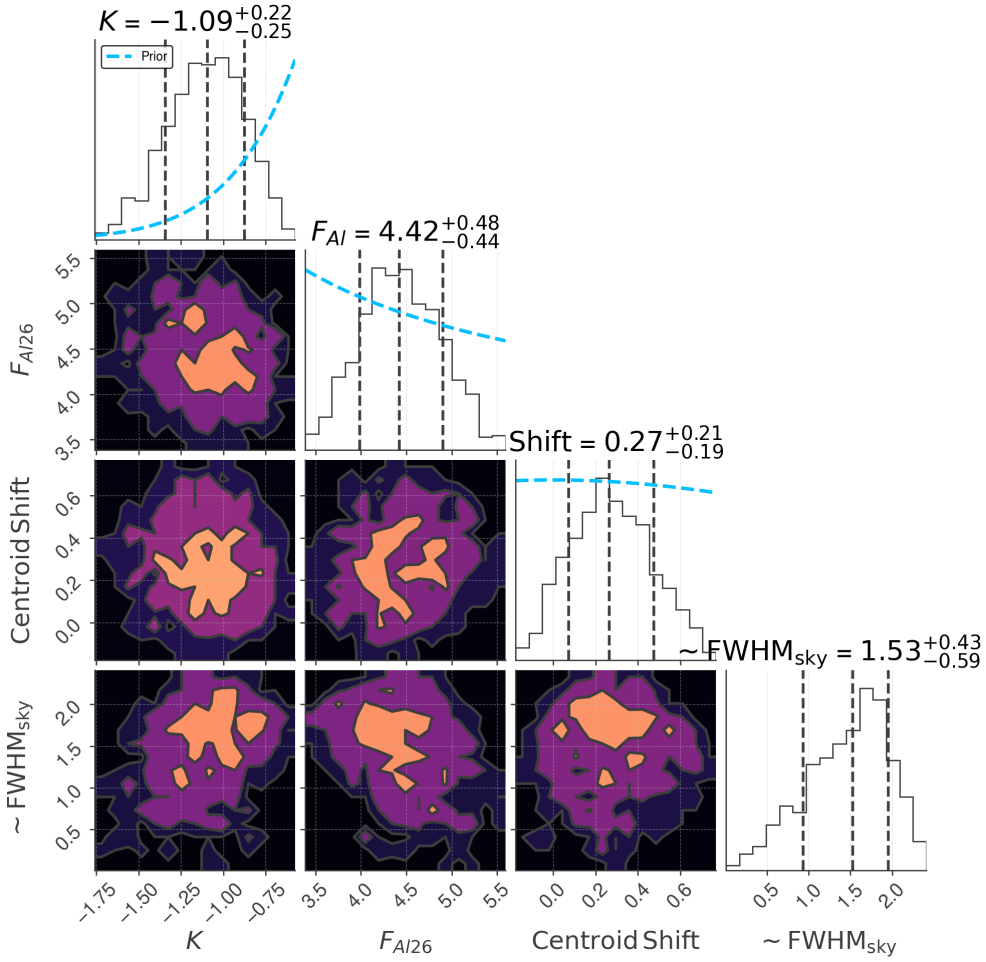

Fig. 37: Bayesian sampled parameters for the Orion 1.809 MeV line flux, using the SPI-based sky model. The blue line indicates the prior distribution for each parameter. The continuum K is in units $10^{-6}\,\mathrm{ph\,cm^{-2}\,s^{-1}\,keV^{-1}}$, the flux F_{Al} is in units of $10^{-5}\,\mathrm{ph\,cm^{-2}\,s^{-1}}$, and the centroid shift as well as the FWHM in units of keV.

Sky Model Size Evaluation

To validate our result for Orion, we need to test different models. Therefore, we test the impact of changing the size of the sky model cut-out, used to describe the Orion region in a sky model. We test a set of sky models centered around the apparent hotspot in the SPI-map of $(\ell, b) = (168°, -24°)$, with varying radii r = $(1 - 40)°$. This set of sky models is then fitted as before in Sec. 4.1.1. The flux and the significance of each model against the expectation for a Galactic disk model (right axis), with the logarithmic likelihood (left axis) are shown in Fig. 38. The Galactic disk is modelled as a double-exponential function following Pleintinger et al. [2019]. They obtained best fit parameters in a scale heigth of z = (0.77 ± 0.17) kpc and a scale radius of z = (5.81 ± 0.64) kpc. To get flux expectations for the Galaxy, we evaluate the flux contribution from the circular region of our respective sky models, which we get from the Galactic disk model. When comparing the Orion model flux to the Galactic background, we not only detect significant gamma-ray emission from

Orion but also a significant difference to the Galactic background model. This confirms the abundance of ^{26}Al in Orion, which we presume to be contained in the OES. To filter out

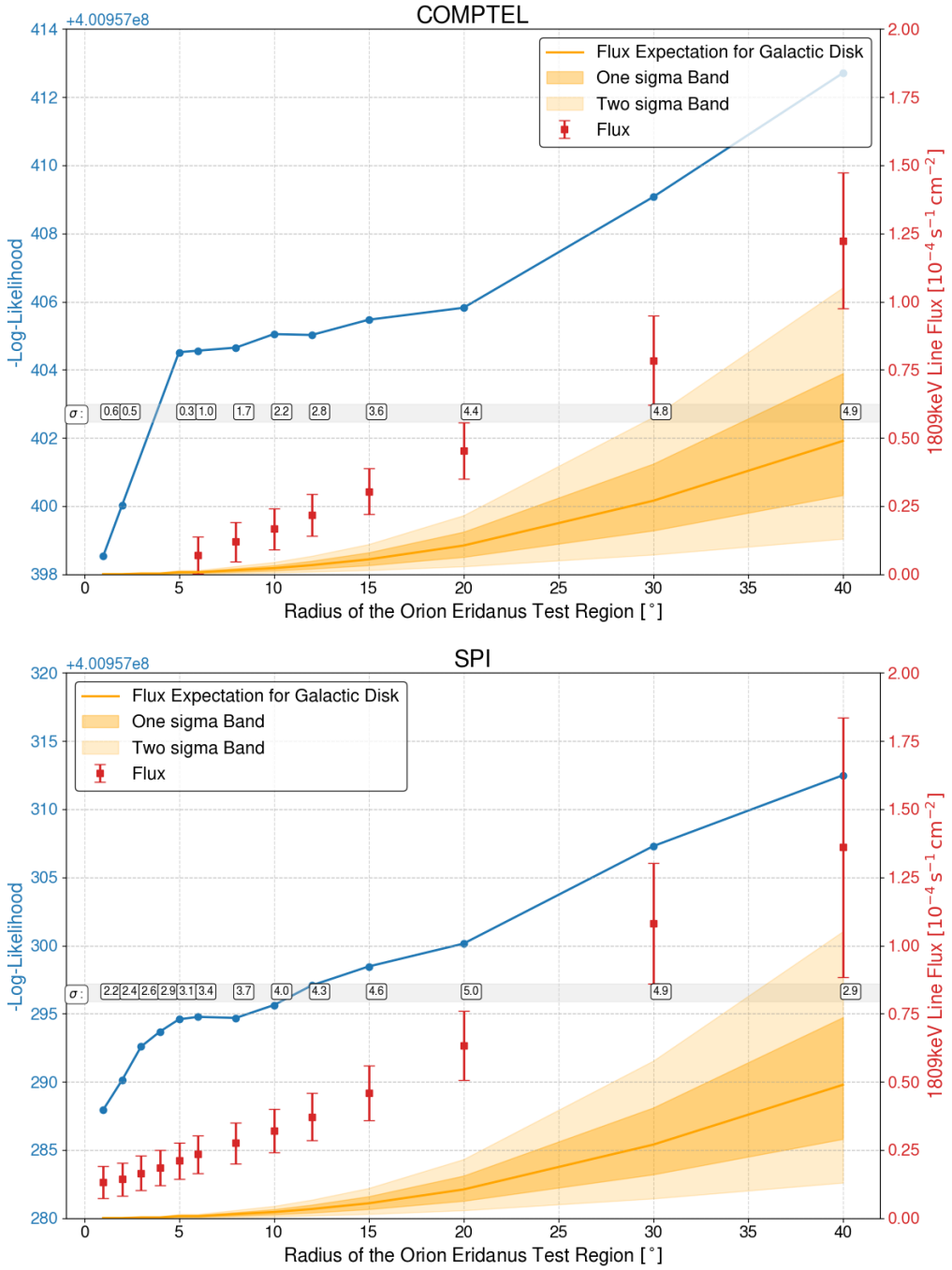

Fig. 38: Likelihood values of differently-sized cutouts (x-axis) from the COMPTEL (top) and the SPI (bottom) map (blue, left y-axes). The 1.809 MeV line flux for each model is extracted (red, right axes) from the fit and plotted against a Galactic background model, estimated from a double-exponential disk with scale height of $z = (0.77 \pm 0.17)$ kpc and scale radius of $z = (5.81 \pm 0.64)$ kpc (orange). The detection significance is added for each model data point.

models that are inferior in describing the region, we use a detection significance threshold of $\geq 4\sigma$. In addition, we exclude sky models with $r > 20°$, since in these sky models large

diffuse flux contributions and hotspots from the Perseus region become part of the sky model (Fig. 12). Thus, the ^{26}Al detection is not meaningful in the description of the Orion sky. For this reason, we exclude these models from the analysis. The resulting set of, as good approved, models are the SPI-based sky models from radii $r = (10 - 20)^\circ$ and the COMPTEL-based sky model with $r = 20^\circ$. For these, we find the total 1.809 MeV line flux in Orion to be in the range of $F_{Orion} = (2.4–7.6) \cdot 10^{-5}\,ph\,cm^{-2}\,s^{-1}$. The 1.809 MeV line flux contribution we consider to be from the OES is consequently the difference between the total line flux and the Galactic expectation. This gives us a 1.809 MeV line flux from the OES in the range of $F_{OES} = (2.2–6.6) \cdot 10^{-5}\,ph\,cm^{-2}\,s^{-1}$. We can estimate the ^{26}Al mass in the OES with Eq. 23. For the distance of $300 - 500$ pc from the Sun to the emitting ^{26}Al inside the OES assuming an average age of 3 Myr we evaluate the ^{26}Al-mass in the OES to be $M_{26} = (1.7 - 5.0) \cdot 10^{-5}\,M_\odot$.

4.2 Physical Models

We concluded before that there is ^{26}Al in the direction of the OES. We want to use this conclusion to build physical models to describe the OES as an extended source, independent of previous image reconstruction. This is done by a geometric model filled with information about the stars in Orion and their ^{26}Al output.

4.2.1 Geometric Setup

In Sec. 2.2.2 we introduced the two possible solutions from Pon et al. [2014], models A and T. The parameters we know from their analysis are not enough to define two unambiguous ellipsoidal models, congruent to the models A and T. Therefore, we build up on the given information with some additional fitting in Hα. In addition, we reduce the parameter

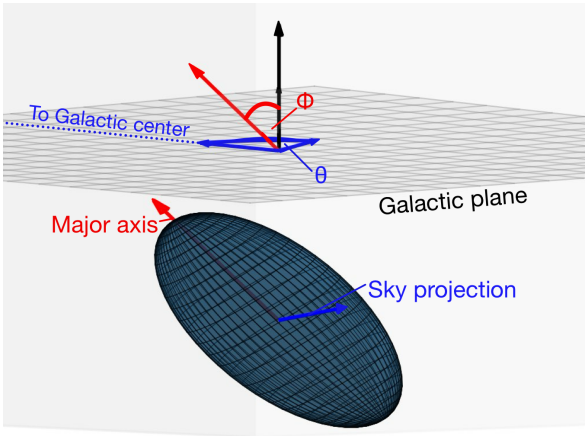

Fig. 39: Schematic prolate ellipsoid with two angles defining the orientation. The Galactic plane angle, ϕ, is the angle between the major axis and the Galactic plane normal (black arrow). The sky projection angle, θ, is the angle of rotation around the Galactic plane normal.

space, describing the OES with a prolate rotationally symmetric ellipsoid, instead of a general ellipsoid. For this, we only need two angles to describe the orientation. First, the angle between the major axis of the ellipsoid and the Galactic plane normal, and second, the rotation angle of the ellipsoid around the Galactic plane normal. The angles are called the Galactic plane and the sky projection angle, respectively. The setup with two angles defining the orientation of a prolate symmetric ellipsoid is shown in Fig. 39. We fix the main axes values and the Galactic plane angle in Model A and T, respectively, and use the Hα-map from Finkbeiner [2003] to adjust the parameters of sky projection angle and ellipsoid position. Similar to Pon et al. [2014], we matched the ellipsoid with Barnard's loop as the most prominent feature in Hα, additionally trying to also match the Eridanus filaments. The best models for setup A and T that we could place in the Hα boundaries are displayed in Fig. 40.

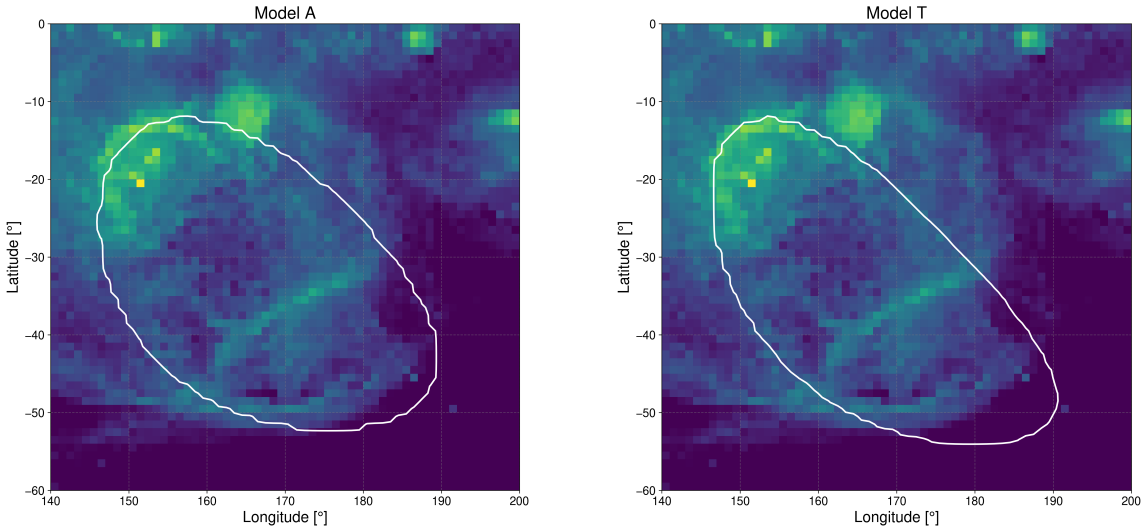

Fig. 40: The two best fitting models A (left) and T (right) in the Hα map from Finkbeiner [2003]. Model T is oriented towards and Model A away from the Sun with the Eridanus end. The model parameters are summarized in Tab. 13.

The fixed parameters and the fit results are summarised in Tab. 13. We continue the terminology from Pon et al. [2014], and refer to these geometries as Model A and T in the following.

Model	**Ellipsoid**				**Position**		
	major axis [pc]	minor axis [pc]	Galactic plane angle [°]	Sky projection angle [°]	x [pc]	y [pc]	z [pc]
A	390	220	35	-5	371	82	-260
T	320	100	85	50	227	86	-122

Tab. 13: Parameter for the Pon et al. [2014] based models A and T, fitted to Hα as displayed in Fig. 40 to extract the missing values, leading to the geometric setup we use for the OES.

4.2.2 Emissivity

We know the profile for an ^{26}Al mass decaying, while moving out spherically symmetric with the sound speed v_s, from Eq. 23. We use this to derive a spatial emissivity $\rho(s)$ with an emissivity profile $f(s)$. This profile is scaled by an emissivity level ρ_0 and is:

$$\begin{aligned} f(s) &= \exp\left(-\frac{\lambda \cdot d}{v_s}\right) \\ \rho(s) &= \rho_0 \cdot f(s) \\ \rho_0 &= \frac{p \cdot M \cdot \lambda}{m \cdot V} \\ V &= \int d\Omega \int s^2 \cdot f(s) ds \end{aligned} \tag{35}$$

, where d is the distance to the position on the LOS, given by the radial component of the LOS s. V is the characteristic volume that is needed to calculate ρ_0. s is also the spatial information of the emissivity profile and therefore of the emissivity ρ_s itself. In our profile, the decay is spatially coupled with the sound speed. To illustrate this, we use such an emissivity to fill the exemplary ellipsoid from Sec. 2.1.2, with one hotspot in the center. In addition, a homogeneously filled ellipsoid results for very high sound speeds in the emissivity profile. The homogeneously filled ellipsoid and one for the sound speed of $v_s = 50\,\mathrm{km\,s^{-1}}$ are shown in Fig. 41, with an ^{26}Al-mass of $\mathrm{M_{Al}} = 1 \cdot 10^{-4}\mathrm{M_\odot}$, when LOS integrated. The homogeneous distribution leads to the same colour coding as we had in the geometric image and is therefore just a translation of the geometry into physical

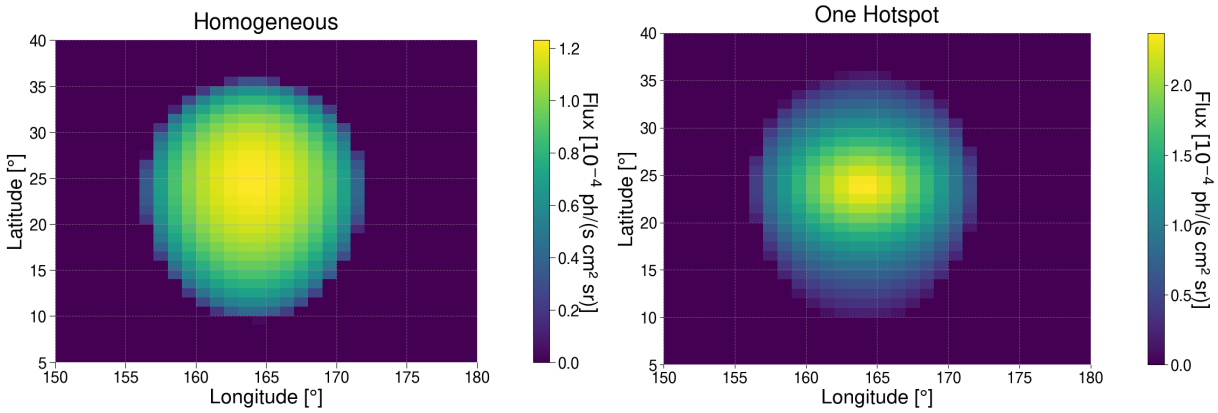

Fig. 41: LOS integrated ellipsoidal models, filled with physical emissivity profiles.
Left: A homogeneous distribution of ^{26}Al leads to the geometric profile when LOS integrated, only now with physical values.
Right: For one Hotspot and with the sound speed of $50\,\mathrm{km\,s^{-1}}$, the ^{26}Al abundance is concise around the hotspot and decays into the outer regions of the ellipsoid. The geometry is now only the result of enough ^{26}Al initial mass to fill up the whole ellipsoid. When comparing the two, we can see that the same amount of ^{26}Al is distributed in the ellipsoid. This leads to a higher maximum flux per sr in the hotspot model, but similar total flux values in both images.

values. The hotspot model shows higher discrepancies of flux. In this model ^{26}Al mass is concentrated in the region around the hotspot and decreases when moving to the edges of the ellipsoid.

Combining the emissivity with the geometric setup for the OES and with the information from the TS maps, we can now produce physical sky models for the OES. We use the likelihood "hotspot" position from the extended source models in the TS maps, $(\ell, b) = (166°, -23°)$, as the center in the emissivity profile. Here, a hotspot is placed inside the ellipsoid and tuned via the sound speed. We test sound speeds of $v_s = 1 - 400\,\mathrm{km\,s^{-1}}$ and the homogeneous case ($v_s \approx \infty$). In Fig. 42 we show two of these skymodels for each geometric model, illustrating the impact of different sound speeds. For a lower sound speed, the decay acts faster than the distribution of ^{26}Al, and the far end of the ellipsoid can not be reached.

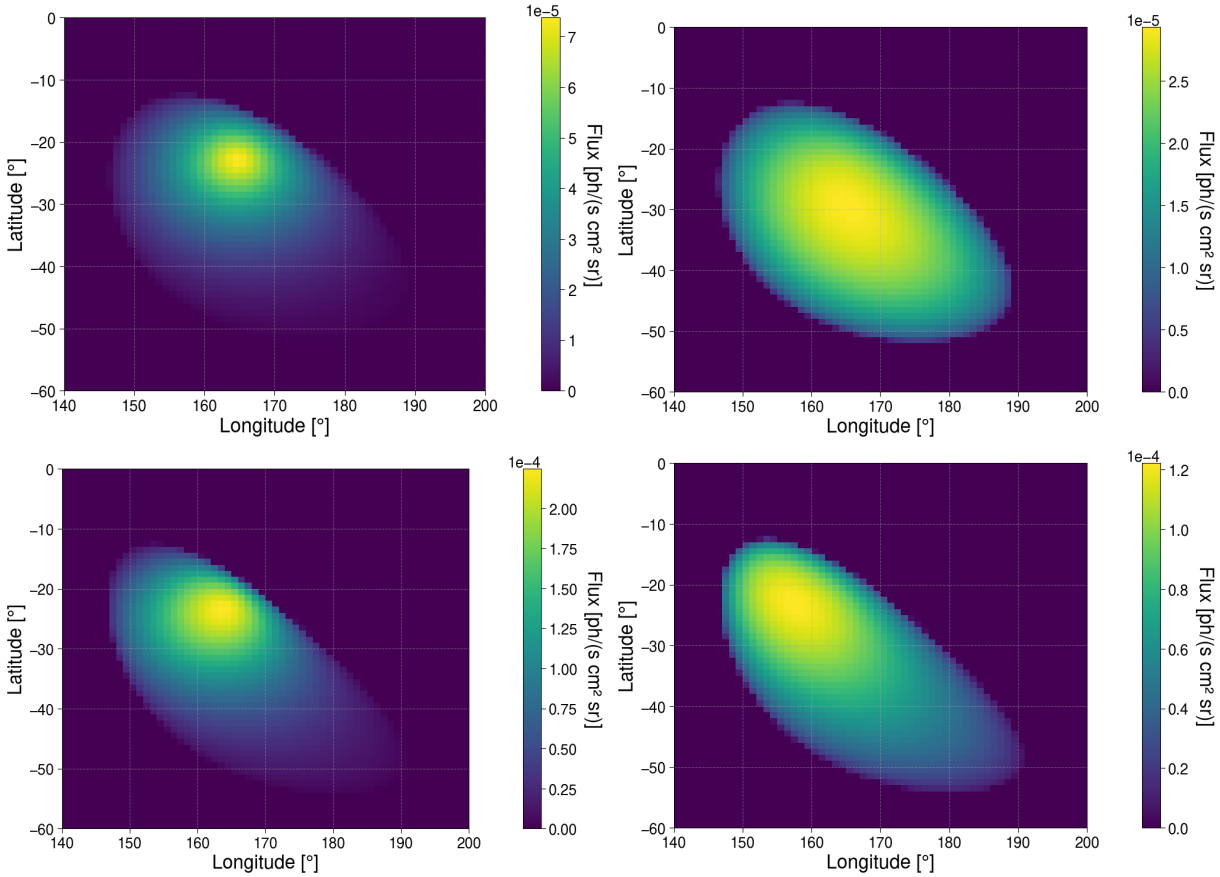

Fig. 42: Physical models A (top) and T (bottom) for one hotspot positioned at $(\ell, b) = (166°, -23°)$. From here, ^{26}Al is blown out with different sound speeds (left: $50\,\mathrm{km\,s^{-1}}$ and right: $400\,\mathrm{km\,s^{-1}}$). If the sound speed is too low, the ^{26}Al is not distributed into the whole ellipsoid.

These models are tested as in Sec. 3.3 using a reference map without any contribution from Orion. Therefore, we can evaluate the statistics in the same way for the different sound speeds. The model improvement when using the respective sky model instead of the blank test region is displayed in Fig. 43. We see that for this model setup, the model

improves for rather low sound speed values. We find the maxima at $10\,\mathrm{km\,s^{-1}}$ for Model A and $5\,\mathrm{km\,s^{-1}}$ for Model T. Considering the physical processes that blow out ^{26}Al, i.e., stellar wind and SNe, these sound speeds are not physical. A reason for this lies within this setup of a physical OES model. The hotspot from the TS maps is a two-dimensional information on the center position in the sky, but not the position inside the ellipsoid. Here, the emissivity is only projected on the boundaries of the OES in the sky. Therefore, these physical models describe the sky in the same way as the initial models from the TS-modelling, only with a different model extension limit. The TS-models are limited to a width of 3-σ, while the physical models are limited to the OES boundaries. Due to the exponential decay in the emissivity profile, for the sound speed of $v_s = 5\,\mathrm{km\,s^{-1}}$ this is an exponential function with $\sigma_{5\mathrm{km/s}} \approx 5°$ in the sky. Thus, we find our most likely model when using one hotspot to be comparable to the most likely 2D Gaussian initial models. Nonetheless, when using the ellipsoid as boundaries our best models are slightly more extended ($\sigma_{phys} \approx 5° - 10°$) than our best TS-models (Sec. 3.3) ($\sigma_{ts} \approx 2° - 5°$). We conclude that the model adaptations are consistent, but we need more information to improve the physical models compared to the initial model setup. For this, we use the information about the production sites of ^{26}Al, the massive stars in the Orion OB1 association.

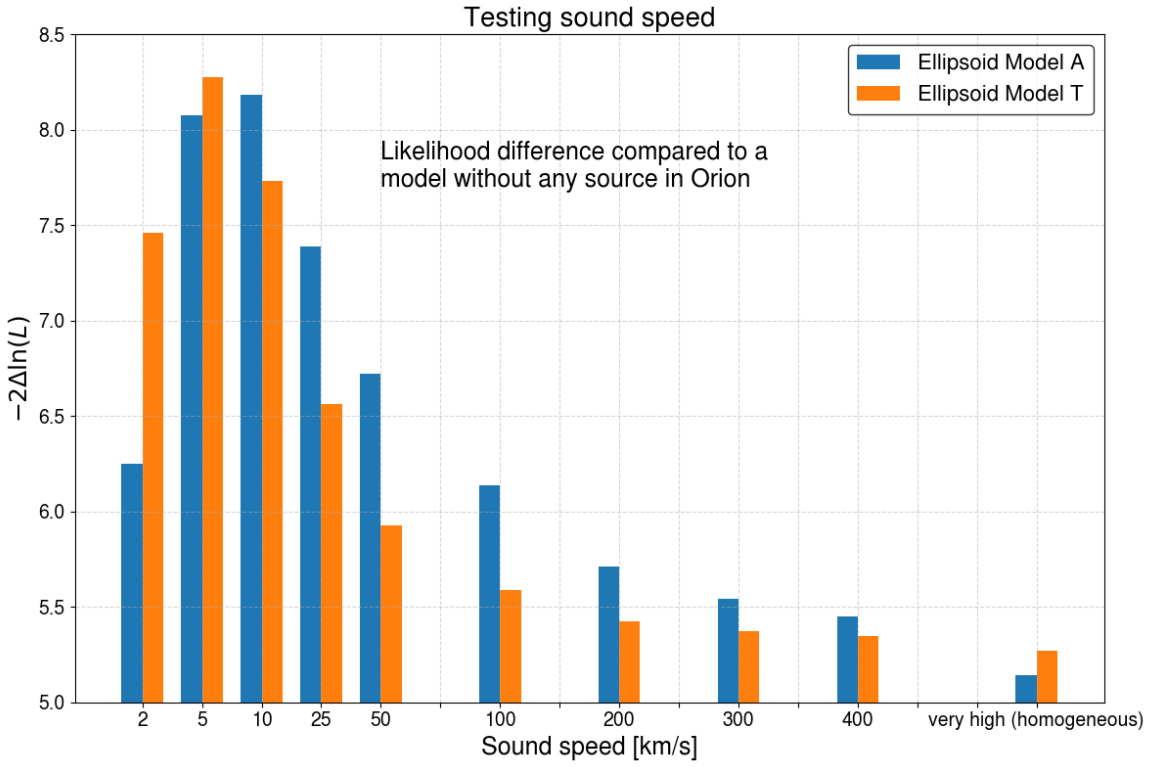

Fig. 43: Model improvement for the physical models A (blue) and T (orange) with an emissivity profile of one hotspot positioned at $(\ell, b) = (166°, -23°)$ for different sound speeds. The most likely models show similar width than the initial models in the TS testing, even though they are slightly wider ($\sigma_{phys} \approx 5° - 10°$ instead of $\sigma_{ts} \approx 2° - 5°$).

4.2.3 ^{26}Al Mass Evaluation

To find an estimate of the ^{26}Al mass and its distribution in the OES, we further examine the subsets of the GAIA catalog, displayed in Fig. 18. According to Wright [2020], Orion contains at least 56 massive stars of spectral type B2 or higher. Nonetheless, when we look at the mass distribution of our subsets, we barely find massive stars at all and none with masses exceeding $\approx 9\,\mathrm{M}_\odot$. This is due to GAIA's magnitude G-band covering 330–1050 nm. [Gaia Collaboration et al., 2021]. B-type stars emit most of their energy in UV radiation [Nieva and Przybilla, 2014]. Therefore, the G-magnitude of B-type stars can be several magnitudes fainter than their bolometric magnitude. Thus, we extrapolate the massive star distribution.

Stellar Mass Extrapolation

The stellar mass distribution follows the PDMF, which is described as a two-part power-law, with the IMF slope below m_{TO} and the PDMF slope for higher masses (see Sec. 2.1.1). To describe this IMF with only one power-law index, the stellar masses are filtered to be minimal $M = 1\,\mathrm{M}_\odot$. The filtered stars for each Orion OB1 subgroup are shown in Fig. 44. Even though we do not see most of the massive stars, we can extrapolate them. This

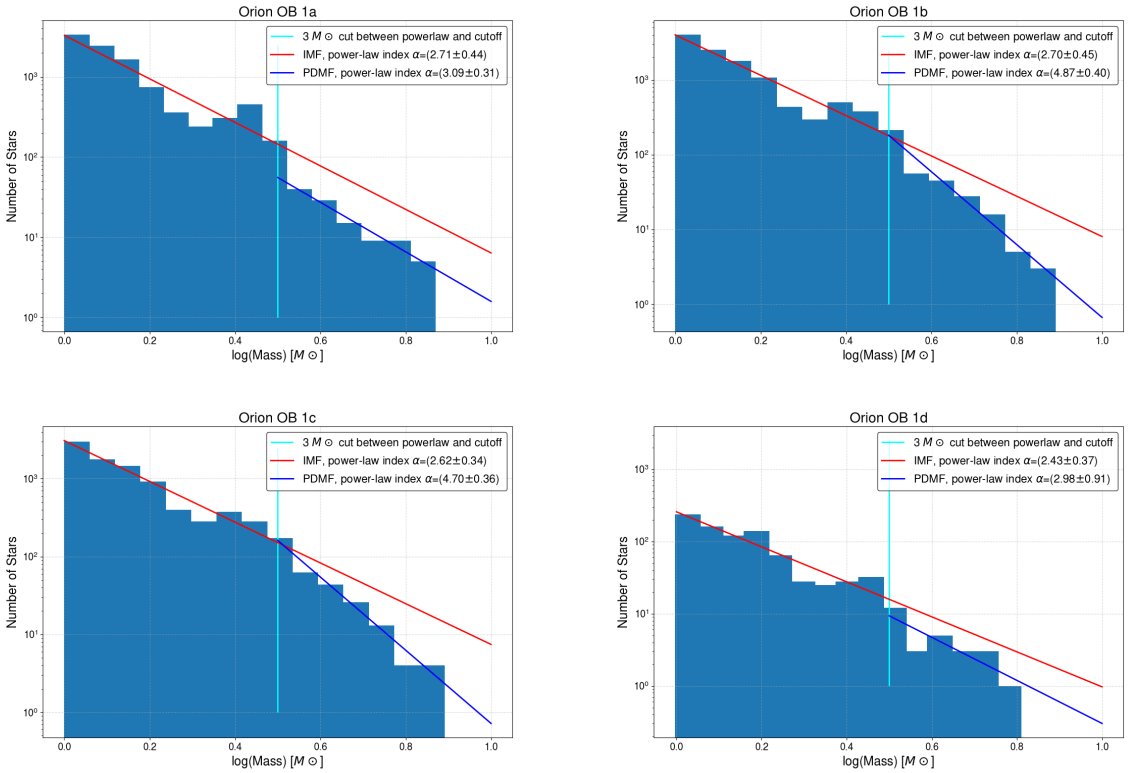

Fig. 44: Stellar mass distribution in the four subgroups of the Orion OB1 association. In the range 1–3 $\mathrm{M}_\odot$ we extract a power-law slope as IMF for each subgroup. For higher masses, we extract a power-law slope of the PDMF. The difference between IMF and PDMF is the rate of already exploded stars, N_{SNe}.

works due to the same cutoff magnitude G=3 in all four subgroups. This brightness cutoff translates to a luminosity cutoff with the distance to the Orion OB1 association. Due to the luminosity-mass relation in main sequence stars, the luminosity cutoff translates to the same mass cutoff in the four subgroups. For the extrapolation, we set m_{TO}, to be $3\,\mathrm{M}_\odot$. This value is not calculated from the age of the subgroups, since GAIA did not observe the expected value for m_{TO}. This is due to the incompleteness in the GAIA observation regarding the massive stars, leading to a shift of m_{TO} to less massive values. Thus, we fit a power-law for the IMF in the range $1\,\mathrm{M}_\odot \leq M \leq 3\,\mathrm{M}_\odot$, and a power-law for the PDMF in the range $3\,\mathrm{M}_\odot \leq M$. The power-laws for the subgroups are shown in Fig. 44. We fit an apparent line into the double logarithmic representation. This represents a power-law with:

$$\log N(\log M) = -\alpha \cdot \log M + b_{\mathrm{int}} \tag{36}$$

, where α is the power-law index for $N \propto M^{-\alpha}$, and b_{int} is the y-intersect of the apparent fit. We derive the following fit parameters for the IMF and the PDMF in the four groups:

Orion OB	1a	1b	1c	1d
IMF	$\alpha = (2.71 \pm 0.44)$ $b = (3.60 \pm 0.12)$	$\alpha = (2.70 \pm 0.45)$ $b = (3.52 \pm 0.13)$	$\alpha = (2.62 \pm 0.34)$ $b = (3.49 \pm 0.09)$	$\alpha = (2.43 \pm 0.37)$ $b = (2.41 \pm 0.10)$
PDMF	$\alpha = (3.09 \pm 0.31)$ $b = (3.29 \pm 0.22)$	$\alpha = (4.87 \pm 0.40)$ $b = (4.70 \pm 0.28)$	$\alpha = (4.70 \pm 0.36)$ $b = (4.56 \pm 0.25)$	$\alpha = (2.98 \pm 0.91)$ $b = (2.46 \pm 0.60)$

Tab. 14: Power-law indices for the different subgroups in the Orion OB1 association. The IMF gives the distribution of stars below $m_{TO} = 3\,\mathrm{M}_{\mathrm{odot}}$, the PDMF for stars above $m_{TO} = 3\,\mathrm{M}_{\mathrm{odot}}$.

We expect for the IMF $\alpha_{\mathrm{IMF,\,Lit}} = (2.3 \pm 0.3)$, and for the PDMF $\alpha_{\mathrm{PDMF,\,Lit}} = 4.53$ (see Sec. 2.1.1). The power-law indices for the IMF and the PDMF in all four subgroups match the expected values, within their uncertainties, with the exception of the Orion-OB-1a and the Orion-OB-1d-PDMF. For these, the extrapolated power-law index is too low. This could be due to using the same m_{TO}, as we do for the younger groups 1b and 1c, where the result fits the expectation. For Ori 1d, the sample is probably to small, leading to the deviation from the expected value that is within a 2-σ interval of our result. The difference between the IMF and the PDMF gives the distribution of stars that are already exploded, i.e., initially formed, but are not part of the present-day observation. We can calculate this difference between the extrapolated power-laws, using Eq. 36 with:

$$\begin{aligned} N_{\mathrm{SNe}}(M) &= N_{\mathrm{IMF}}(M) - N_{\mathrm{PDMF}}(M) \\ N_{\mathrm{SNe}}(M) &= 10^{-\alpha_{\mathrm{IMF}} \cdot \log M + b_{\mathrm{IMF}}} - 10^{-\alpha_{\mathrm{PDMF}} \cdot \log M + b_{\mathrm{PDMF}}} \end{aligned} \tag{37}$$

, with the mass function for the exploded stars, N_{SNe}, the IMF N_{IMF}, and the PDMF, N_{PDMF}. For the different subgroups, we calculate and extrapolate the exploded star mass functions for the subgroups. These are shown in Fig. 45. With this, we conclude that in

Ori 1a, up to $\sim$ 10, in Ori 1b, up to $\sim$ 13, in Ori 1c, up to $\sim$ 15, and in Ori 1d, $\sim$ 1 massive stars exploded, with masses following the N_{SNe}.

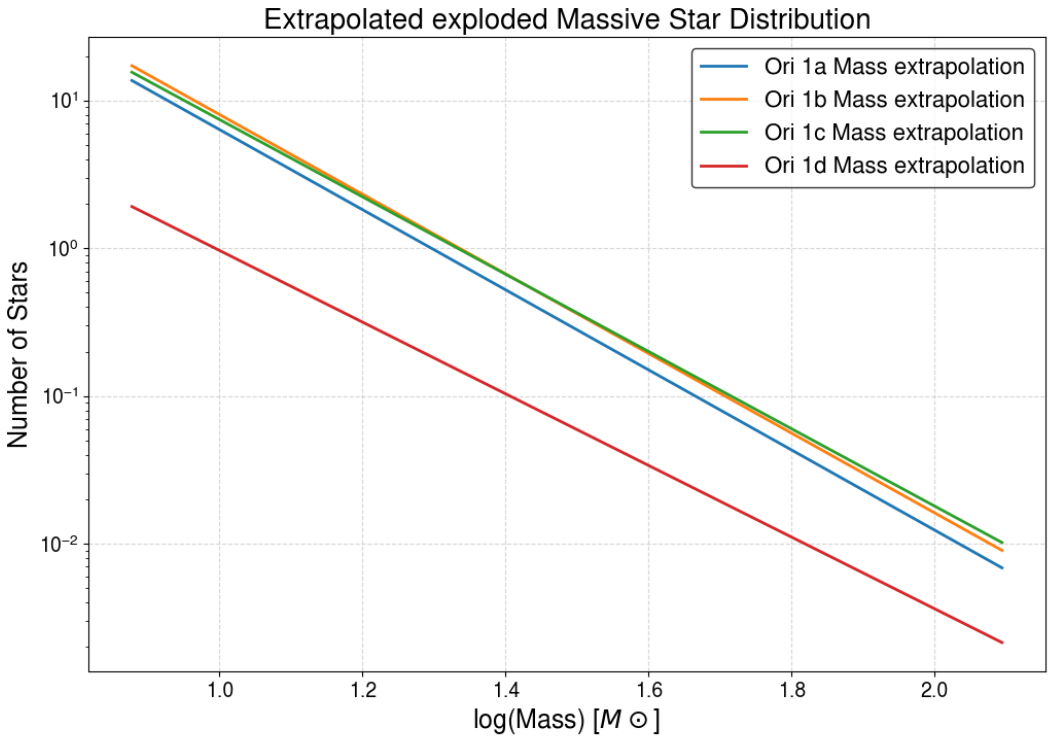

Fig. 45: Stellar mass distribution for exploded stars, N_{SNe}, in the four subgroups of the Orion OB1 association. The power-law distribution results from the difference between the extrapolated IMF and extrapolated PDMF.

Exploded Mass Sampling

With the extrapolated explosion mass functions, we can sample different configurations for the Orion OB1 subgroups. Here, we sample massive stars in the range $8-120\,\mathrm{M}_{\odot}$, that follow the respective N_{SNe}. For this, the number of stars is fixed to upper and lower boundaries for each group, and for each run, a random number of stars within the boundaries is sampled. The mass of these stars is not random but follows the distribution of the N_{SNe}. Thus, each run gives a configuration for one subgroup, with a number of stars inside the boundaries and masses that match the exploded mass rate in this group. To get a statistical set for the subgroups, we sample $1 \cdot 10^{6}$ configurations in total. In each sample, the number of stars varies between one and the maximum of N_{SNe} in the mass range $8\,\mathrm{M}_{\odot} \leq M \leq 120\,\mathrm{M}_{\odot}$, for each subgroup, respectively. The results from the sampled configurations are summarized in Tab. 15.

To confirm the sampling from the N_{SNe}, the mass distribution of the sampled stars, e.g., in Ori 1a, is shown on the left in Fig. 46. Here, the power-law index of the N_{SNe},

Group	N_{Stars} (min)	N_{Stars} (max)	N_{Stars} (mean)	mean M_{Stars} [$M_\odot$]	$\sigma_{M,Stars}$ [$M_\odot$]	mean M_{Group} [$M_\odot$]
Ori 1a	1	10	5.5	17.1	14.0	94
Ori 1b	1	13	7.0	17.0	13.8	119
Ori 1c	1	15	8.0	17.6	14.6	140
Ori 1d	1	2	1.5	19.8	17.2	30

Tab. 15: Summary of the Orion OB1 association exploded star sampling per subgroup. With the mean number of stars in a configuration for each subgroup, N_{Stars}, the mean mass of the stars created in all the samples for each subgroup, mean M_{Stars}, the standard deviation of the mean mass per star, $\sigma_{M,Stars}$, and the mean total mass of all the configurations created for each subgroup mean M_{Group}.

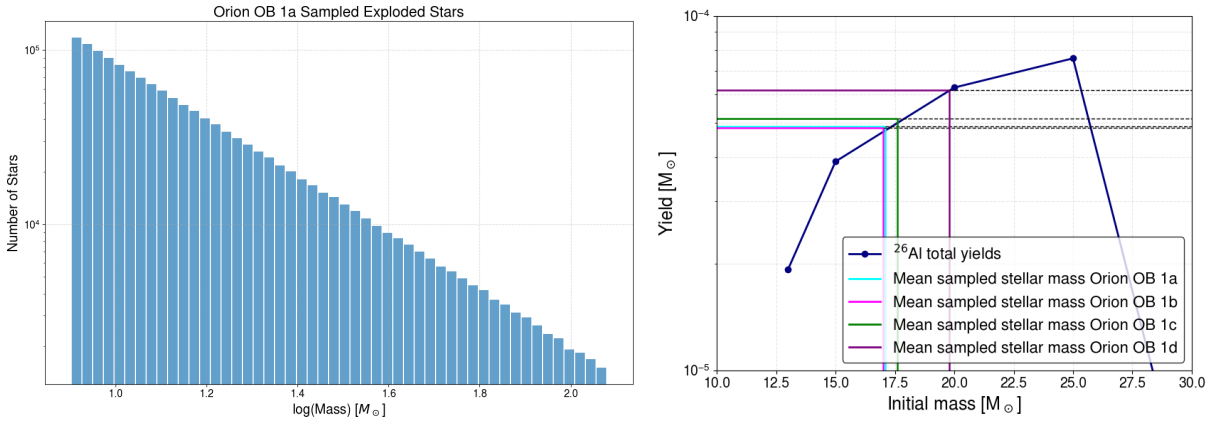

Fig. 46: Left: From the N_{SNe} sampled stars in Ori 1a. Right: For the sampled mean stellar mass in each subgroup, estimated yields with the stellar evolution models (blue dots) from Limongi and Chieffi [2018].

is visible for the distribution of sampled stellar masses. We use the sampling results to estimate the ^{26}Al yields accumulated for the exploded stars in the subgroups. For this, we use the stellar models from Limongi and Chieffi [2018] to evaluate the mean ^{26}Al yield for the mean stellar mass results of the sampled stars in each subgroup. We get this by interpolating the yields for this mass between the stellar evolution model yields. This is shown on the right in Fig. 46. We note that for the standard deviation of the sampled mean stellar mass in all four groups, within one σ-band the mean ^{26}Al yield per star is between $M_{Al,Star=}\,(1.9-7.6)\cdot10^{-5}\,M_\odot$. Thus, we use the mean value to get comparable values for the different groups we have here. The interpolated yields and the total ^{26}Al mass is:

Group	mean N_{Stars}	mean $M_{Al,\,Star}$	$\sigma_{M,\,Al,\,Star}$	mean $M_{Al,\,Group}$
Ori 1a	5.5	$4.9\cdot10^{-5}\,M_\odot$	$(1.9-7.6)\cdot10^{-5}\,M_\odot$	$2.7\cdot10^{-4}\,M_\odot$
Ori 1b	7.0	$4.8\cdot10^{-5}\,M_\odot$	$(1.9-7.6)\cdot10^{-5}\,M_\odot$	$3.4\cdot10^{-4}\,M_\odot$
Ori 1c	8.0	$5.1\cdot10^{-5}\,M_\odot$	$(1.9-7.6)\cdot10^{-5}\,M_\odot$	$4.1\cdot10^{-4}\,M_\odot$
Ori 1d	1.5	$6.2\cdot10^{-5}\,M_\odot$	$(1.9-7.6)\cdot10^{-5}\,M_\odot$	$0.9\cdot10^{-4}\,M_\odot$

Tab. 16: Mass estimation of the Orion OB1 subgroups. We combine the sampling results with the stellar evolution models from Limongi and Chieffi [2018] and get the mean ^{26}Al yield for one star in each subgroup, mean $M_{Al,Star}$. Multiplied with the mean number of stars, this leads to the mean total ^{26}Al mass for the subgroups, mean $M_{Al,Group}$.

With these values, we estimate the total output of ^{26}Al in the four subgroups. These values are only upper limits to the ^{26}Al mass we expect in the OES, since there is no time dependence in the estimate. Here, the values represent the total ^{26}Al that is produced in the Orion OB1 association, over its lifetime.

Population Synthesis

To also evaluate stellar time profiles for sampled stars, we use the `PSYCO` code from Pleintinger [2020]. Similar to our sampling method, the algorithm `PSYCO` samples stars, using an underlying power-law mass distribution. Therefore, we can adjust the code to sample stars for our evaluated exploded star mass function N_{SNe}, for each Orion OB1 subgroup. `PSYCO` uses stellar evolution models to produce ^{26}Al yield time profiles for each sampled star. In our analysis, we use the stellar evolution model by Limongi and Chieffi [2018], which is already implemented in the code. The integration over the time profiles gives the total abundance of ^{26}Al, produced by the sampled stellar group, considering birth at the same time, i.e., for each subgroup, in an evolutionary profile. This profile of the total ^{26}Al output of a stargroup is shown for Ori 1a in Fig. 47. We use the maximum number of stars for each subgroup that we got from the N_{SNe} in the sampled mass range, as the number of sampled stars in each `PSYCO` run.

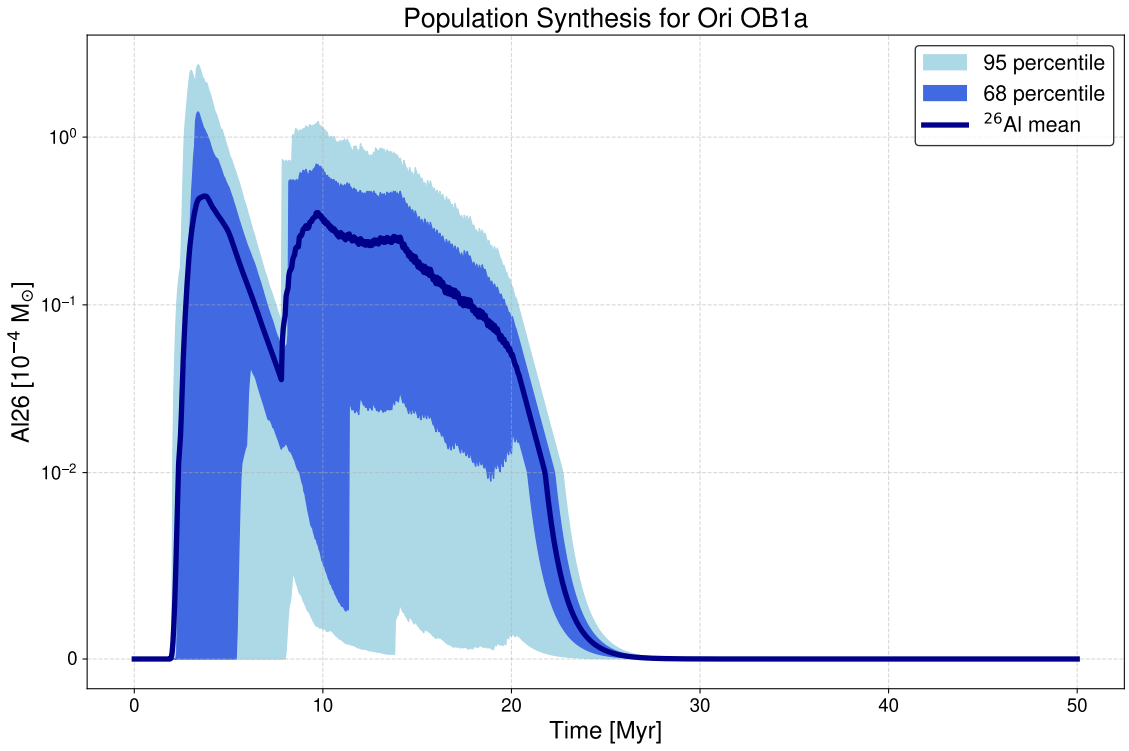

Fig. 47: Population synthesis for Ori 1a. We do 1000 runs, sampling 10 stars in each run. The delay between the birth of the group and the first output of ^{26}Al comes from the time stars need to reach the high burning phases in which the ^{26}Al is produced and then blown out via stellar winds.

The simulation shows ^{26}Al abundance in the groups for about 25 Myr, after birth. Thus, we can apply the age of a star group in the form of an x-axis shift towards negative values, with the ages from Sec. 2.2.4, of the different subgroups. This gives the ^{26}Al contribution from a subgroup for today. When doing the population synthesis for each subgroup, we can apply the range of possible ages. This gives the possible ^{26}Al output from the subgroups, in the given age range. The age-dependent output of ^{26}Al and its uncertainty in the form of the 68% percentile for the four groups, are shown in Fig. 48. We find the Ori OB 1d to be negligible in its contribution to the total ^{26}Al abundance. 1b and 1c have the highest possible solutions in their 68% percentile deviations from the mean. The results for the age-dependent population synthesis of each subgroup are used in our most sophisticated physical models in Sec. 4.2.4

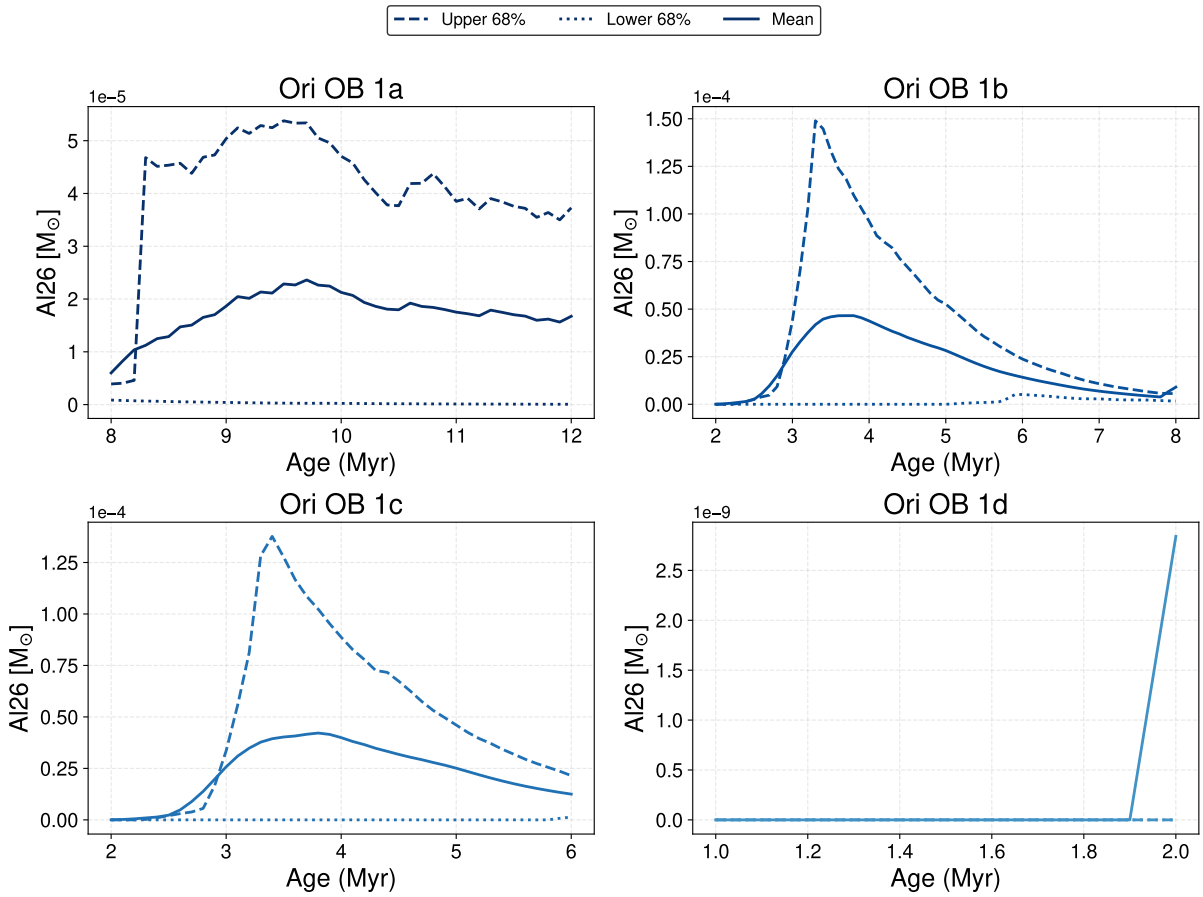

Fig. 48: ^{26}Al population synthesis results for the different Orion OB1 subgroups, considering their ages.

When we combine the population synthesis for the subgroups, we get the total population synthesis for the Orion OB1 association. Here, the age for each subgroup is the center value of the given age range. The sum of the population synthesis profiles after shifting with their age is shown in Fig. 49. We find the mean value of the total ^{26}Al abundance in Orion OB1 today, $M_{Mean} = 8.94 \cdot 10^{-5}\,M_\odot$. Considering the 68% percentiles gives total amount of ^{26}Al between $M_{26} = (0.002 - 1.9) \cdot 10^{-4}\,M_\odot$. Therefore the population synthesis

is below our upper values given by the sampling of the total ^{26}Al output over the Orion OB1 lifetime, in addition, the population synthesis for today is matching with the result for the ^{26}Al abundance in the OES we measured with SPI, using the empirical sky models in Sec. 4.1, $M_{26} = (1.7-5.0) \cdot 10^{-5}\,M_\odot$.

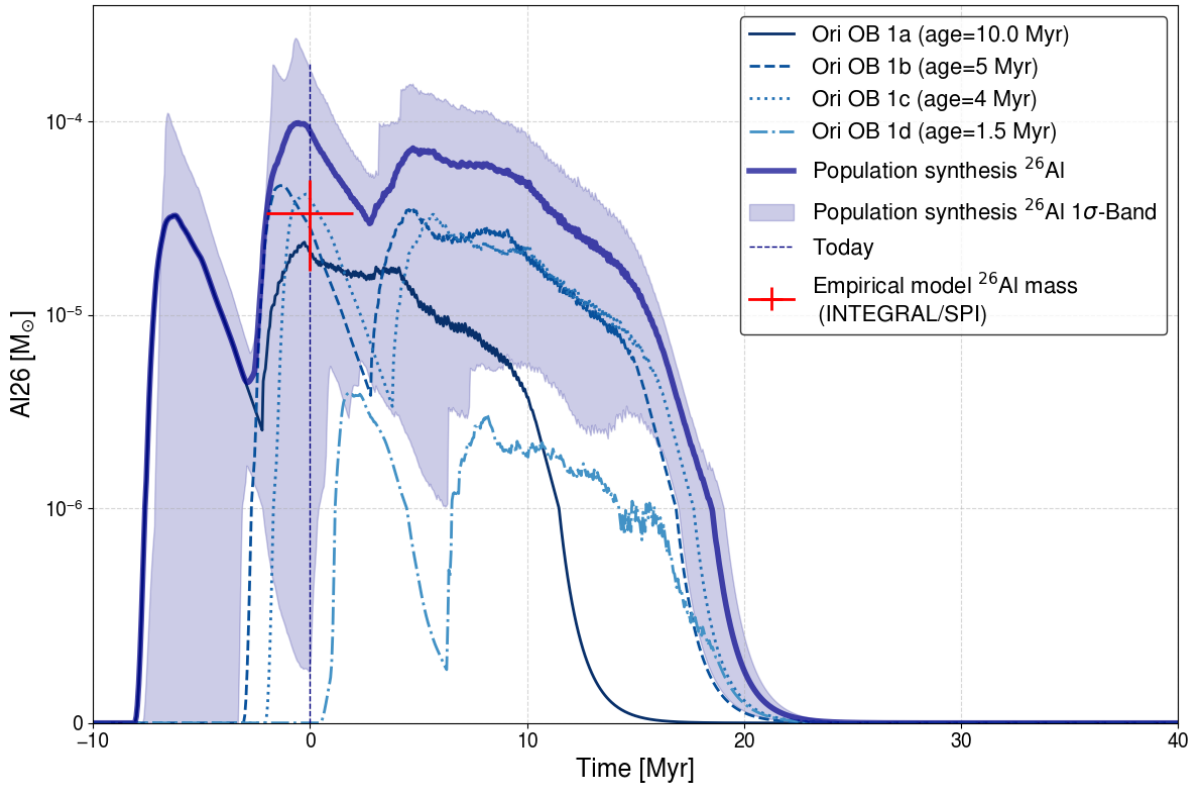

Fig. 49: Population synthesis ^{26}Al results for the entire Orion OB1 association, as superposition of the age adjusted subgroups. For comparison, we show our result of the ^{26}Al abundance in the OES we evaluated for the empirical models (red cross), hinting at the age uncertainties of the subgroups as well. The population synthesis matches with the SPI measured abundance of ^{26}Al, estimated with the empirical models.

4.2.4 Physical OES Models

The physical models of the OES are a combination of the information gathered in the previous sections. We use the geometries given by Model A and Model T, and fill them with an emissivity profile consisting of four hotspots positioned at the location of the Orion OB1 subgroups. These locations are known, except for the distance to Ori 1b, which ranges between 360 – 420 pc. We use the results from the population synthesis of the four subgroups to scale the hotspot amplitude of the different groups with the respective ^{26}Al mass. We use the mean value of the population synthesis and at the age in the middle of the age range, as the standard ^{26}Al mass. In addition, we use the maximum of the 68% percentile profile for each group to test the dominant star group. In such a dominant star group model, we take this maximum value for one of the subgroups,

while the other groups are left with their standard mass estimate. The ^{26}Al mass estimate for Ori 1d is much smaller than the other three. We include it with the mean value for the ^{26}Al mass, but do not test a variation for it. We find in the models that Ori 1d's impact is negligible either way. With these parameters, we build physical models that are tuned by the sound speed.

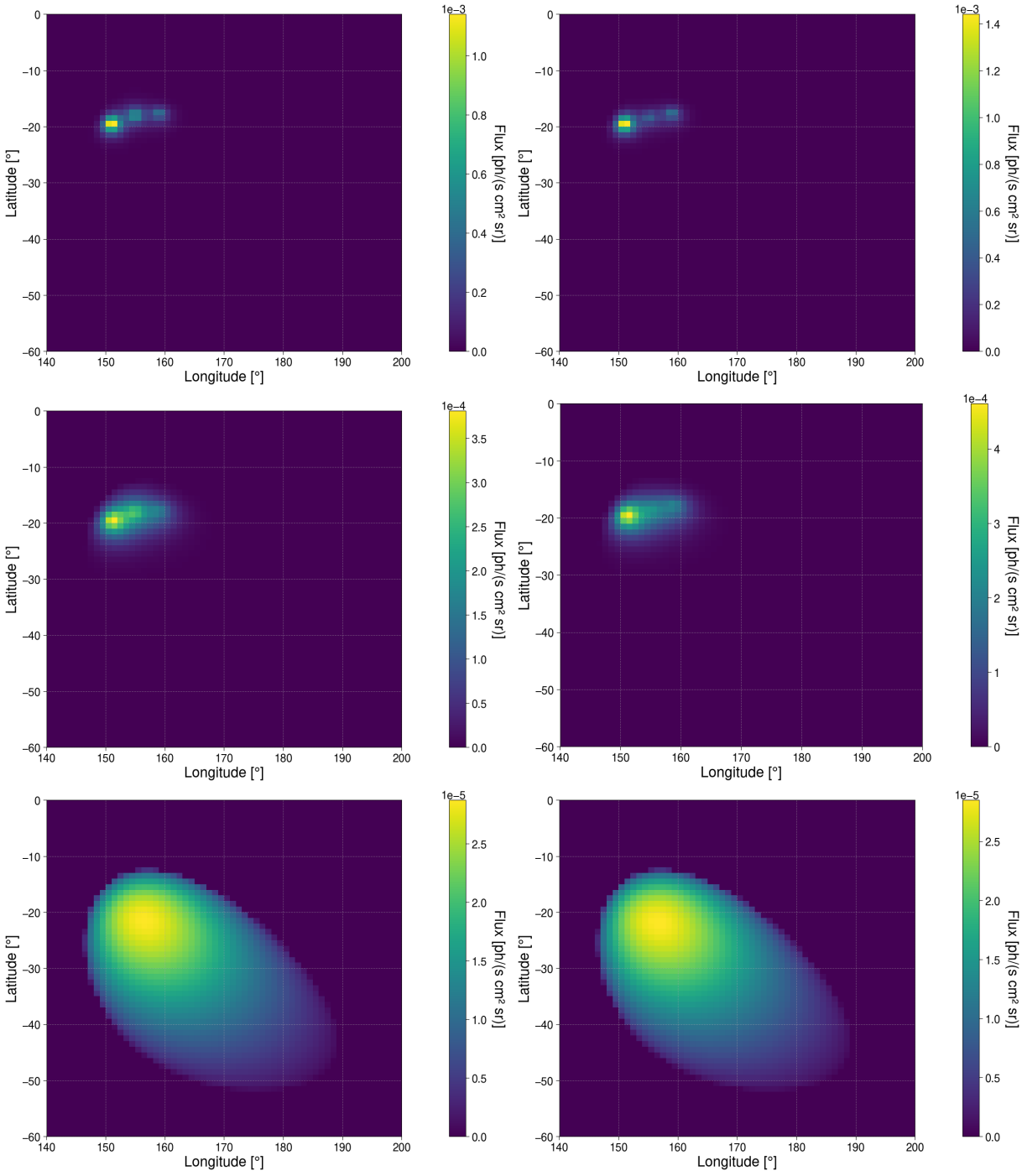

Fig. 50: Physical models of the OES with varying distance to Ori 1b. The models are built with the standard masses for the subgroup and using Model A exemplary. The left panels show Ori 1b at the farthest distance at 420 pc, while the right panels show the nearest configuration with Ori 1b at a distance of 360 pc. The sound speed is 5 km s^{-1}, 10 km s^{-1}, and 100 km s^{-1}, top to bottom.

The sound speed in a physical model is fixed and describes the outflow of ^{26}Al for the hotspots in the emissivity profile, in the same way for all the hotspots. The sound speed in our set of models is between $1-400\,\mathrm{km\,s^{-1}}$. In Fig. 50, we illustrate the impact of the distance to Ori 1b for different sound speeds in the geometry of Model A (Model T shows the same variations for the different ellipsoidal projection on the sky). For the left panels, Ori 1b (middle of the three hotspots) is further away, which results in a smaller flux/sr. Due to the larger distance, the subgroup appears wider in the sky. For increasing sound speed, the impact of the distance decreases, and for v_s =100 $\mathrm{km\,s^{-1}}$, the models get indistinguishable. In Fig. 51, we illustrate the models with different dominant subgroups, again with Model A exemplary. Here, we fix the distance to Ori 1b at 380 pc. The different dominant groups concentrate the flux towards one hotspot in the sky model. For Ori 1a as the dominant star group, due to the age of the subgroup this effect is not as strong. When the sound speed increases, the impact of the dominant group decreases. For v_s =100 $\mathrm{km\,s^{-1}}$, the hotspots smeared into one hotspot that is only slightly shifted between the different dominant group models. The set of models we test are all the configurations that result from combining the parameters in Tab. 17. The combination of the different variable parameters leads to a set of 704 physical models in total.

Ellipsoid Model	**Sound Speed** [$\mathrm{km\,s^{-1}}$]	**^{26}Al Mass Relation**	**Distance** [pc]
A	1	**No Dominant Subgroup**	**Ori 1a**
T	2	Standard: Mean ^{26}Al masses	360
	3	Max: 68% percentile upper limit ^{26}Al mass	**Ori 1b**
	5	**One Dominant Subgroup**	360
	10	Ori 1a	380
	20	Ori 1b	400
	50	Ori 1c	420
	100	**Two Dominant Subgroup**	**Ori 1c**
	200	Ori 1a+1b	385
	300	Ori 1a+1c	**Ori 1d**
	400	Ori 1b+1c	380

Tab. 17: All parameters used in the set of physical models. The two geometries, Model A and Model T, where filled with the emissivity profile describing the subgroups in one of the mass relation configurations, and with a sound speed from the set. In addition, the distance to Ori 1b varies.

4.2.5 Physical Model Results

We use the setup from the TS modelling (Sec. 3.3), with the physical OES models as sky models, and compared to the reference map without any source model in the Orion test region. Thus, we examine the line flux and the model improvement to the reference map for each of the 704 models.

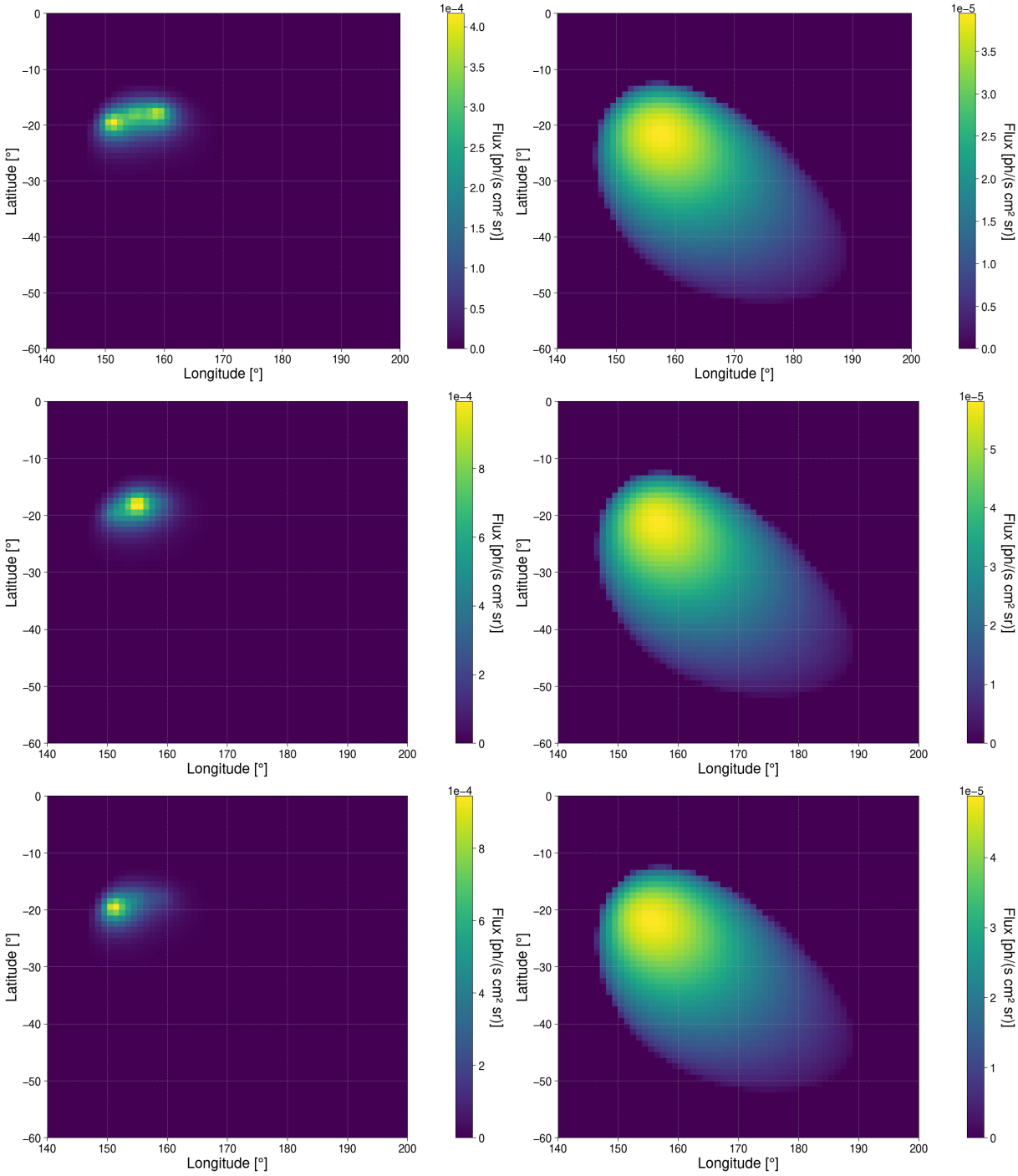

Fig. 51: Physical models of the OES with varying dominant stargroup. Ori 1b is at the distance 380 pc, in the Model A, exemplary. Top to bottom: Ori 1a, 1b, and 1c, as the dominant star group respectively, for the sound speed 10 km s^{-1} in the left, and 100 km s^{-1} in the right panels.

Model Comparison

In order to make statements about the different models, we analyse the impact of different parameters. We start with the distance to Ori 1b. For this, we use the physical models, with the standard ^{26}Al masses in all subgroups. The model improvement, for the

different sound speeds, is shown in Fig. 52, for the 4 different tested distances to Ori 1b. The top panel shows Model A, and the bottom panel shows Model T. The models A and

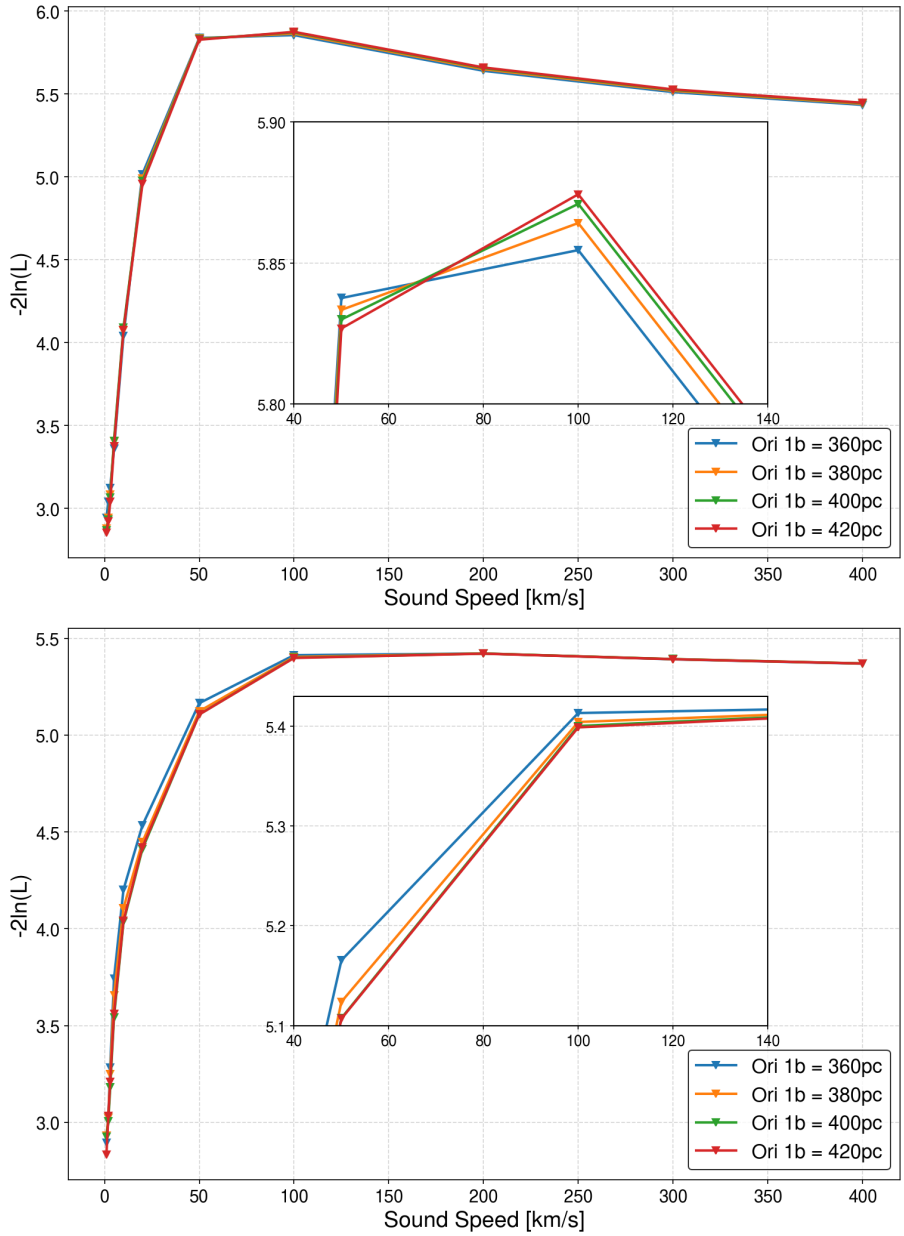

Fig. 52: Model improvement for different sound speeds when varying the distance for Ori OB 1b for models A (top) and T (bottom). The impact of varying the distance is model-dependent. In Model A the best performing models have Ori 1b at 420 pc, in Model T they have Ori 1b at 360 pc, from the Sun. The inset shows a zoom in on the peak performing models.

T show model improvements that mainly depend on the sound speed. Both models show a significant model improvement to the reference map (no sky model in Orion), while no geometry (of A, and T) is significantly better in modelling the OES than the other. The insets in the figure show that the model improvement for different distances to the Ori 1b subgroup depends on the geometry used. For most of the sound speeds in Model A,

it does not matter which distance is chosen. This changes at the peak performing models at $100\,\mathrm{km\,s^{-1}}$, where the models improve with increasing distance to Ori 1b. Thus, we set the distance to Ori 1b to 420 pc in the Model A. For models T, the best performing models have Ori 1b at the distance of 360 pc. Thus, this is the value we use for Model T. With this fixed, we can evaluate the rest of the models. We compare the different dominant star group configurations with the equally weighted configuration. The model improvement for these four categories (1a, 1b, 1c, or no stargroup as dominant), and the flux results are shown in Fig 53. Again, the models A and T, are highly dependent on the sound speed in both the model improvement and the flux, and no geometry is significantly better in the model improvement, even though Model A performs slightly better. While the flux increases model-independently with the sound speed, the model improvement reaches maxima in both models at different sound speeds. The sound speed in models A and T is within 1-σ from the likelihood maximum:

$$v_A = 50^{+\infty}_{-30}\,\mathrm{km\,s^{-1}}$$
$$v_T = 100^{+\infty}_{-80}\,\mathrm{km\,s^{-1}}$$

These sound speed values are in agreement with the expectation between a few hundred and a few $1000\,\mathrm{km\,s^{-1}}$, within the uncertainties [Krause et al., 2018]. We do not see significant differences when changing the dominant star group, but both models perform best regarding their likelihood when choosing Ori 1a as the dominant group. For these, the 1.809 MeV line flux is:

$$F_A = (3.0 \pm 1.2) \cdot 10^{-5}\,\mathrm{ph\,cm^{-2}\,s^{-1}}$$
$$F_T = (3.0 \pm 1.3) \cdot 10^{-5}\,\mathrm{ph\,cm^{-2}\,s^{-1}}$$

These values match the flux results from the empirical modelling of the Orion region.
To evaluate if a combination of two subgroups as dominant, or the 68% percentile upper limit masses from population synthesis, improve the models even further we display these in Fig. 54. Here, the results are very similar to the models with one dominant star group. The maximum mass configuration (with the upper limits for each group), gives the same model improvement and flux as the standard mass setup with the mean ^{26}Al values. This is due to the amplitude being adjusted in the modelling with SPI. The resulting sky models are similar in their relative flux distribution, i.e., more flux in the image but not in relation between the hotspots. The combination of different subgroups does not show a significant change. Nonetheless, models with Ori 1a and 1b, as dominant, perform the best, regarding their likelihood. Since the models with Ori 1a as one dominant star group and the models with Ori 1a in combination with another star group perform the best we conclude that Ori 1a is the dominant contributor of ^{26}Al in the OES.

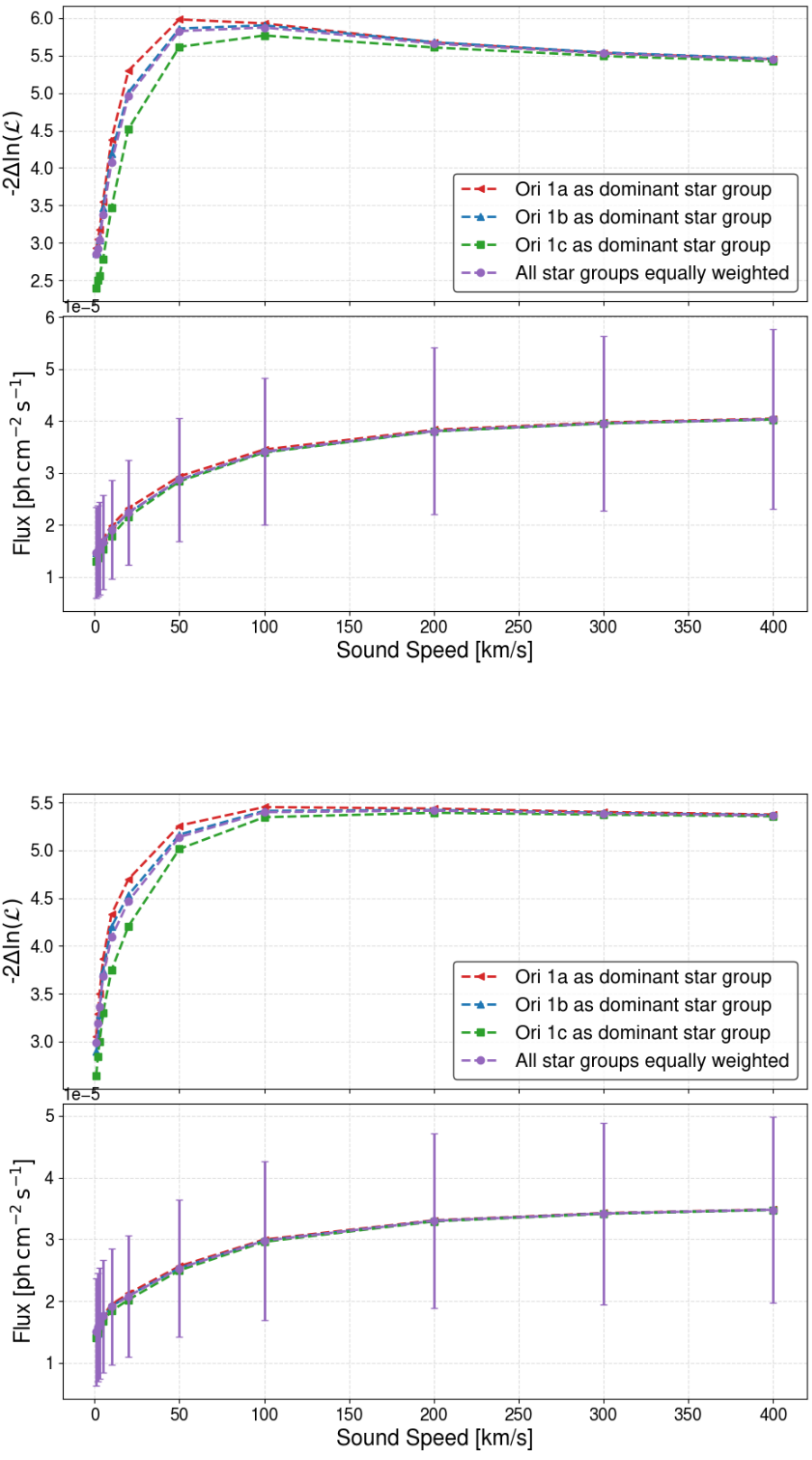

Fig. 53: Physical modelling summary for models A (top) and T (bottom), with Ori OB 1b fixed at a distance of 420 pc for Model A and 360 pc for Model T. Upper y-axis: Model improvement for different sound speeds when fixing the dominant subgroup in the Orion OB1 association as one of 1a, 1b, 1c or no dominant group (mean ^{26}Al expectation each). Lower y-axis: 1.809 MeV line flux for the respective model.

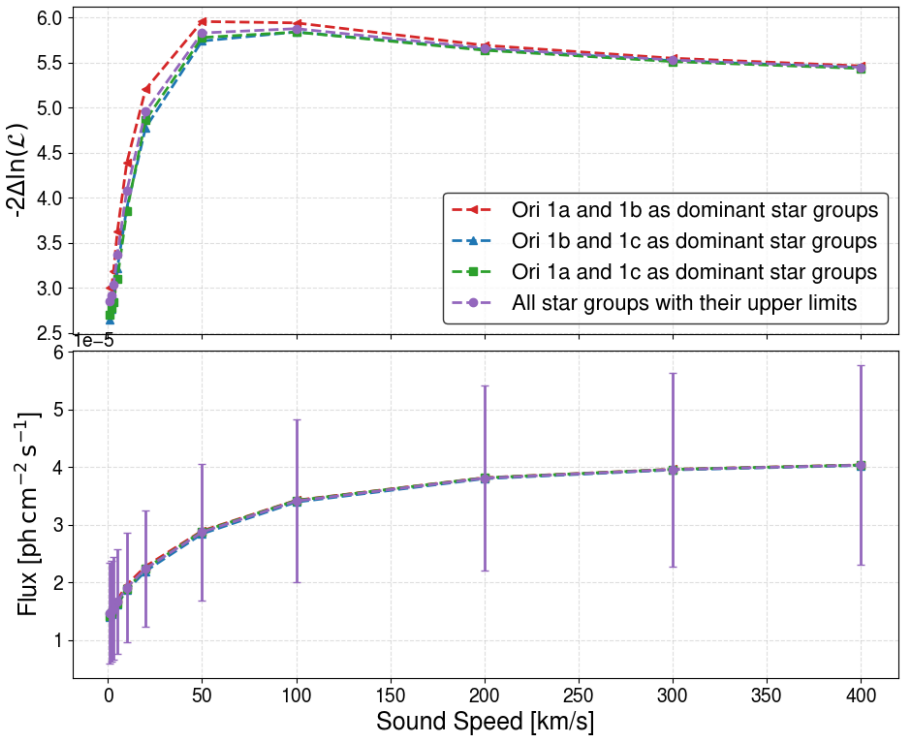

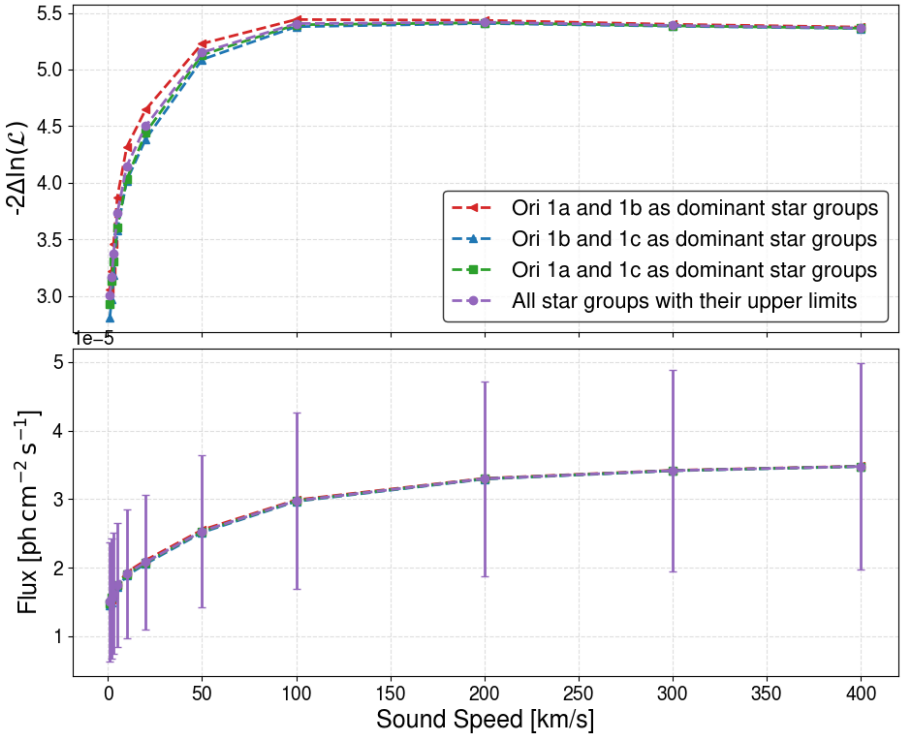

Fig. 54: Physical modelling summary for models A (top) and T (bottom), with Ori OB 1b fixed at a distance of 420 pc for Model A and 360 pc for Model T. Upper y-axis: Model improvement for different sound speeds when fixing two subgroups as dominant in the Orion OB1 association and when using the upper limits for the subgroup ^{26}Al masses. Lower y-axis: 1.809 MeV line flux for the respective model.

Best performing Model

From the model comparison we get the best performing physical model, Model A, with Ori 1b at a distance of 420 pc from the Sun, with Ori 1a as the dominant stellar group in distributing the ^{26}Al, with the sound speed 50 km s^{-1}. The model is shown in Fig. 55. For this sound speed, the ^{26}Al does not reach the far end of the superbubble. This fits with the result from the TS maps, where the flux was constrained to a region above $-40°$ latitude. We use this physical model as a sky model to fit a spectrum to the data, as

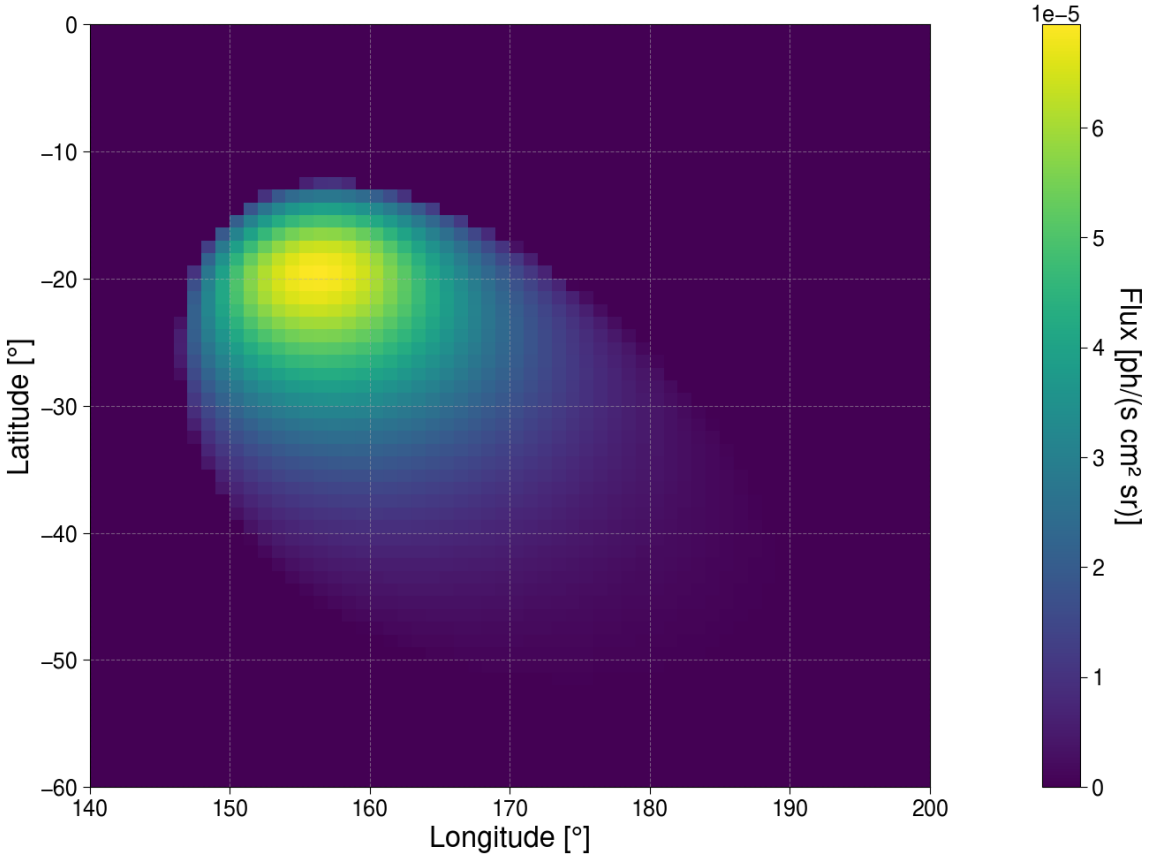

Fig. 55: Best performing physical model, A with Ori 1a as the dominant subgroup. The sound speed is 50 km s^{-1}.

before with the empirical sky models in Sec. 4.1. The rest of the MW is given by the reference map based on the COMPTEL all-sky 1.809 MeV map. The resulting spectrum is shown in Fig. 56, and the fit results are summarised in Tab. 18. Here, also the result of a Bayesian fit for this model is included. For the Bayesian fit we use the same priors as in Sec. 4.1, since the fitted 1.809 MeV line flux model is the same. The posteriors and the priors are shown in the cornerplot Fig. 57.

The flux from the OES matches the results from the empirical models within the uncertainties, and the detection significance of $\sigma = 4.3$ for the likelihood fit is similar to the empirical model detection. This means the significant line flux corresponds to the LOS contribution through the OES, due to the modelling of the total Orion region in the

Physical Model Results						
Method	Flux $[10^{-5}\,\mathrm{ph\,cm^{-2}\,s^{-1}}]$	$\mathrm{FWHM_{Sky}}$ [keV]	Centroid Shift [keV]	$\mathrm{v_{Doppler}}[\mathrm{km\,s^{-1}}]$	sNr	Significance $[\sigma]$
Likelihood Fit	3.5 ± 0.8	$\lesssim 2.9$ (2σ U.L.)	0.39 ± 0.36	65 ± 60	-22.7	4.3
Bayesian Fit	$3.09^{+0.55}_{-0.39}$	$1.14^{+0.48}_{-0.53}$	$0.36^{+0.29}_{-0.28}$	55^{+44}_{-43}	-	5.6

Tab. 18: Model parameter and fit results for our best physical model. The parameters not directly fitted are calculated as in Tab. 9. The Bayesian fit priors are shown with the posteriors in Fig. 57.

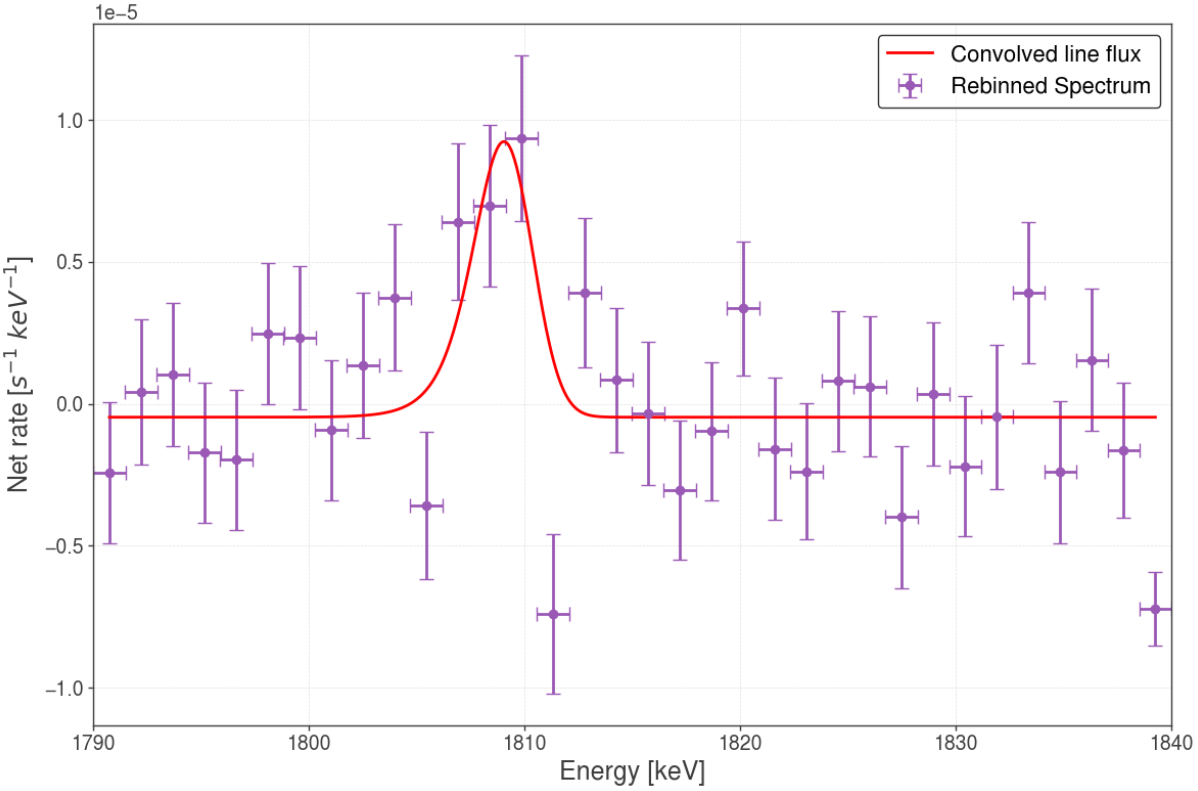

Fig. 56: Observed (purple crosses) gamma-ray spectrum from Orion for our best performing physical model, using model A and Ori 1a as the dominant stargroup. For better illustration, we rebinned the spectra to a 1.5 keV bin size. The fit results are shown in Tab. 18.

empirical approach, in contrast to only the OES in the physical approach. This difference in the sky models could account for the different detection significance in the Bayesian fitting for the physical and empirical model, where we also find a higher 1.809 MeV line flux in the empirical model. Here, the detection significance for the physical model is $\sigma = 5.6$, while the empirical model has $\sigma = 9.2$. In our physical model results, the line flux is again blueshifted, and we find that the ^{26}Al is moving towards the Sun. This velocity is not significantly higher than zero ($v > 0 \approx 1\sigma$). Nonetheless, this could confirm the predominant flow direction of ^{26}Al that is expected for the OES. In addition, the sound speed used in the the physical modelling matches with the $\mathrm{v_{Doppler}}$ evaluation. This shows a consistency in the modelling with the results, i.e., we find that the model built with the sound speed that matches the observed Doppler velocity describes the ^{26}Al signature (the 1.809 MeV line) in the sky the best.

For the line flux evaluated with the Bayesian fit, we calculate the corresponding mass of ^{26}Al, using Eq. 23.

$$M_{26\,\mathrm{phys}} = (2.3 \pm 0.4) \cdot 10^{-5}\,M_{\odot}$$

This value matches the population synthesis results and with the mass evaluation from the empirical models, within the uncertainties. With this, we conclude an ^{26}Al abundance in the direction of the OES, which corresponds to the output from the massive stars in the Orion OB1 association, and can be constrained with the geometry known for the OES.

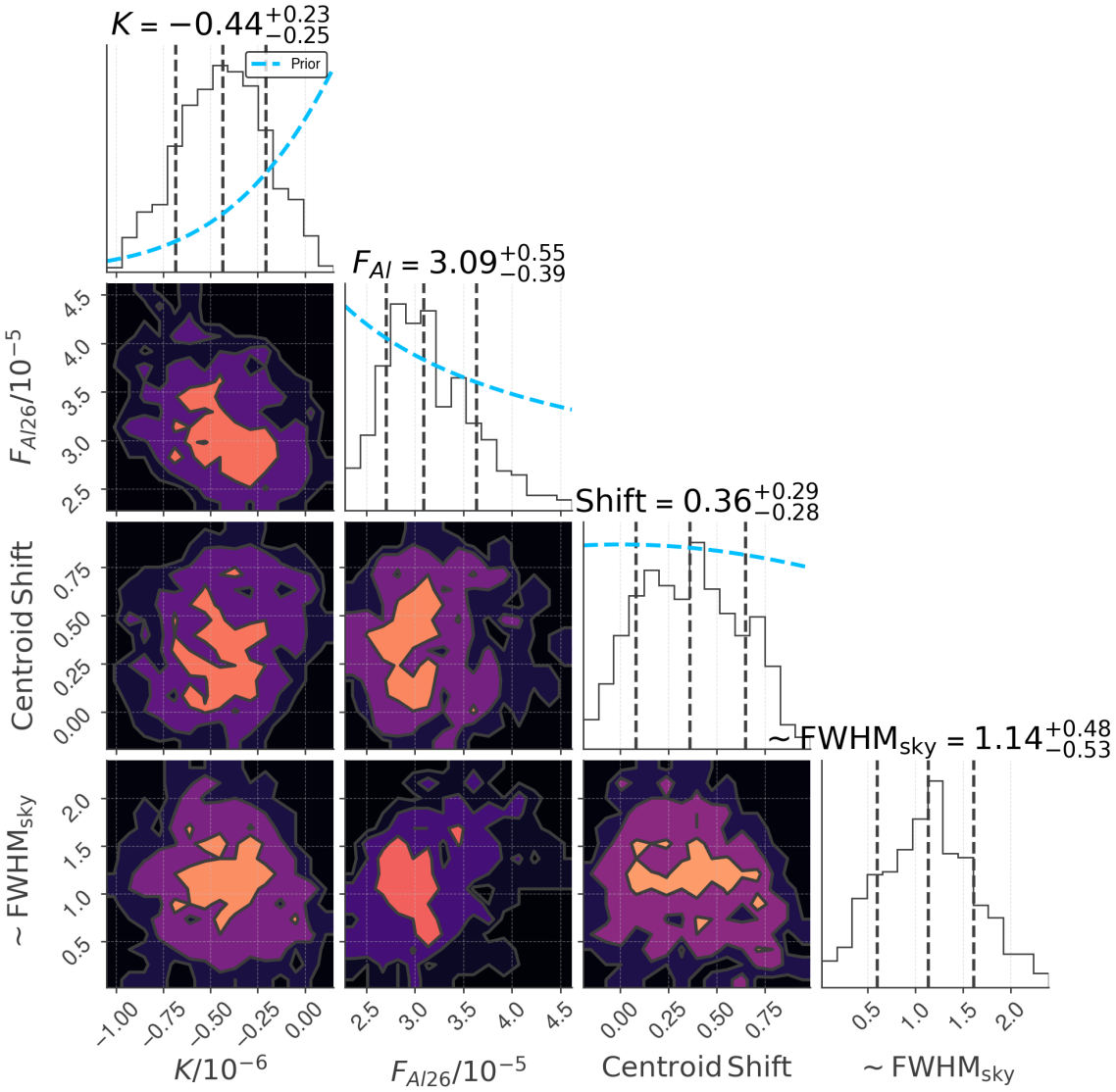

Fig. 57: Bayesian sampled parameters for the 1.809 MeV line flux in the Orion region, using our best physical model, A with Ori 1a as the dominant star group. The continuum K is in units of 10^{-6} ph cm^{-2} s^{-1} keV^{-1}, the flux F_{Al} is in units of 10^{-5} ph cm^{-2} s^{-1} and the centroid shift as well as the FWHM in units of keV.

5 Discussion

In this chapter, we discuss the expected ^{26}Al distribution in the Orion region and morphology of the OES, with the modelling and spectral analysis results for this region.

5.1 ^{26}Al Distribution in Orion

With the empirical models, based on the 1.809 MeV all-sky surveys, from COMPTEL, Plüschke et al. [2001] and from SPI, Bouchet et al. [2015], we detect the 1.809 MeV gamma-ray line corresponding to ^{26}Al in the Orion region with a significance up to $\sigma = 9.2$. This line flux is still significant when we subtract the expected contribution from the Galactic plane, modelled as a double-exponential disk, for the size and position of the region. Thus, we find an ^{26}Al abundance on top of the Galactic expectation, with an ^{26}Al mass of $M_{\mathrm{OES,\,empirical}} = (1.7-5.0) \cdot 10^{-5}\,M_{\odot}$. In the physical modelling, the ^{26}Al distribution is constrained to the geometry of the OES, here we detect the 1.809 MeV gamma-ray line with a significance up to $\sigma = 5.6$. The line flux in the physical modelling corresponds to an ^{26}Al mass of $M_{\mathrm{OES,\,physical}} = (2.3 \pm 0.4) \cdot 10^{-5}\,M_{\odot}$. This value matches the mass evaluated from the empirical models, and we conclude that the ^{26}Al is positioned in the direction of the OES.

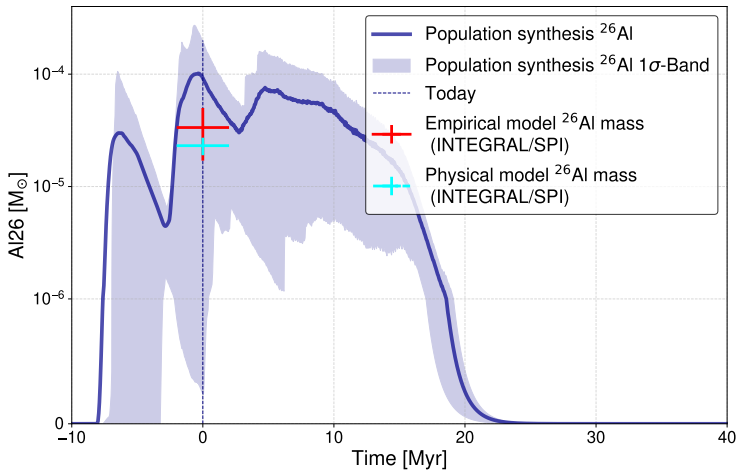

Fig. 58: Mass of ^{26}Al in the OES with population synthesis for the Orion OB1 association. Also, the mass evaluation with the empirical models (red cross) and the physical models (cyan cross) is shown. We see the match for the population synthesis with the SPI measured abundance of ^{26}Al in both model approaches.

Since the physical models are built with the expectation of the stellar output in the Orion OB1 association, i.e., the population synthesis results, we also conclude that the ^{26}Al is accumulated inside the OES. We can say this due to the mass evaluation from the empirical, and the physical modelling of the Orion region matching the yields of ^{26}Al expected from the Orion OB1 stars with population synthesis. The different mass evaluations are summarised in Fig. 58. We note that for the physical models, this is not circular reasoning, even though the models are built on the population synthesis results. This is due to the models being fitted to the SPI data before evaluating the mass, $M_{\mathrm{OES,\,physical}}$.

The TS maps in Sec. 3.3, indicated a shift in the ^{26}Al distribution to the COMPTEL all-sky map from Plüschke et al. [2001]. If we compare our best-performing physical model to the COMPTEL map, we find that the shift in the TS map is not reflected in the physical model. We find a deviation in the physical model from the COMPTEL map hotspot towards the Orion OB1 subgroups. This is shown in Fig. 59. Our physical model is built

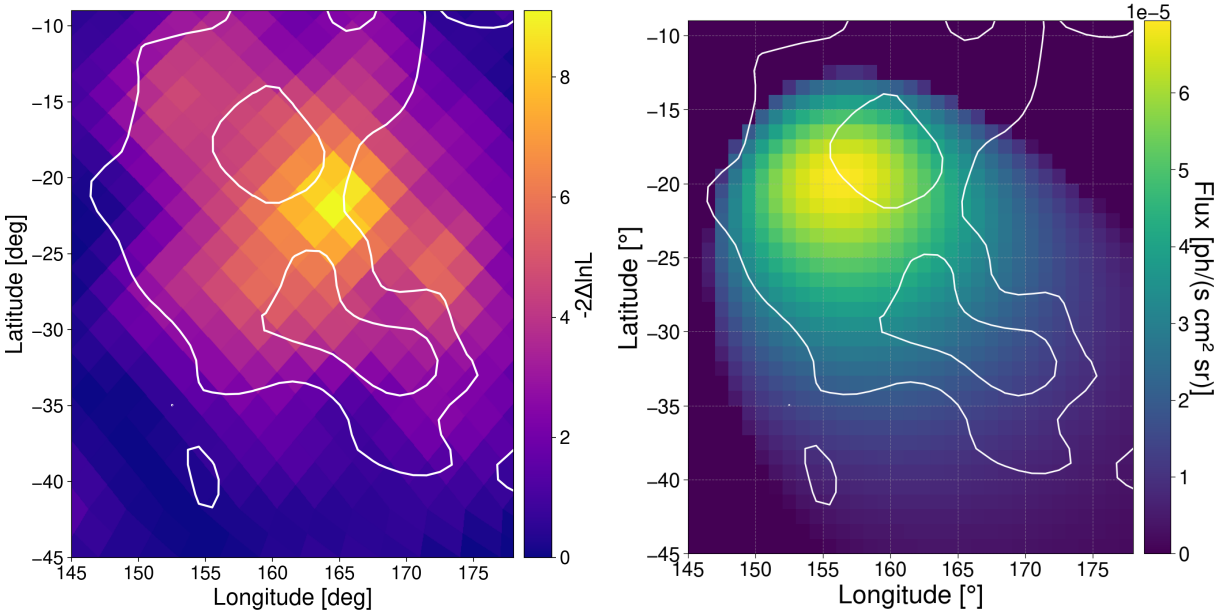

Fig. 59: Results from TS modelling and the best physical model compared to the COMPTEL all-sky map at 1.809 MeV from Plüschke et al. [2001]. The TS map for an initial model with a width of 2° (left) indicates a hotspot in the SPI data that is shifted away from the COMPTEL hotspot. This shift is non-existent in the physical model (right), where we find the hotspot from COMPTEL moving to the other Orion OB1 subgroups.

inside the Hα boundaries for the OES, with the Orion OB1 as the production site for ^{26}Al. In Sec. 2.2, we showed that the COMPTEL map is not aligned with the Hα boundaries of the OES, and the COMPTEL hotspot only aligns with the Ori 1a subgroup. This explains why our physical model hotspot is shifted compared to the COMPTEL map. This shift is in the direction of the Orion OB1 subgroups, while we find a shift towards the Eridanus end in the TS maps.

In our best physical models, Ori 1a is the dominant subgroup, in regard to filling up the OES, independent of the underlying geometry. In Brown et al. [1994] they state that the energy output from the Ori 1a subgroup is sufficient to form the ambient ISM, i.e., the OES. This statement becomes stronger with our analysis even though in our physical models, Ori 1b and 1c contribute to the flux additionally. One reason for Ori 1a being dominant in the ^{26}Al distribution, could be that this subgroup is the oldest one. While Ori 1a evacuated the ISM and formed the OES, Orion 1b and 1c ejected ^{26}Al in the already existing superbubble, leading to a more efficient spatial distribution of the ^{26}Al. Thus, the yields from Ori 1a are concentrated around the production site, while the other subgroups fill up a larger area in the sky.

5.2 OES Morphology

The advanced superbubble modelling from Pon et al. [2014] gives two possible orientations for the OES, with the Eridanus end towards the Sun, or with the Eridanus end away from the Sun. In our physical modelling, both orientations lead to a significant line detection. Model A performs slightly better regarding the likelihood, but there is no significant advantage in choosing Model A over Model T.

If we look at the 1.809 MeV gamma-ray line centroid position in the spectral analysis, we find a blueshift in both the empirical and the physical models for Orion. This blueshift corresponds to a movement of the ^{26}Al towards the Sun with a Doppler velocity that ranges from $v_{\mathrm{D\,empirical}} = (45-91)\,\mathrm{km\,s^{-1}}$, in the empirical, and $v_{\mathrm{D\,physical}} = (55-65)\,\mathrm{km\,s^{-1}}$ in the physical models. These velocities are all above $0\,\mathrm{km\,s^{-1}}$ with a significance of $\approx 1\sigma$. Even though the velocities are not significantly positive, we conclude that the ^{26}Al moves predominantly towards the Sun. This statement is supported by the different modelling approaches that all lead to a blueshifted line flux in Orion. The blueshift also supports an orientation of the OES with the Eridanus end facing the Sun. This is realised in Model T. Model A produces a blueshifted line even though the underlying geometry is oriented away from the Sun. This is due to the LOS that applies when considering the sky as seen by the instrument. In the SPI model fitting, the apparent sky for the ellipsoidal model is fitted to the data.

The evaluated values for the Doppler velocity match the sound speed of our best-performing physical models within the uncertainties. We conclude that the observed Doppler velocity corresponds to the sound speed and that ^{26}Al moves towards the Sun. If the Doppler velocity and the sound speed are the same, the ^{26}Al outflow goes directly towards the Sun, this is shown schematically in Fig. 60. With this, we conclude that the OES lies between the Orion molecular cloud, which hinders an outflow away from the Sun, and the Local Bubble, and thus that the ^{26}Al predominantly flows into the elongated superbubble, towards the Sun. We find our best performing physical models for Model A and Model T

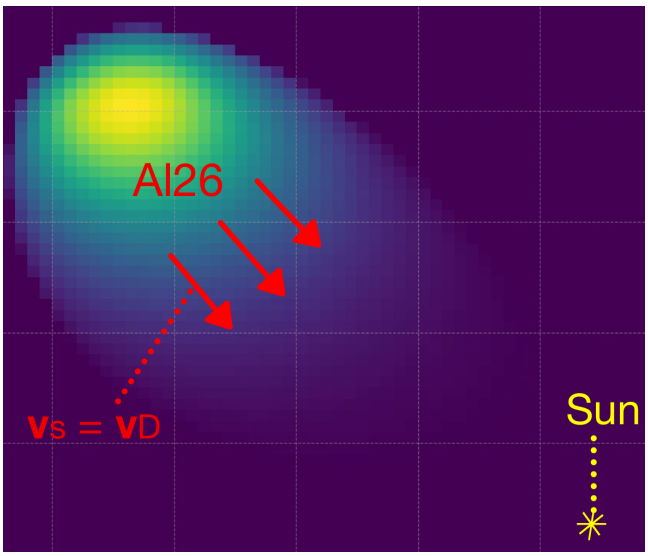

Fig. 60: Schematic ^{26}Al outflow towards the Sun in the best physical model. The sound speed matches the observed Doppler velocity within the uncertainty, confirming the outflow direction.

with sound speeds of $v_s = (50-100)\,\mathrm{km\,s^{-1}}$. For a sound speed up to $50\,\mathrm{km\,s^{-1}}$ our physical models are in agreement with the expectation of a mixed superbubble with the ^{26}Al in the upper part of the bubble, while the Eridanus end is dominated by X-ray emission (see Fig. 14). For a higher sound speed, the ^{26}Al reaches the far end of the bubble, and the entire OES should be visible at 1.809 MeV. The assumption that the ^{26}Al does not reach the far end of the bubble is supported by the flux results from the TS modelling, where no positive ^{26}Al flux is obtained from models below, $-40°$ latitude.

6 Conclusion

The ^{26}Al from massive stars in OB associations fills up superbubbles throughout the universe. A significant 1.809 MeV line detection from the radioactive decay of this isotope could be achieved in previous analysis for Cygnus and ScoCen, but not for the OES in the Orion region. Measurements in other wavelengths contribute to today's knowledge of the morphology of this superbubble, leading to two possible orientations of a prolate rotational symmetric ellipsoidal shape. We use INTEGRAL/SPI observations from over 20 yr, and fit sky models to the data. The data analysis method for SPI, as well as the dataset, are shown in this thesis. The sky models are based on two approaches, empirical and physical. The empirical sky models are based on two surveys from the instruments CGRO/COMPTEL and INTEGRAL/SPI. The physical models are based on the prolate rotational symmetric ellipsoidal shape and the expected ^{26}Al output from the massive stars inside the OES. We find this output of the entire Orion OB1 association to be an ^{26}Al mass of $M_{\mathrm{Al,\,pop}} = (0.002 - 1.9) \cdot 10^{-4} \mathrm{M}_{\odot}$, using population synthesis. The population synthesis is based on an extrapolated exploded massive star estimate we get from GAIA observed stars in the Orion OB1 association, for each stellar subgroup. To validate the sky model fitting method, we analyse spectra for the Cygnus region and the Milky Way in the empirical approach, as strong baseline models with a known flux estimate from a previous significant detection. We find that the results for both baseline models are consistent with the previous analysis within the uncertainties, and conclude that the method works. For the Orion region, we find a blueshifted 1.809 MeV emission line in sky models based on both surveys. We find a line flux of $F_{1809,\,\mathrm{COMPTEL}} = (3.0 \pm 0.8) \cdot 10^{-5} \mathrm{ph\,cm^{-2}\,s^{-1}}$ for the COMPTEL-based and $F_{1809,\,\mathrm{SPI}} = (4.2 \pm 1.0) \cdot 10^{-5} \mathrm{ph\,cm^{-2}\,s^{-1}}$ for the SPI-based sky model. We performed a Bayesian fitting for the latter and find a line flux of $F_{1809,\,\mathrm{SPI,\,Bayesian}} = (4.42^{+0.48}_{-0.44}) \cdot 10^{-5} \mathrm{ph\,cm^{-2}\,s^{-1}}$. For differently sized sky models we get a set of possible models for the Orion region, where we find 1.809 MeV line flux values between $F_{1809,\,\mathrm{Orion}} = (2.4 - 7.6) \cdot 10^{-5} \mathrm{ph\,cm^{-2}\,s^{-1}}$. For these sky models, we subtract the expected contribution of the Galactic plane, modelled as double exponential disk. This leads to a flux of $F_{1809,\,\mathrm{OES}} = (2.2 - 6.6) \cdot 10^{-5} \mathrm{ph\,cm^{-2}\,s^{-1}}$, which we consider as the flux from only the OES. The mass of ^{26}Al inside the OES that corresponds to this flux is $M_{\mathrm{Al,\,empirical}} = (1.7 - 5.0) \cdot 10^{-5} \mathrm{M}_{\odot}$. The physical models are compared regarding their likelihood. We find Ori 1a as the dominant subgroup in filling the OES with ^{26}Al. The distance to Ori 1b, varies in the models with different underlying geometries. The

model with the Eridanus end facing the Sun, Model T, has Ori 1b at a distance of 360 pc, and the model away from the Sun, at a distance of 420 pc in the most likely models. No geometry performs significantly better than the other, while both lead to a significant detection of the OES in the sky model fitting. In the physical models we find a sound speed of $v_A = 50^{+\infty}_{-30}\,\mathrm{km\,s^{-1}}$ in Model A and $v_T = 100^{+\infty}_{-80}\,\mathrm{km\,s^{-1}}$ in Model T. This sound speed matches with the Doppler velocity from the blushifted line results in all the spectra for the OES within the uncertainties. We thus conclude that the ^{26}Al moves predominantly towards the Sun. For our best performing physical model we find a 1.809 MeV line flux of $F_{1809,\,\mathrm{physical}} = (3.5 \pm 0.8) \cdot 10^{-5}\mathrm{ph\,cm^{-2}\,s^{-1}}$ and with Bayesian fitting $F_{1809,\,\mathrm{physical,\,Bayesian}} = (3.09^{+0.55}_{-0.39}) \cdot 10^{-5}\mathrm{ph\,cm^{-2}\,s^{-1}}$. The mass corresponding to this flux from the Orion OB1 association is $M_{\mathrm{Al,\,physical}} = (2.3 \pm 0.4) \cdot 10^{-5}\mathrm{M_\odot}$. Thus, the two model approaches lead to a fitted ^{26}Al mass that matches the population synthesis result within the uncertainties. This supports the stellar evolution models used and confirms that the Orion OB1 association is sufficient in producing the ^{26}Al that fills the OES correspondingly to the observed 1.809 MeV emission. In addition, we significantly detect the OES at 1.809 MeV with the different models. We find a significance of up to $\sigma = 5.6$ in the physical modelling and up to $\sigma = 9.2$ in the empirical modelling. This is the first significant detection of the OES in this wavelength.

Bibliography

H. Akaike. A new look at the statistical model identification. *IEEE Transactions on Automatic Control*, 19(6):716–723, 1974. doi: 10.1109/TAC.1974.1100705.

V. Baumgartner and D. Breitschwerdt. Superbubble evolution in disk galaxies. I. Study of blow-out by analytical models. *Astron. Astrophys.*, 557:A140, September 2013. doi: 10.1051/0004-6361/201321261.

Laurent Bouchet, Elisabeth Jourdain, and Jean-Pierre Roques. The Galactic ^{26}Al Emission Map as Revealed by INTEGRAL SPI. *Astrophys. J.*, 801(2):142, March 2015. doi: 10.1088/0004-637X/801/2/142.

A. G. A. Brown, E. J. de Geus, and P. T. de Zeeuw. The Orion OB1 association. I. Stellar content. *Astron. Astrophys.*, 289:101–120, September 1994. doi: 10.48550/arXiv.astro-ph/9403051.

J. Buchner, A. Georgakakis, K. Nandra, L. Hsu, C. Rangel, M. Brightman, A. Merloni, M. Salvato, J. Donley, and D. Kocevski. X-ray spectral modelling of the AGN obscuring region in the CDFS: Bayesian model selection and catalogue. *Astron. Astrophys.*, 564:A125, April 2014. doi: 10.1051/0004-6361/201322971.

Julie Castillo-Rogez, Torrence V. Johnson, Man Hoi Lee, Neal J. Turner, Dennis L. Matson, and Jonathan Lunine. 26al decay: Heat production and a revised age for iapetus. *Icarus*, 204(2):658–662, 2009. ISSN 0019-1035. doi: https://doi.org/10.1016/j.icarus.2009.07.025. URL `https://www.sciencedirect.com/science/article/pii/S0019103509003248`.

Gilles Chabrier. Galactic Stellar and Substellar Initial Mass Function. *Publications of the Astronomical Society of the Pacific*, 115(809):763–795, July 2003. doi: 10.1086/376392.

T. J. L. Courvoisier, R. Walter, V. Beckmann, A. J. Dean, P. Dubath, R. Hudec, P. Kretschmar, S. Mereghetti, T. Montmerle, N. Mowlavi, S. Paltani, A. Preite Martinez, N. Produit, R. Staubert, A. W. Strong, J. P. Swings, N. J. Westergaard, N. White, C. Winkler, and A. A. Zdziarski. The INTEGRAL Science Data Centre (ISDC). *Astron. Astrophys.*, 411:L53–L57, November 2003. doi: 10.1051/0004-6361:20031172.

R. Diehl, C. Dupraz, K. Bennett, H. Bloemen, W. Hermsen, J. Knoedlseder, G. Lichti, D. Morris, J. Ryan, V. Schönfelder, H. Steinle, A. Strong, B. Swanenburg, M. Varendorff, and C. Winkler. Comptel observations of Galactic ^{26}al emission. *A&A*, 298: L25–L28, 1995.

Roland Diehl, Hubert Halloin, Karsten Kretschmer, Giselher G. Lichti, Volker Schönfelder, Andrew W. Strong, Andreas von Kienlin, Wei Wang, Pierre Jean, Jürgen Knödlseder, Jean-Pierre Roques, Georg Weidenspointner, Stephane Schanne, Dieter H. Hartmann, Christoph Winkler, and Cornelia Wunderer. Radioactive ^{26}Al from massive stars in the Galaxy. *Nature*, 439(7072):45–47, January 2006. doi: 10.1038/nature04364.

Roland Diehl, Thomas Siegert, Jochen Greiner, Martin Krause, Karsten Kretschmer, Michael Lang, Moritz Pleintinger, Andrew W. Strong, Christoph Weinberger, and Xiaoling Zhang. INTEGRAL/SPI γ-ray line spectroscopy. Response and background characteristics. *Astron. Astrophys.*, 611:A12, March 2018. doi: 10.1051/0004-6361/201731815.

F. Feroz, M. P. Hobson, and M. Bridges. MULTINEST: an efficient and robust Bayesian inference tool for cosmology and particle physics. *Mon. Not. R. Astron. Soc.*, 398(4): 1601–1614, October 2009. doi: 10.1111/j.1365-2966.2009.14548.x.

Douglas P. Finkbeiner. A Full-Sky Hα Template for Microwave Foreground Prediction. *Astrophys. J. Suppl. Ser.*, 146(2):407–415, June 2003. doi: 10.1086/374411.

Gaia Collaboration, T. Prusti, J. H. J. de Bruijne, A. G. A. Brown, A. Vallenari, C. Babusiaux, C. A. L. Bailer-Jones, U. Bastian, M. Biermann, D. W. Evans, L. Eyer, F. Jansen, C. Jordi, S. A. Klioner, U. Lammers, L. Lindegren, X. Luri, F. Mignard, D. J. Milligan, et al. The Gaia mission. *Astron. Astrophys.*, 595:A1, November 2016. doi: 10.1051/0004-6361/201629272.

Gaia Collaboration, A. G. A. Brown, A. Vallenari, T. Prusti, J. H. J. de Bruijne, C. Babusiaux, M. Biermann, O. L. Creevey, D. W. Evans, L. Eyer, A. Hutton, F. Jansen, C. Jordi, S. A. Klioner, U. Lammers, L. Lindegren, et al. Gaia Early Data Release 3. Summary of the contents and survey properties. *Astronomy & Astrophysics*, 649:A1, May 2021. doi: 10.1051/0004-6361/202039657.

Philip C. Gregory. *Bayesian Logical Data Analysis for the Physical Sciences*. Cambridge University Press, 2005. ISBN 978-0-521-84150-1. doi: 10.1017/CBO9780511791277.

J. Knödlseder, D. Dixon, K. Bennett, H. Bloemen, R. Diehl, W. Hermsen, U. Oberlack, J. Ryan, V. Schonfelder, and P. von Ballmoos. Image reconstruction of comptel 1.8 mev 26al line data, 1999. URL `https://arxiv.org/abs/astro-ph/9903172`.

M. Krause, K. Fierlinger, R. Diehl, A. Burkert, R. Voss, and U. Ziegler. Feedback by massive stars and the emergence of superbubbles. I. Energy efficiency and Vishniac instabilities. *Astron. Astrophys.*, 550:A49, February 2013. doi: 10.1051/0004-6361/201220060.

Martin Krause, Roland Diehl, Hans Böhringer, Michael Freyberg, and Daniel Lubos. Feedback by massive stars and the emergence of superbubbles. II. X-ray properties. *Astron. Astrophys.*, 566:A94, June 2014. doi: 10.1051/0004-6361/201423871.

Martin G. H. Krause, Andreas Burkert, Roland Diehl, Katharina Fierlinger, Benjamin Gaczkowski, Daniel Kroell, Judith Ngoumou, Veronica Roccatagliata, Thomas Siegert, and Thomas Preibisch. Surround and Squash: the impact of superbubbles on the interstellar medium in Scorpius-Centaurus OB2. *Astron. Astrophys.*, 619:A120, November 2018. doi: 10.1051/0004-6361/201732416.

Pavel Kroupa. On the variation of the initial mass function. *Mon. Not. R. Astron. Soc.*, 322(2):231–246, April 2001. doi: 10.1046/j.1365-8711.2001.04022.x.

Marco Limongi and Alessandro Chieffi. Presupernova Evolution and Explosive Nucleosynthesis of Rotating Massive Stars in the Metallicity Range -3 $\leq$ [Fe/H] $\leq$ 0. *Astrophys. J. Suppl. Ser.*, 237(1):13, July 2018. doi: 10.3847/1538-4365/aacb24.

L. Lindegren, J. Hernández, A. Bombrun, S. Klioner, U. Bastian, M. Ramos-Lerate, A. de Torres, H. Steidelmüller, C. Stephenson, D. Hobbs, U. Lammers, M. Biermann, R. Geyer, T. Hilger, D. Michalik, U. Stampa, P. J. McMillan, J. Castañeda, M. Clotet, G. Comoretto, M. Davidson, C. Fabricius, G. Gracia, N. C. Hambly, A. Hutton, A. Mora, J. Portell, F. van Leeuwen, et al. Gaia Data Release 2. The astrometric solution. *Astron. Astrophys.*, 616:A2, August 2018. doi: 10.1051/0004-6361/201832727.

M. Lugaro and A. Chieffi. *Radioactivities in Low- and Intermediate-Mass Stars*, page 83–151. Springer Berlin Heidelberg, June 2010. ISBN 9783642126987. doi: 10.1007/978-3-642-12698-7_3. URL `http://dx.doi.org/10.1007/978-3-642-12698-7_3`.

Mordecai-Mark Mac Low and Richard McCray. Superbubbles in Disk Galaxies. *Astrophys. J.*, 324:776, January 1988. doi: 10.1086/165936.

François Mignard. Astronomical distance scales. *Comptes Rendus. Physique*, 20(1–2): 140–152, January 2019. ISSN 1878-1535. doi: 10.1016/j.crhy.2019.02.001. URL `http://dx.doi.org/10.1016/j.crhy.2019.02.001`.

María-Fernanda Nieva and Norbert Przybilla. Fundamental properties of nearby single early b-type stars. *Astronomy & Astrophysics*, 566:A7, May 2014. ISSN 1432-0746. doi: 10.1051/0004-6361/201423373. URL `http://dx.doi.org/10.1051/0004-6361/201423373`.

Moritz M. M. Pleintinger. *Star Groups and their Nucleosynthesis*. PhD thesis, Technische Universität München, 2020. URL `https://mediatum.ub.tum.de/1554296`.

Moritz M. M. Pleintinger, Thomas Siegert, Roland Diehl, Yusuke Fujimoto, Jochen Greiner, Martin G. H. Krause, and Mark R. Krumholz. Comparing simulated ^{26}Al maps to gamma-ray measurements. *Astron. Astrophys.*, 632:A73, December 2019. doi: 10.1051/0004-6361/201935911.

S. Plüschke, R. Diehl, K. Kretschmer, D. H. Hartmann, and U. Oberlack. Gamma-ray line emission from superbubbles in the interstellar medium: The cygnus region. In Steven Ritz, Neil Gehrels, and Chris R. Shrader, editors, *Gamma 2001: Gamma-Ray Astrophysics*, volume 587 of *American Institute of Physics Conference Series*, pages 518–522. AIP, October 2001. doi: 10.1063/1.1419456.

Onno R. Pols. Stellar structure and evolution. `https://www.astro.ru.nl/~onnop/education/`, 2011. Lecture notes, Utrecht University.

Andy Pon, Doug Johnstone, John Bally, and Carl Heiles. Kompaneets model fitting of the Orion-Eridanus superbubble. *Mon. Not. R. Astron. Soc.*, 444(4):3657–3669, November 2014. doi: 10.1093/mnras/stu1704.

Andrew Pressley. *Elementary Differential Geometry*. Springer, 2nd edition, 2010. ISBN 978-1-84882-891-9.

Edwin E. Salpeter. The Luminosity Function and Stellar Evolution. *Astrophys. J. Suppl. Ser.*, 121:161, January 1955. doi: 10.1086/145971.

J. M. Scalo. The Stellar Initial Mass Function. 11:1–278, May 1986.

J. Michael Shull. Supernovae, supernova remnants, and superbubbles. In Michael R. Haas, Jacqueline A. Davidson, and Edwin F. Erickson, editors, *From Gas to Stars to Dust*, volume 73 of *Astronomical Society of the Pacific Conference Series*, pages 365–386, January 1995.

Thomas Siegert. *Positron-Annihilation Spectroscopy throughout the Milky Way*. Dissertation, Technische Universität München, München, 2017.

Thomas Siegert, Roland Diehl, Christoph Weinberger, Moritz M. M. Pleintinger, Jochen Greiner, and Xiaoling Zhang. Background modelling for γ-ray spectroscopy with INTEGRAL/SPI. *Astron. Astrophys.*, 626:A73, June 2019. doi: 10.1051/0004-6361/201834920.

G. Vedrenne, J.-P. Roques, V. Schönfelder, P. Mandrou, G. G. Lichti, A. von Kienlin, B. Cordier, S. Schanne, J. Knödlseder, G. Skinner, P. Jean, F. Sanchez, P. Caraveo,

B. Teegarden, P. von Ballmoos, L. Bouchet, P. Paul, J. Matteson, S. Boggs, C. Wunderer, P. Leleux, G. Weidenspointner, Ph. Durouchoux, R. Diehl, A. Strong, M. Cassé, M. A. Clair, and Y. André. SPI: The spectrometer aboard INTEGRAL. *Astron. Astrophys.*, 411:L63–L70, November 2003. doi: 10.1051/0004-6361:20031482.

Giacomo Vianello et al. astromodels: A model definition and serialization system for 3ml, 2015. URL `https://doi.org/10.5281/zenodo.59366`.

R. Voss, R. Diehl, D. H. Hartmann, M. Cerviño, J. S. Vink, G. Meynet, M. Limongi, and A. Chieffi. Using population synthesis of massive stars to study the interstellar medium near OB associations. *Astron. Astrophys.*, 504(2):531–542, September 2009. doi: 10.1051/0004-6361/200912260.

Wei Wang. Galactic Al 1.8 MeV Gamma-Ray Surveys with Integral. In *International Journal of Modern Physics Conference Series*, volume 23 of *International Journal of Modern Physics Conference Series*, pages 48–53, January 2013. doi: 10.1142/S2010194513011069.

R. Weaver, R. McCray, J. Castor, P. Shapiro, and R. Moore. Interstellar bubbles. II. Structure and evolution. *Astrophys. J.*, 218:377–395, December 1977. doi: 10.1086/155692.

C. Winkler, T. J.-L. Courvoisier, G. Di Cocco, N. Gehrels, A. Giménez, S. Grebenev, W. Hermsen, J. M. Mas-Hesse, F. Lebrun, N. Lund, G. G. C. Palumbo, J. Paul, J.-P. Roques, H. Schnopper, V. Schönfelder, R. Sunyaev, B. Teegarden, P. Ubertini, G. Vedrenne, and A. J. Dean. The INTEGRAL mission. *Astron. Astrophys.*, 411:L1–L6, November 2003. doi: 10.1051/0004-6361:20031288.

Nicholas J. Wright. OB Associations and their origins. *New Astronomy Reviews*, 90: 101549, November 2020. doi: 10.1016/j.newar.2020.101549.

Eidesstattliche Erklärung

Hiermit erkläre ich, dass ich die vorliegende Arbeit eigenständig und ohne fremde Hilfe angefertigt habe. Textpassagen, die wörtlich oder dem Sinn nach auf Publikationen oder Vorträgen anderer Autoren beruhen, sind als solche kenntlich gemacht. Die Arbeit wurde bisher keiner anderen Prüfungsbehörde vorgelegt und auch noch nicht veröffentlicht.

Würzburg, 01.12.2025

Niklas Bauer